UNIVERSITY OF LIVERPOOL

Monitoring Partial Discharge Signals using a Chromatic Approach

by

Mohamed Ragaa

Thesis submitted in accordance with the requirements of the University of Liverpool for the degree of Doctor in Philosophy

May 2012

Abstract

A novel approach for extracting information about the insulation integrity of a dielectric from Partial Discharge (PD) signals is described. The approach is based upon chromatic methodologies and involves addressing PD signals with three processors having non-orthogonal (overlapping) responses. The outputs of the three processors are transformed into a number of chromatic parameters designated x, y, z and H, L, S. x, y, z represent the proportion of the signal from each of the three processors. H, L, S represent respectively the dominant phase, effective strength and notional spread of the PD signals. A range of Partial Discharge signals obtained by various researchers worldwide have been analysed using the chromatic approach. These include investigations on various dielectrics (epoxy resins, impregnated oil, Perspex...etc) which exhibited complete insulation breakdown, as well as PD signals generated from different PD sources have been analysed using the approach. Changes in the values of the chromatic parameters are shown to reflect various PD trends and to provide early indications of incipient insulation failure and PD source discrimination. The approach provides a high degree of traceability in relating the chromatic parameters to the raw PD signals.

To my father Houari, my mother Fatna and all my brothers and sisters.

Acknowledgements

I am grateful to Allah the Almighty for giving me the opportunity to do this PhD degree. I am very grateful to my supervisor Professor JW. Spencer for providing me with the opportunity for this research and his inspiration throughout this project. I am deeply indebted to Professor GR. Jones for his significant help, his continuous guidance, advice and encouragement.

It is my pleasure to express my gratitude to Dr. Liwei Hao from the University of Southampton (UK) and Dr. Wayan Ariastina from Udayan University (Indonesia) for providing me with raw PD data. I would like also to thank Professor Trevor Blackburn from the University of New South Wales (Australia) for his collaboration and support.

Special thanks are also due to all the staff at CIMS group, Dr AG Deakin and DH. Smith for their support and assistance.

Special thanks are to my parents, brothers, sisters, friends and to my ex-wife Amanda, without whose patience, encouragement, support and prayers none of this would have been possible.

Contents

List of Figures

List of Tables

Chapter 1

Introduction

ONE of the prime causes of failure in the electrical insulation of high voltage (HV) power equipment arises from partial discharges (PD) that occur in gas filled voids and cavities within solid insulation due to ionisation induced by elevated electrical stresses [10]. Thereafter a progressive deterioration of material may ensue, for example through a treeing process, which finally leads to the failure of the apparatus [11]. Epoxy resin insulated HV equipment is increasingly adopted in power distribution systems because the equipment is more compact and environmentally safer than with oil insulation. However the lifetime of epoxy resins can be considerably shortened due to partial discharge activity [11] which can lead to insulation degradation of the high voltage equipment and ultimately lead to service interruption [12].

Partial discharges can be detected as current (measured in Amps) or voltage pulses (measured in Volts) using a suitable detector circuit. These current or voltage pulses are converted into a charge quantity expressed in pico-Coulombs (pC) [13]. The trend and frequency of PD activity can carry information about the insulation integrity under operating conditions. Therefore PD testing and monitoring has become an important tool for the implementation of predictive and condition-based maintenance [14]

Various methods have been proposed for automating the identification of defects through characterisation of electrical emissions produced by PDs. These methods involve defining pulse shapes, pulse density distribution or in classifying the signals. Examples of such methods are various manifestations of Neural Networks

(NNs), the use of expert systems, classification with fuzzy logic or minimum distance and the deployment of genetic algorithms, 2-D or 3-D pattern recognition techniques or wavelet transform [10] [12] [14] [17][19][22 - 78] However, each of these approaches has one or more limitations so that the quest for methods of improved PD information precessing and extraction continues.

The main objective of this contribution explores the possible use of a different approach for PD information extraction which is based upon chromatic processing [6]. It provides a means for distinguishing between various signals along with a good level of traceability. The approach was originally developed for optical fibre based sensing optical [15] and has been extended for monitoring in the domains of acoustic [16], and radio frequency emissions [17].

The use of the chromatic methodology has been extended to differentiating between PD data generated by different types of PD sources and PD signals progressing -in time or with increasing voltage- towards full electrical breakdown. Both PD data sets were generated under controlled laboratory conditions.

Part of this study was published by the author in [18]. A newer study has been accepted for publication at the Gas Discharge Conference in Beijing in 2012 [19] and another part has been published in Section 4, Chapter 10 in [20].

This thesis is divided into six chapters, including Introduction and Conclusion. Each chapter begins with a short introduction and ends with a summary. Chapter 1 was dedicated to a detailed introduction giving an overview of the research work and thesis and also highlighting the motivating driver behind this research subject.

Chapter 2 gave basic definition of PDs, their types and their measurment techniques and the used instruments. A detailed literature review of the various methods used in PD pattern recognition is given. Examples of the use of the most common methods is given in Appendix E. Definitions of the alternative propsed method, chromaticity, were given in the last part of this chapter.

The processed PD data is presented in Chapter 3. A detailed layout of the various PD data coming from various PD sources and leading to breakdown is given. Chapter 4 contained the pre-conditionning method of the raw PD data, as well as the actual chromatic processing of the data and a detailed layout of the resulting chromatic parameters. In the last part, model signals, imitating most probable shapes of PD signals encountered in real situations, were introduced, chromatically

processed and used as a background for predicting shapes and possible behaviour of real PD signals.

Chapter 5 was dedicated to the discussion of the obtained results from the previous chapter. Various chromatic maps and diagrams of the obtained results were presented, expalined and informative conclusion were drawn. A concise conclusion of the research work undertaken is given in Chapter 6, along with proposed future work which can take advantage of the proposed method or develop its outcomes to furher stages in conjunction with already established methods.

Chapter 2

PD and literature review

2.1 Introduction

PDs are an important aspect in the ageing and the breakdown process of solid or mixed insulation systems. The first part of this chapter defines PDs and describes their occurrence in high voltage equipment and dielectrics, different types of PDs and their causes and effects.

PD measurement is a key task for monitoring HV equipment. Various up-to-date PD measuring methods are also described in this chapter. A comparison between the different measuring methods and the basic IEC 60270 Standards for measuring PDs is made.

Recently, there has been appreciable effort focused on the application of statistical analysis methods and neural networks on partial discharge pattern recognition in order to automate the process and make the latter less subject to interpretational errors by human operators. Previous attempts in employing artificial NNs, Fuzzy Logic and other classifying methods were described.

The last part of this chapter introduces a new processing approach which has hitherto not been used for PD recognition. The approach is based upon what are known as chromatic techniques. The manner in which chromatic techniques can be used for distinguishing changes in signals is described and the quantification of such changes in terms of established chromatic parameters is considered.

2.2 Partial Discharges

PDs are generally initiated if the electrical field strength inside gaseous insulation exceeds the intrinsic field strength of the gas. Partial discharges are defined in the IEC 60270[1] [1] as:

"localised electrical discharge that only partially bridges the insulation between conductors and which can or can not occur adjacent to a conductor. They are in general a consequence of local electrical stress concentrations in the insulation or on the surface of the insulation. Generally, such discharges appear as pulses having a duration of much less than 1 ps."

From a physical point of view, self-sustaining electron avalanches may happen only in gaseous dielectrics [2]. Consequently, discharge in liquids and solid dielectrics may occur in gaseous inclusions, such as voids or cracks in solid materials as well as bubbles in liquids, due to imperfections in solid and liquid dielectrics [2].

Partial discharges are often accompanied by the emission of sound, light, heat, and chemical reactions. The pulse charge of PD can be in the order of a few pC and may exceed 1000 pC [2].

2.3 Types of Partial Discharges

2.3.1 External Partial Discharge "*Corona*"

PDs in ambient air are generally classified as "external discharges" and often referred to as "*Corona* discharges" [2]. Corona is a partially ionised region adjacent to a conductor, initiated at a location of high electric field and causes a gas breakdown between the conductor and the ground. The breakdown decays because the electric field decreases rapidly as a function of distance from the highly stressed position within the system [21].

Corona discharges in ambient air propagating along solid electric surfaces (e.g on transformer bushings and on power cable terminations) may become harmful

[1]The IEC standard refers to PD measurements of electrical apparatus, components or systems tested with AC voltages up to 400 KHz.

because they create an irreversible degradation process due to normal (perpendicular) and tangential field vectors [2]. Such a discharge (*Surface* discharge in air) may bridge long gap distances even if the applied voltage is raised only a few kVs above the inception voltage. Additionally, the solid insulation surface may be eroded progressively due to the local high temperature in the propagating channels [2].

The time scale of corona discharges can vary from nanoseconds to milliseconds or more. Corona tends to be repetitive, as once the region is cleared of charge, the region returns to the conditions which generated the previous corona pulse. Corona in air is sensitive to air velocity and other environmental factors [21].

The present study considers both *Corona* in air and *Surface* discharges in air as studied by Hao *et al* [7].

2.3.2 Internal Partial Discharge

Partial discharges due to imperfection in insulating liquids and solid dielectrics as well as in compressed gas are classified as *Internal* discharges [2]. Partial discharges in solid insulating materials may be initiated in gas-filled cavities, such as voids and cracks (since electron avalanches are only created in gaseous inclusions). In liquid insulators, partial discharges may occur in gas-bubbles due to thermal and electrical phenomena and in water-vapour which may be created in high field regions [2].

A void in a solid dielectric between two electrodes, carrying an AC voltage is subjected to an electric field. If the voltage is increased to generate a sufficiently high field, then a free electron within the void can result in a breakdown of the air within the void. Such a breakdown involves substantial ionisation within the void and these charges will tend to drift to the void walls so as to cancel the field within the void. Thus the field within the void will reduce substantially to sustain the breakdown [21].

The charge flowing from the power supply to the electrodes as a result of the drop in the field within the void caused by the discharge, remains on the electrodes after the discharge extinguishes. This charge flow produces the externally measurable PD signal. The time scale for void-induced PD pulses tends to be 1 to 3 nanoseconds [21].

Another type of Internal discharge occurs in HV equipment when an electrode is adjacent to a point with no well defined electrical potential (e.g. a conductor sliding on an aluminum spacer insert). If the potential difference between the "floating" point and the conductor is sufficiently high to break down the gas gap between them, then a discharge will occur which will tend to equalise the voltage between them. This type of discharge is referred to as a *Floating* discharge.

Internal and *Floating* discharges have been investigated by many researchers (Ariastina *et al* [4], Hao *et al* [7], Lai *et al* [8] and Cavallini *et al* [22]).

2.4 PD measuring circuits and instruments

PD current pulses are characterised by a duration as short as a few ns. Consequently, the frequency spectrum covers the VHF and UHF ranges (up to hundreds of GHz). The shape of such pulses in the time domain may be distorted if traveling from the PD site to the terminals of the test object [2]. However, the current-time integral is more or less invariant. As a consequence, the current-time integral (i.e. charge of the captured PD pulses) rather than the peak value of the PD current pulses, is a most suitable parameter for quantifying the PD intensity.

To ensure reproducible and comparable test results, the PD measuring circuit is specified in IEC 60270, where three basic measuring circuits are recommended. The three circuits, which differ by the arrangement of the measuring impedance Z_m are shown on Figure 2.1 (a), (b) and (c).

The most common circuit employed in practice is shown in Figure 2.1 (a), where Z_m is connected in series with the coupling capacitor C_k. A noise blocking filter Z_n is used to reject the electromagnetic noise coming from the test transformer T_r. The latter is used to provide high voltage potential to create partial discharges in the test object. Care is needed to ensure that the HV leads are PD-free and that the grounding leads are kept as short as possible to minimise the inductance and thus the impact of electromagnetic interference on the PD test results.

The PD detection sensitivity can be substantially increased if Z_m is connected in series with the grounding of the test object, as shown in Figure 2.1 (b). External electromagnetic noise disturbing sensitive PD measurements can also be eliminated to a certain extent if a balanced bridge is employed (Figure 2.1 (c))

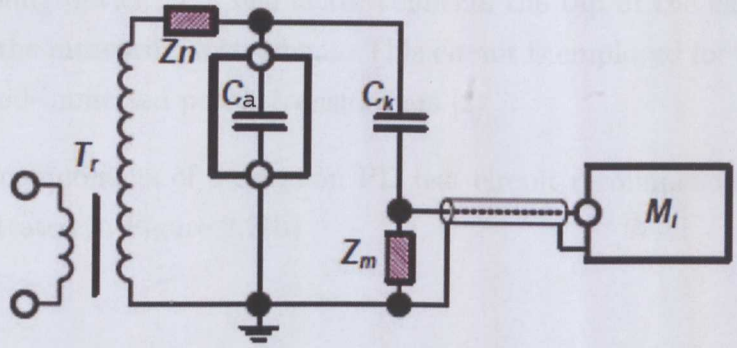

a) Measuring impedance Z_m in series with the coupling capacitor C_k

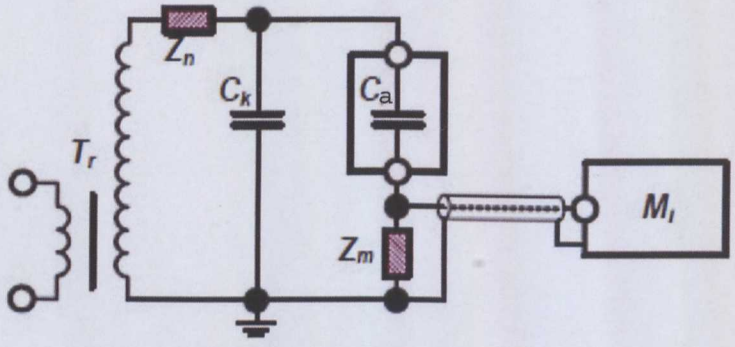

b) Measuring impedance Z_m in series with the test object capacitor C_a

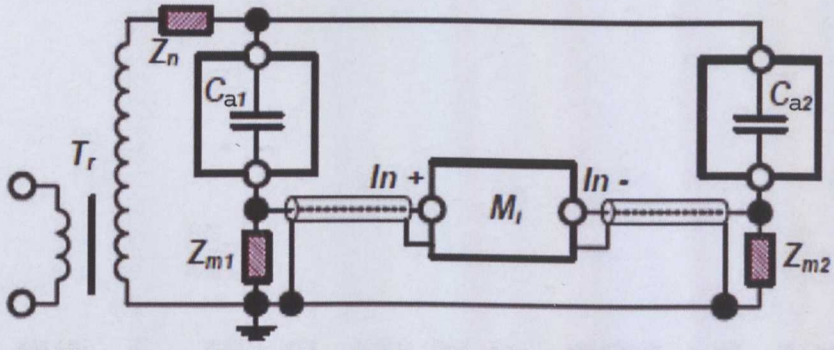

c) Balanced bridge using a reference branch (C_{a2}, Z_{m2}) in parallel to the test branch (C_{a21}, Z_{m1})

T_r – HV test transformer
C_a – Virtual test object capacitance
Z_m – Measuring impedance as part of the coupling device
Z_n – Noise blocking filter
C_k – Coupling capacitor
M_i – PD measuring instrument

FIGURE 2.1: Basic PD test circuits recommended in IEC 60270 [1]

A variant of the PD test circuit reported in Figure 2.1 (a) is the so-called Bushing tap mode, illustrated in Figure 2.2(a). Here the coupling capacitor is represented by the high voltage bushing capacitance C_1, and the measuring impedance Z_m of the coupling device D_c. The latter connects the tap of the capacitive graded bushing to the measuring instrument. This circuit is employed for induced voltage tests of liquid-immersed power transformers [2].

The major components of a common PD test circuit recommended in IEC 60270 [1] are illustrated in Figure 2.2(b)

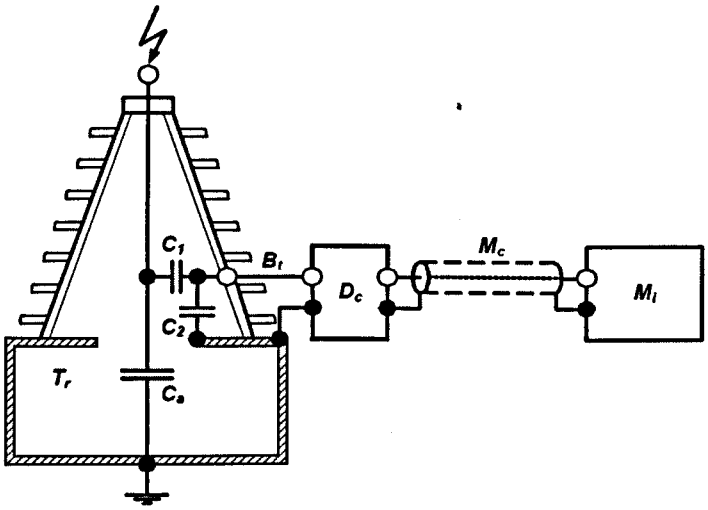

T_r – Transformer under test
C_a – Virtual test object capacitance
C_1 – HV capacitance of the bushing
C_2 – LV capacitance of the bushing
B_t – Bushing tap
D_c – Coupling device
M_c – Measuring cable
M_i – Measuring instrument

(a) Bushing tap circuit recommended in IEC 60270 [1]

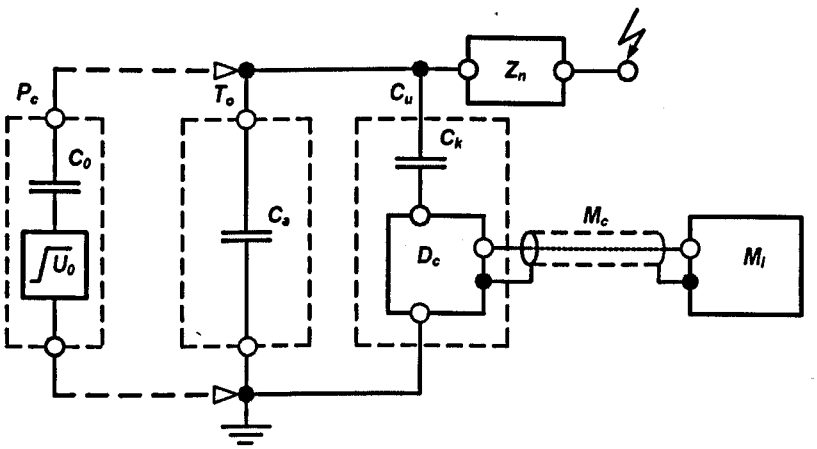

P_c – PD calibrator
C_0 – Calibrating capacitor
U_0 – Step pulse generator
T_o – Test object
C_a – Virtual test object capacitance
Z_n – Noise blocking filter
C_u – PD coupling unit
C_k – Coupling capacitor
D_c – Coupling device
M_c – Measuring cable
M_i – PD measuring instrument

(b) Major components of common PD circuits recommended in IEC 60270 [1]

FIGURE 2.2: PD measuring circuits recommended by IEC 60270

One approach for measuring the apparent charge, is to use conventional analogue PD instruments equipped with a band-pass filter amplifier followed by a peak level indicator. As long as the band-pass filter extracts the measuring frequency in a range where the spectral density of the PD pulses is nearly constant, (Figure 2.3), the PD pulses captured from the terminals of the test object are quasi-integrated. That means the response at the output of the PD instrument and thus the reading of the peak level indicator is proportional to the apparent charge [2].

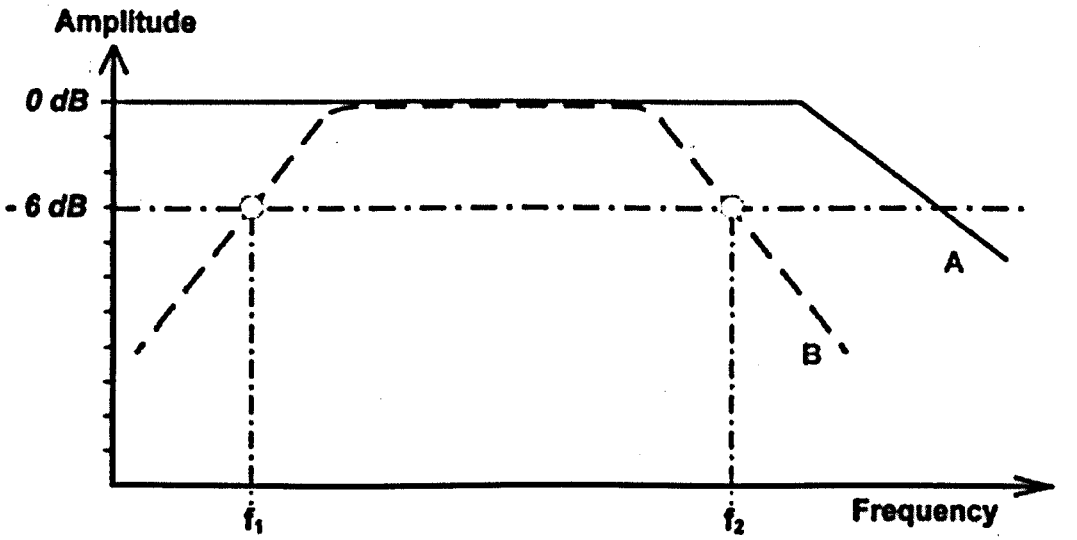

FIGURE 2.3: Principle of the quasi-integration of PD pulses [2]

Another option for measuring the apparent charge is to use a wide band preamplification of the PD signal captured from the test object followed by an electronic integration. This principle offers several advantages not only for the reduction of electromagnetic interferences, but also for the location of PD faults in long power cables [2].

Nowadays the conventional analogue PD pulse processing is increasingly based upon advanced digital techniques. A block diagram for a computerised PD measuring system is shown in Figure 2.4. PD pulses captured from the test object are digitised in real-time, i.e. the band-pass filtering required for the quasi-integration, as well as the peak detection are performed after the A/D conversion using a Field-Programmable Gate Array (FPGA).

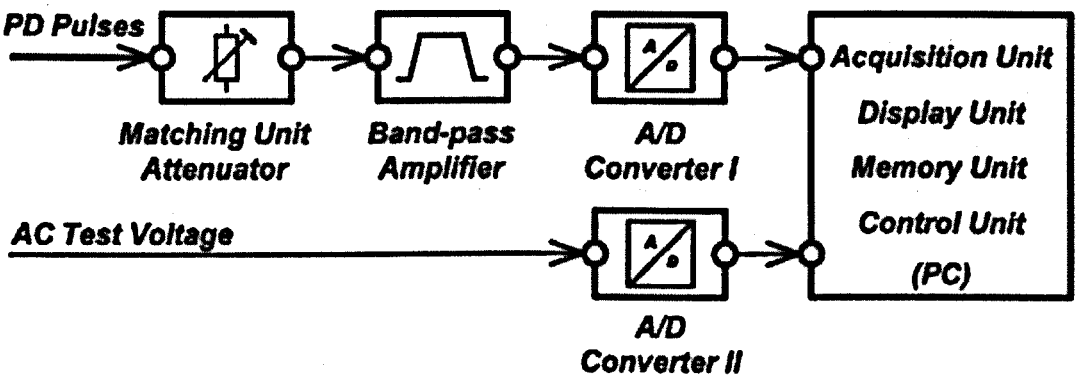

FIGURE 2.4: Bloc diagram of an advanced digital PD measuring system

The main feature of a digital PD measuring system is the ability to store the following characteristic parameters of each PD event:

- t_i time instant of PD occurrence
- q_i apparent charge at t_i
- u_i test voltage magnitude at t_i
- θ_i phase angle at t_i

The vector $[q_i \quad u_i \quad t_i \quad \theta_i]$ stored in the computer memory is utilised for further processing as well as for visualisation of phase-resolved PD patterns.[2]

2.5 Related and derived PD quantities

IEC 60270 standards also recommend the evaluation of PD related quantities other than the apparent charge.

Quantities related to the test voltage are:

- *PD test voltage*: The AC test voltage magnitude applied for a PD test procedure during which PD events exceed a specified apparent charge magnitude.
- *PD inception voltage* V_i: The applied AC voltage at which repetitive occurring PD pulses exceed a specified apparent charge magnitude when the voltage applied to the test object is gradually increased from a level at which no PD events occur.
- *PD extinction voltage* V_e: The applied AC voltage magnitude at which PD pulses of a specified apparent charge magnitude disappear when the voltage applied to the test object is gradually decreased from a level at which PD events occur.

Quantities derived from the PD recurrence are:

Pulse repetition rate n :

$$n = \frac{N_x}{T_0} \tag{2.1}$$

T_0: reference time interval.
N_x: total number of PD pulses within T_0

Pulse repetition frequency N :

$$N = \frac{N_y}{T_r} \tag{2.2}$$

T_r: reference time interval.
N_y: total number of calibrating pulses within the reference time interval.

Phase angle θ_i :

$$\theta_i = (360°) * \frac{\Delta t_i}{T_c} \tag{2.3}$$

Δt_i: time between negative-positive crossing of the applied AC test voltage and a PD pulse.
T_c: time period of one cycle of the applied voltage.

Average discharge current :

$$I = (|q_1| + |q_2| + ... + |q_i|)/T_r \tag{2.4}$$

T_r: reference time interval.
q_i: apparent charge corresponding to PD pulses within T_r.

Discharge power P : Average power of a PD pulse sequence fed into the termination of the test object within a chosen reference time interval T_r divided by this reference time interval:

$$P = (q_1 * V_1 + q_2 * V_2 + ... + q_i * V_i)/T_r \tag{2.5}$$

T_r: reference time interval.
q: instantaneous apparent charge magnitude.
V: instantaneous applied voltage.

2.6 Phase Resolved Analysis

Recently, the use of computer-aided processing techniques have facilitated the automation of PD representation tasks. Phase Resolved Partial Discharge (PRPD) measurement systems have become popular [3]. In such a system, PD pulses are grouped by their phase angle with respect to power frequency of a sine wave. Consequently, the voltage cycles are divided into phase windows representing the phase angle axis (0^o to 360^o).

Standard PD analysis usually applies phase resolved PD distributions, which are the PD pulse heights (measured in *pico*-Coulombs (pC), in Volts (V) or in Amperes (A)) as a function of their corresponding phases of occurrence (in degrees). This is used to extract information about the characteristics of defects as well as PD induced ageing of the insulating materials (Das *et al* [3], Sanjay *et al* [23], Hao *et al* [7] and Ariastina *et al* [4])

The analysis of accumulated discharge data are mainly based on the phase of occurrence. The data are collected during a fixed recording time. Subsequently

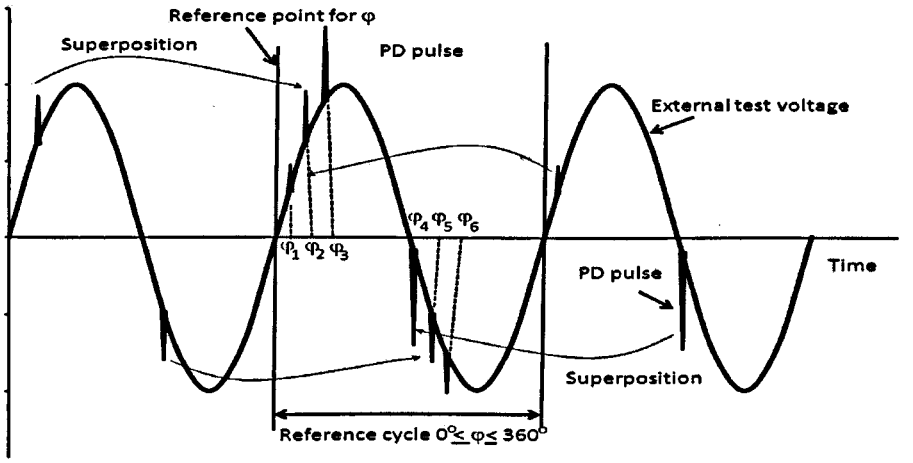

FIGURE 2.5: Basic principle of PD accumulation at each phase angle in a 50 Hz wave [3].

the entire measuring time with numerous voltage cycles is transformed into one reference cycle of the applied voltage, as shown in Figure 2.5 [3]. All discharge pulses are then superimposed within the reference cycle and synchronised to the beginning of this cycle.

A digital PD detector is used for acquiring individual quasi-integrated pulses, and quantifying each of these PD pulses by their discharge magnitude (q in pC), the corresponding phase angle (φ) at which they occur and their discharge rates (n), i.e. number of discharges in a given time interval.

By taking appropriate averages of these statistical distributions, the observed PD patterns throughout the whole phase angle range can be obtained as either, two (q vs φ, n vs φ) or three ($q : n : \varphi$) dimensional patterns.

The bi-variate distribution data (i.e.($q : n : \varphi$) patterns) is considered as one of the more complete forms of graphical representation of a PD pulse distribution. Three main distributions can be derived indirectly from the ($q : n : \varphi$) plots:

1. The distribution of the pulse number (n) vs. pulse amplitude (q), i.e. ($n : q$)
2. The distribution of the pulse number (n) vs. phase of occurrence (φ), i.e. ($n : \varphi$) and
3. The distribution of the pulse amplitude (q) vs. phase of occurrence (φ), i.e. ($q : \varphi$).

Figure 2.6 shows a typical $(q : n : \varphi)$ three dimensional representation of the PD activity in a highly contaminated oil at 5 kV taken from [4]. This shows the phase of occurrence (φ), induced charge (q) for each PD event and number of such pulses (n) that occurred during the measuring time. This represents the most popular pattern representation used in all standard PD analysis.

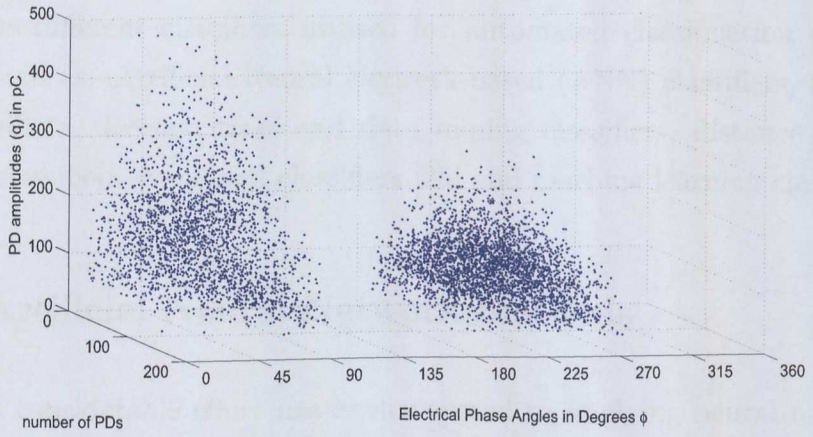

FIGURE 2.6: 3D pattern of PD activity in Highly Contaminated Oil at 5 kV over a 3 minute period [4].

2.7 Methods used for PD pattern recognition

Various methods have been proposed for automating the identification of defects through characterisation of the electrical emissions produced by PDs. These methods involve defining pulse shapes and pulse density distribution in classifying the signals.

An automatic pattern classification system generally consists of two distinct entities: a description unit for extracting appropriate features from the raw data and a classification unit for assigning patterns to a particular class [24].

An effective description unit should extract from the raw data the information, which is most relevant for classification purposes. It should also produce features of the input data, which distinguish pattern classes from each other; the dimensionality of data must be also reduced [24].

The most commonly used PD pulse characteristic descriptions are:
1) discharge pulse/phase distribution,

2) discharge pulse shapes, and
3) hysteresis traces of maximum discharge magnitude as a function of the applied voltage [24].

Given the appropriate PD pulse behavior and characteristic features, the most crucial step in pattern recognition rests on the classification procedure [24].

Most of the different classifiers utilised for automated classification of PD can be categorised as: Artificial Neural Network-based (ANN) classifiers, fuzzy logic based classifiers, decision trees and data mining classifiers, distance classifiers, statistical classifiers, combined classifiers [25] and machine learning classifiers.

2.7.1 Artificial Neural Network methods

Recently, a considerable effort has been devoted to applying neural networks to the recognition of partial discharge pulse patterns in order to identify various discharge sites and the associated cavity sizes in electrical power apparatus and cables, that may eventually lead to electrical breakdown [26] - [27]. ANNs are mathematical models designed to imitate human brain operation. Neural networks are parallel processing configurations using Neurons as the main building blocks. ANN architectures are created by interconnecting these building blocks. Computation neuron sums N weighted inputs and outputs the result through a non-linear function. Data flows through this series of non-linear transformations (e.g., sigmoid), in one or more stages in an assigned topology of ANN. Knowledge in the training set is extracted and stored in the connection weights and neuron biases during a learning phase. Categorisation of ANNs is based on the method of training, network topology and algorithm used in training.

There are several different types of ANN structures used in PD recognition which include (but not limited to) the following: Back-Propagation Neural Net, Kohonen, Self-Organising feature map, Learning Vector Quantisation Network, Modular and Cascaded Neural Nets [25]. When ANNs are used to characterise PD signals, and during the learning phase, they are usually trained using PD feature vectors which have resulted from:

- Statistical features of the PD pulse shape; Skewness, Kurtosis, Mean value...etc [14] [27] [28] [29] [30] [31] [32].

- Features based on signal processing algorithms (Wavelet Transform, Fourier Transform..etc) [33] [34] [35] [36].
- Pulse shape features of the PD pulse, Magnitude, Risetime, Falltime, Width, Area [10] [37] [38] [39].
- Phase resolved analysis of the PD pulse; PD magnitude, Phase angle and Discharge count [26] [22] [40].

An example of the use of an ANN (Back Propagation Network) in PD signal recognition is given in Appendix E.

The accuracy of ANNs depends upon the input PD features vector, hence the best feature extractor function is the mapping tool that provides a compact meaningful representation of the measured PD pulses [32].

Abdel-Galil et al [25] report for an investigation carried out without any statistical preconditioning that, even with the simplest of partial discharge sources, (e.g. artificially prepared cylindrical cavities and well defined electrical trees) the neural networks perform adequately, but they are generally incapable of achieving perfect distinction between even these idealised discharge sources with known geometry [38] [41] [42], notwithstanding the long times required to train them.

Also, two identical cavities located at different sites such as in the case of a transformer, will not be recognised as equal in size. The PD pulses from the site situated further away deep in the windings will have lower detected amplitudes and slower rise times due to the transmission line behavior of the windings [25].

Consequently, a much lower degree of pattern recognition performance may be anticipated with actual physically real cavity occlusions of varied size and irregular geometry, and which may be dispersed in varying degrees throughout practical insulating systems of high-voltage power apparatus of different design and configuration [10].

Furthermore, ANNs "learn" via training examples and are incapable of giving explanations of the criteria upon which their decision-making is based [43],i.e they lack of traceability.

Kranz *et al* [44] state that the ANN classifiers still have no or only a conditional degree of traceability .

Salama *et al* [10] have extended the studies of [38] [42] to comparing the recognition capabilities of Learning Vector Quantisation, Nearest Neighbor Classifier and Multi-Layer Perceptron neural networks. They demonstrated that no substantial difference existed between the partial discharge pattern recognition capabilities of these prime neural networks when applied to identify simple discharge sources, (e.g. [45]). The topology of the Multi-Layer Perceptron network was altered by the usual trial and error techniques to arrive at the appropriate number of inputs and nodes in the hidden layers to yield optimum performance of the neural network .

Also, the training procedure of neural networks is relatively slow, and the training data must be sufficient and compatible [10].

Wang *et al* [14] report that the convergence of learning of an ANN is influenced by the network topology and values of learning parameters. A further limitation of the traditional NN is the inability to produce linguistic output, because it is difficult to understand the content of the network memory.

2.7.2 Fuzzy Logic based methods

Fuzzy Logic (FL) can be considered as an extension to crisp set theory (in which the degree of membership of any object in the set is either 0 or 1) [46]. FL allows partial set membership rather than crisp set membership (1) or non-membership (0) [46]. The FL model is experimentally based, relying on an operator's experience. FL does not require precise inputs. It is inherently robust, and can process any reasonable number of inputs. Fuzzy systems rely on a set of "*if-then*" rules [25].

PD classification using fuzzy logic is based on the assumption that the various PD signal feature parameters are not crisp values (0 or 1); rather they should be more effectively and naturally treated as fuzzy variables such as small, medium, and large [39] [22] [47]. Thus, the feature parameters are mapped to the membership values to different fuzzy sets defined over their respective domains. The basic steps involve fuzzification of features, an inference engine, and a defuzzified output. The identification of the PD source is obtained from the defuzzified output [39]. An example of the use of FL in PD signal recognition is given in Appendix E.

Another method based on FL, the fuzzy c-means clustering algorithm, which is also one of the most popular fuzzy clustering algorithms [48]. Fuzzy c-means clustering

algorithm has been applied for pattern recognition for PD of Cast Resin Current Transformers (CRCT) [49]. It has been used with an Inductive Learning (decision tree) approach for PDs in High Density Polyethylene (HDPE) cables [37] [43], or combined with a Generic Algorithm (GA) approach for PD signals of CRCT [50].

Expert Systems are used for processing information of the type "assumption-hypothesis", i.e. the "$if - then$" type of decisions, similar to FL. Expert Systems evaluate the individual diagnostic methods, make correlations between them, use knowledge from previous measurements and evaluations and provide expert propositions. Several Expert Systems have been developed for the diagnostics of insulation systems by characterising the PD signals [51].

The fuzzy approaches and expert system require human expertise, and have been successfully applied in PD pattern recognition. However, there are difficulties in acquiring knowledge and in maintaining the database [30].

ANNs can directly acquire experience from the training data, and overcome some of the shortcomings of the expert system. However, the training data must be sufficient and compatible -which is not the case in real situations- to ensure proper training in traditional ANNs [14].

2.7.3 Decision trees and data mining methods

Data Mining (DM) is the process of discovering new patterns from large data sets involving methods from statistics, artificial intelligence and databases [52]. Decision Trees (DT) are classification algorithms used in data mining and machine learning to create knowledge structures that guide the decision making process [53].

Rule based systems for PD pattern analysis rely upon the development of a set of rules that describe the experience related knowledge used by human experts. The human expert provides the reasoning behind the classification decision, which permits a computer program to be designed which incorporates the experts reasoning in a form of a set of rules. The use of data mining approaches such as decision tree [37] [54] [55] may avoid the need for stipulating such rule by enabling these rules to be generated directly from a stored database of PD pulses.

The rules obtained rely mainly on features, which are based on the feature extractors of the PD pulse shapes. These are difficult to identify even by the experts

due to the overlapping characteristics of the attributes that describe the pulses associated with different PD cavity sizes [25]. This tends to render the approach less accurate in discriminating between PD signals generated from various PD cavity sizes. An example of the use of a data mining technique (decision tree using genetic algorithm) in PD signal recognition is given in Appendix E.

2.7.4 2-D / 3-D Wavelet Transform classifiers

A wavelet, as its name implies, can be interpreted as a small wave (mother wavelet) that has a limited duration and a zero mean value. It oscillates in amplitude and decays to zero quickly on both sides of the central position of the waveform [56].

Wavelet analysis is a method which has been used in PD pattern recognition. It has been used for time-frequency analysis in fault diagnosis [33] [36] [57] [58] [59], and as a PD pulse features extractor in the time-frequency domain for the pre-processing stages of ANNs [34] [35] [36].

The use of Discrete Wavelet Transform (DWT) for the pre-processing of PD patterns as proposed in [34] [35] [36] enhanced the capability of PD pattern classification methods. However its limitations in how to apply wavelet transform and how to extract feature vectors led to an improved but not ideal recognition result [35].

The DWT method also lacks shift invariance, which means that small shifts in the input signal can cause major variations in the distribution of energy between DWT coefficients at different scales [59]. Xie *et al* [59] addressed this problem by introducing a Complex Wavelet Transform (CWT). However, this could not overcome the problem. Moreover, when the DWT is used for the analysis of PD signals, it is vital to select the most appropriate wavelet function (mother wavelet) concerning the shape of PD signals.

Since the DWT pattern is strongly related to the shape of the mother wavelet, there are often two essential problems which are associated with its use in practical measurement situations. First, because of the dependence of the detected signals shape upon the experimental measuring set up and PD sources they are likely to have different pulse shapes. Secondly, if the measured PD signals are non-stationary -which is the case in online monitoring- or maybe nonlinear, an adaptive self-tuning wavelet will be required [56].

Other authors have described 2-D pattern recognition techniques [60] [61] [31]. However, these techniques sometimes fail to extract important information and lead to a lower recognition rate than is expected. This is particularly true for cases involving multiple sources [35]. 3-D pattern recognition techniques have been proposed but their correct recognition rate can only reach 70-90 % [62]. This is mainly due to limitations of their feature extraction methods [35].

2.7.5 Distance based classifiers

Distance based classifiers measure all the distances between the unknown PD signal to be classified and a set of labeled classes stored in a reference library. The classifier then assigns the unknown PD signal according to the nearest class to the unknown signal. The principal algorithms under this group which have been utilised for PD patterns are: minimum distance classifiers [63] [64], nearest neighbor classifier and fast match classifiers [24] [44] . Distance classifiers have also been used in locating PD signals within transformers windings [65].

Distance classifier operates better if the chosen features are uncorrelated and if they have equal weight in classification [25]. Distance classifiers have been used in the second step of the PD pattern recognition process, after the PD features extractors. this renders their effectiveness to be tied to the PD features extractors' performance e.g Principal Component Analysis (PCA) [66], Wavelet Transform [35]...etc

2.7.6 Mixed methods

Much research work in the area of machine intelligence focused lately on integrating two or more intelligent techniques to obtain a hybrid model of improved numerical convergence or better classification capability. For example in [37] and [43] a fuzzy inference system for PD pulse pattern recognition which is tuned by utilising decision trees is introduced.

Wang *et al* [14] proposed an Extension-Neural Network (ENN) method which combines Extension Theory (which is an express system of knowledge which regards

matter-element and case-element as logic cell [67]) with a Neural Network architecture. The method uses an extension distance instead of using Euclidean distance (ED) to measure the similarities between tested data and a cluster domain.

Salama *et al* in [10], described a procedure that was based on an autoregressive (AR) time-series analysis concept applied to establish the appropriate number of inputs of an ANN. Since the AR time-series model functions in specific time steps, it was deemed to be particularly applicable to the highly time dependent PD patterns. The procedure represented the first systematic attempt made to devise a neural-network topology with specific application to partial discharge pattern recognition.

ANNs were also combined with various classifiers and features extractors in order to enhance the PD pattern recognition capability of the method used; with distance classifiers [44] [24] and with features extractors; with wavelet transform in [35] [34] [36] and with PCA in [68].

Linear discriminant analysis (LDA) [69] is a another classifier that has been used in combination with PCA, as a feature extractor, in PD pattern recognition [63] [70].

The use of a combined classifier can boost PD pulses classification accuracy since in this case, it may mimic a group of experts in identification and classification of PD pulse and its possible associated source [25]. However, the shortcomings of any block from the PD pattern recognition chain (features extractors or/and classifiers), will eventually impact on the overall performance of the process.

2.7.7 Support Vector machine

A more recent method used in the identification of PD patterns is the so called machine learning method and in particular the Support Vector Machine (SVM). The SVM uses the concept of Kernels for a number of learning tasks and has shown better performance than neural networks in a variety of fields [71]. The SVM is a method for finding functions from a set of labeled training data. The function can be either a classification function or a regression function [72].

Results of using SVM for several feature extractions have been published in [7] [73] [74] [75] [76] [77], and a comparison study between SVM and a probabilistic

neural network (PNN) was conducted by Hunter *et al* in [78]. An example of the use of SVM in PD source discrimination can be found in Appendix E.

Both the SVM, as the classifier engine, and the feature vector extractor, whether it be a wavelet transform, statistical analysis, PCA...etc, require optimisation because of the overlapping characteristics of PD pulses associated with different PD cavity sizes and locations, which Hao *et al* encountered in their research work; [7] [73] [74] [75] [76] [77]. Such a process affects the overall performance of the recognition method. As for applies to ANNs, SVM classifiers have no or only a conditional traceability.

2.8 Chromatic methodology

Chromatic intelligent monitoring relates to vision and optics, both literally and metaphorically. Physically, human vision is based on rods and cones in the eye (sensors and filters) responding to visible light of different wavelengths (colour) to provide signals conveying information in terms of the primary colours red, green and blue. In connection with information, the concept of vision is also generally used in a metaphorical sense, for example in terms of data visualisation, information picture, supervision, and zooming to different scales and levels. Being based on colour science, chromatic processing applies physically to signals and metaphorically in the information domain to aid in the interpretation of the significance of the signals. Figure 2.7 illustrates the combined approach [79].

With reference to Figure 2.7(a), the information in the signal is abstracted - and compressed - by the application of three filters, here with Gaussian responses, as those of the human eye when acquiring red, green and blue wavelengths.

Owing to the similarity with human vision, the chromatic filters are referred to simply, and arbitrarily, as R (red), G (green) and B (blue). The responses (filters) are overlapping. This non-orthogonality enhances sensitivity to changes in the overlapping regions [6].

As a result of chromatic processing with R, G and B filters, a complex signal in an α domain may be characterised by just three values, R_0, G_0, B_0. These values may be transformed via algorithms from colour science into other representations that

emphasise different relationships emerging from the relative proportions of R_0, G_0, B_0, for example the HLS representation (Hue, Lightness and Saturation)[79].

The chromatic methodology, of which colour science is a special case, has advantages of using simple algorithms and traceable processing [80]. The chromatic processing involves two main procedures [81]: chromatic filtering and chromatic transformation.

2.8.1 Chromatic filtering

Chromatic filtering often involves the cross correlation of a signal with the responsitivity of each of three non-orthogonal (overlapping) detectors, referred to as tristimulus filters. Different detector response shapes may be used. For example, a Gaussian shape (Figure 2.7(a)) is commonly applied, aligning with the Gabor transform [82]. For computational simplicity, a triangular shape (Figure 2.7(b)) may be preferred.

Koh *et al* [83] states that in practise, the truncated triangular filters (Figure 2.7(b)) are ideal for the processing of chromatic results from discrete data sets where a component of the data can be independent from another data point. Truncated triangular filters are also efficient because of their high sensitivity when the tails of the signal are of importance.

On the other hand for continuous data, three Gaussians of the form shown in (Figure 2.7(a)) are more practical because filter arrangements can be tailored to discriminate the data more at the centre of the Gaussian with less emphasis on the tail region.

As mentioned above, addressing a signal as in Figure 2.7 with three non-orthogonal processors, yields three outputs, R_0, G_0, B_0 which represent the signal distribution. They are calculated by the convolution of the PD signal with respect to the response of each processor using the formulae:

$$R_0 = \int R(\alpha)P(\alpha)d\alpha$$
$$G_0 = \int G(\alpha)P(\alpha)d\alpha$$
$$B_0 = \int B(\alpha)P(\alpha)d\alpha$$

where P is a random signal in the α domain, and $R(\alpha)$, $G(\alpha)$, $B(\alpha)$ are the responses of each processor with respect to α.

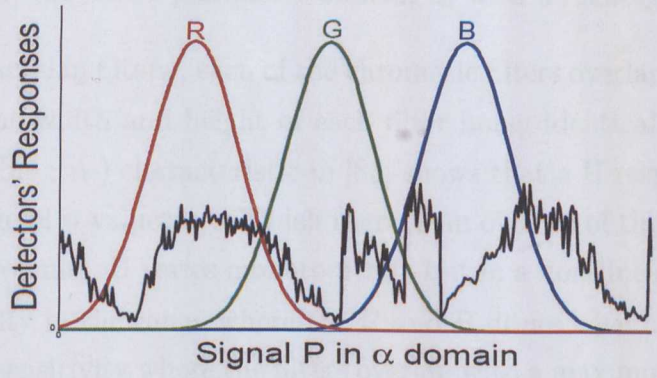

(a) Gaussian shape.

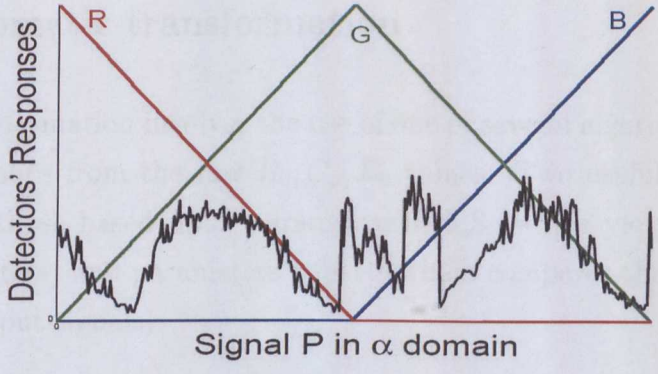

(b) Triangle shape

FIGURE 2.7: Tristimulus filter construction.

Whatever the filter shape, the non-orthogonality in the parameter domain α (e.g. time, frequency, phase...etc) is significant in cross correlating the subdivided signals on each channel and in providing a means of sensitively tuning via the regions of overlap. In this manner, a signal having a complex structure can be conveniently represented by only three parameters calculated from the three processors (R, G and B) [81].

Koh *et al* also states that the resulting (Hue : α) characteristic in the case of truncated triangular filters is highly linear extending throughout the α range covered by the three-filter responses. Tests in [83] show that the best linearity occurred when the individual filters were spaced 2 * r apart (r = half width of filter) with the filter crossing points located at 0.07 of the maximum height (Figure 2.7(b)). Filters implemented in this way give a result that is unconditionally

linear throughout the entire parameter domain α, with no ambiguities [83].

In the case of Gaussian filters , each of the chromatic filters overlapped at their half height values, the width and height of each filter being identical (Figure 2.7(a)). The resulting (Hue : α) characteristic in [83] shows that a H response is only obtained for a range of α values over which there is an overlap of the filter responses. In between these limits, H varies monotonically but in a non-linear manner with a reduced sensitivity in the range where the R and B filters have minimal response and the highest sensitivity where the filters overlap with a maximum rate of change [83].

2.8.2 Chromatic transformation

Chromatic transformation involves the use of one of several algorithms for producing chromatic maps from the raw R_0, G_0, B_0 values. Two useful forms of transformations are those based upon parameters H,L,S (which yields signal feature defining parameters) and parameters x, y, z, (which compares the relative magnitudes of the output signals)

2.8.2.1 Basic HLS transformation

The HLS method is based upon the Hue-Lightness-Saturation scheme of colour science. [5].

The outputs from the cross correlations between an unknown signal and the different responses of each of the three R, G, B processors (Figure 2.7) are transformed to yield signal structure information via the chromatic factors H, L, S. These represent: the dominant value of the signal parameter (Hue, H); the signal strength (Lightness, L); and the spread or the range covered by the signal in the parameter domain (Saturation, (1-S)) [5] where:

$$\mathrm{H}^{2}\begin{cases} 240 - \frac{120\times g}{g+b} & \text{if } r = 0 \\ 360 - \frac{120\times b}{b+r} & \text{if } g = 0 \\ 120 - \frac{120\times r}{r+g} & \text{if } b = 0 \end{cases}$$

with:

[2] 240, 360 and 120 will place Red at 0° / 360°, Green at 120° and Blue at 240°.

$$\begin{cases} r = R_0 - min(R_0, G_0, B_0) \\ g = G_0 - min(R_0, G_0, B_0) \\ b = B_0 - min(R_0, G_0, B_0) \end{cases}$$

$$L = \frac{R_0 + G_0 + B_0}{3} \tag{2.6}$$

$$S = \frac{Max - Min}{Max + Min} \tag{2.7}$$

where Max and Min refer to the maximum and minimum values respectively of the parameters R_0, G_0, B_0. The latter are typically normalised to the range [0-1].

The signal can be represented by the coordinates H, L, S on two-dimensional chromatic maps in the form of H - S and H - L polar diagrams where H is the azimuthal angle, S or L is the radius with : H = $\theta \in [0^o, 360^o]$) and r = S or r = L $\in$ [0, 1] (Figure 2.8(a)). The H, L, S cordinates can also be represented in three dimensional space (θ, z, r) (Figure 2.8(b)).

On Figure 2.8(a), the chromatic boundary encompassing all signals remains fixed as a circle of unity radius [84]. Physically, the radii on these diagrams represent the signal strength (L) or its spread (S). Thus, for the H - S curve, S = 0 represents a signal spread across the entire signal parameter range, whereas S = 1 represents a monochromatic signal. In the H - L diagram, L = 0 indicates a signal strength approaching zero.

An important aspect of such signal representation on the chromatic maps is that the relationship between two signals is easily visualised and the superposition of two complex signals can be conveniently determined using simple moment equations [5].

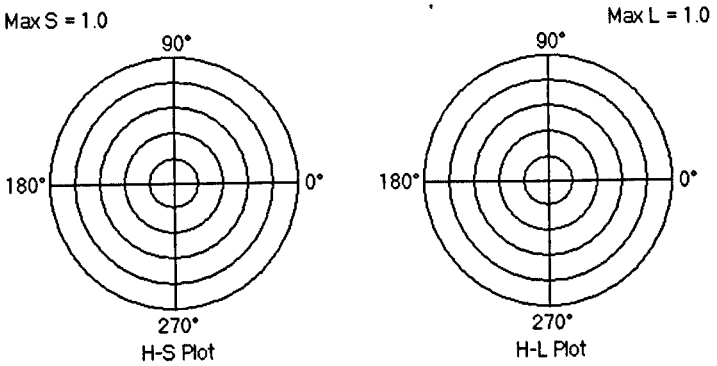

(a) 2D H-S and H-L polar plots.

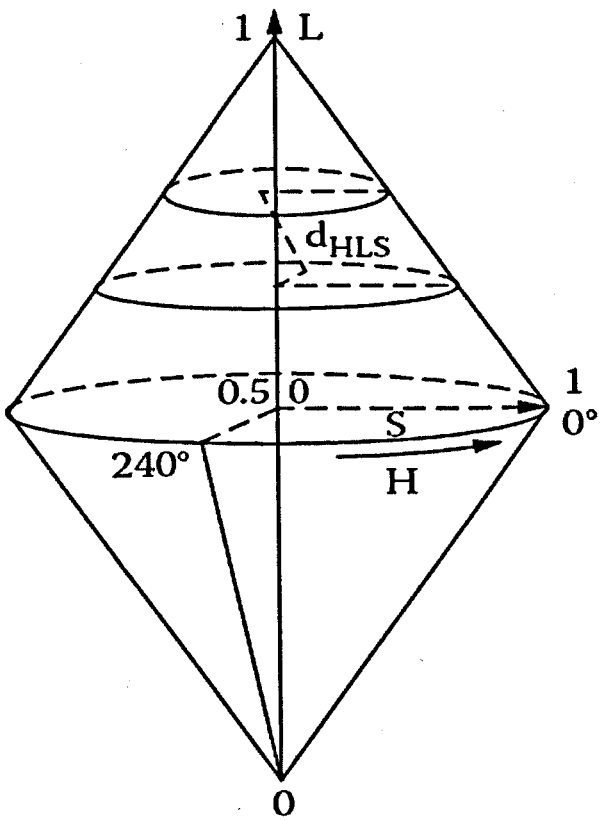

(b) 3D HLS representation

FIGURE 2.8: Chromatic map basic components

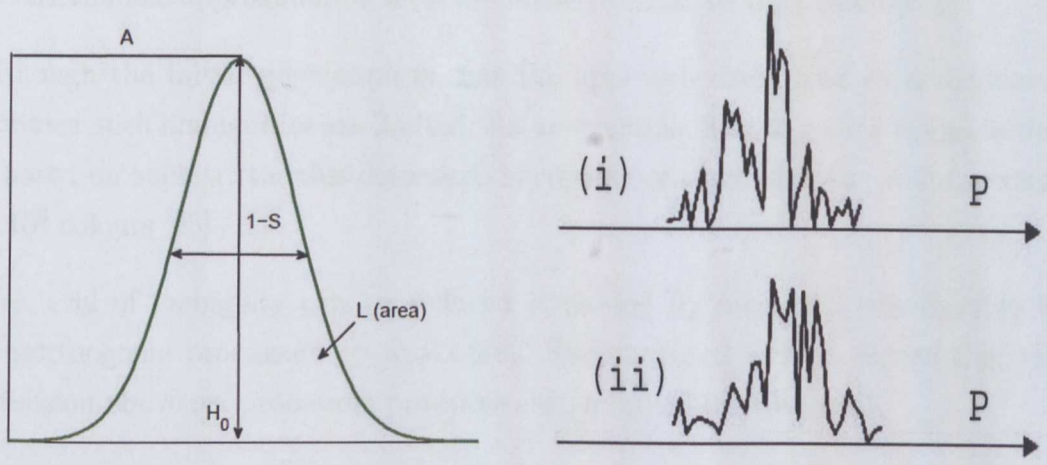

(a) Chromatic domain

(b) Laboratory frame

FIGURE 2.9: Equivalent chromatic Gaussian representation of real complex signals following chromatic transformation [5]

As an aid to comprehending the significance of this description, we may envisage a space within which all signals as perceived by an observer to take the form of a Gaussian envelope (Figure 2.9 (a)) and defined mathematically by [85]:

$$g = A * \exp[-\frac{1}{2}(\frac{(H - H_0)}{S})^2] \tag{2.8}$$

This function g and hence the perceived signal is completely defined by only three variables; the Hue H_0 (location of its maximum value), the Saturation S (its width) and A (its amplitude). A and S govern the area covered by the envelope which is related to the Lightness L (its strength). Consequently, in Gaussian signal space, each signal as seen by the perceiver is defined unambiguously by only three parameters H, L and S.

Figure 2.9 (b) shows two possible signals in the parameter domain P. Although the first signal (i) (Figure 2.9 (b)) is clearly non Gaussian in detail, nonetheless sampling it with a tristimulus system ascribes it to the perceived Gaussian family designated by the curve on Figure 2.9 (a).

Similarly, the second signal (ii) (Figure 2.9 (b)) shows a different non Gaussian signal but which when addressed by the same tristimulus filters could yield identical H, L, S values, indicating that both signals, although different in reality, at

the tristimulus approximation level are indeed similar to the perceiver [5].

Although the initial perception is that the approach could lead to ambiguities. However such ambiguities are limited. As an example, human colour vision, which is based on such tristimulus detection, is capable of discriminating well in excess of 10^6 colours [85].

The level of ambiguity can be reduced if needed by increasing the number of non-orthogonal processors up to six [86]. Stergioulas *et al* have shown that the extension above six processors produces only minimal improvement.

2.8.2.2 Basic xyz transformation

An alternative transformation is the x, y, z transformation on which the CIE diagram of color science is based, Figure 2.10 (a) [87].

The x, y, z are defined in terms of the outputs of the three chromatic processors R, G and B by the equations [88]

$$x = \frac{R_0}{R_0 + G_0 + B_0} \tag{2.9}$$

$$y = \frac{G_0}{R_0 + G_0 + B_0} \tag{2.10}$$

$$z = \frac{B_0}{R_0 + G_0 + B_0} \tag{2.11}$$

so that

$$x + y + z = 1 \tag{2.12}$$

The CIE chromaticity diagram is a Cartesian representation in terms of $x : y$ (Figure 2.10 (a)) with z being implied via Equation 2.12 [5]. The diagram boundary represents maximum saturation for the spectral colors, and the diagram forms the boundary of all perceivable hues [5].

The $x : y$ diagram thereby gives an indication of the relative contribution of each part of the signal covered by a chromatic processor (R,G or B) with respect to the other parts.

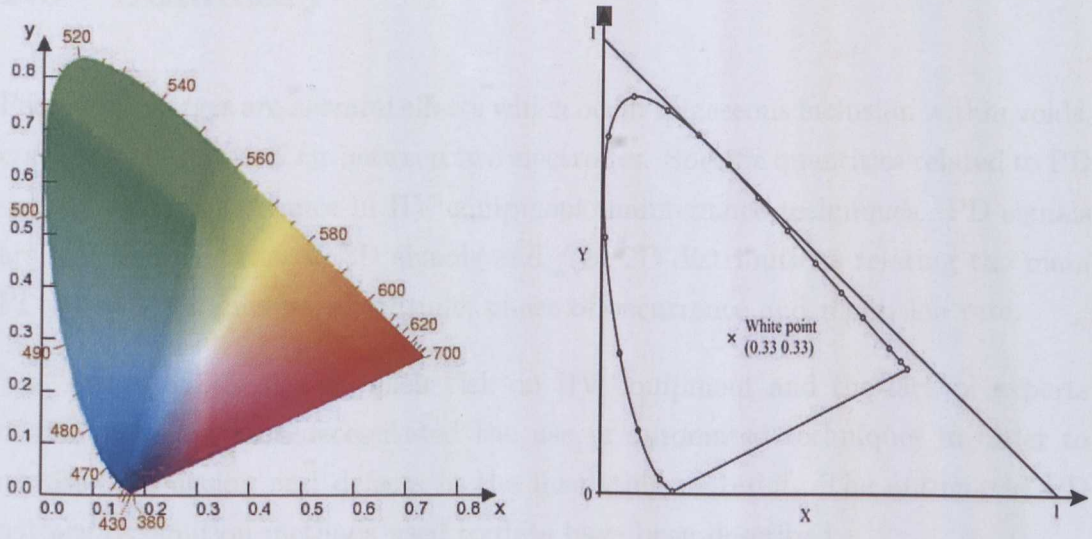

(a) Colour and wavelengths

(b) X:Y representation

FIGURE 2.10: CIE diagram [6]

A further parameter L as defined by Equation 2.6 is also relevant to indicate the lightness (i.e. the signal strength). The monochromatic signals lie on the periphery of the color space defining curve of Figure 2.10 (b).

The point corresponding to $R = G = B$ (i.e. $S = 0$ in HLS space) has coordinates (0.33, 0.33) in the xyz system (Figure 2.10 (b) (*aka* white point)).

The present work shows how these concepts of chromaticity can be deployed for analysing PD signals.

2.9 Summary

Partial discharges are harmful effects which occur in gaseous inclusion within voids, crack, air bubbles and air between two electrodes. Specific quantities related to PD signals are of importance in HV equipment maintenance techniques. PD signals are represented either in 3D signals and / or 2D distributions relating the main PD activity parameters; amplitude, phase of occurrence and repetition rate.

The nature of PD signals, their risk on HV equipment and the lack of experts of PD pulse patterns necessitated the use of automated techniques in order to monitor the ageing and defects in the insulating material. The automated PD pattern recognition methods used to date have been described.

The chromatic methodology, which includes two main procedures of non-orthogonal chromatic filtering and chromatic transformation, has been introduced. It has the advantages in dealing with complex signal/data in a traceable manner.

Data sets containing a complex level of information may be probed using chromatic algorithm to unveil different levels of hidden information and to quantify those levels for relative comparison purposes.

Chapter 3

Processed data

3.1 Introduction

This chapter describes the raw PD signals for different operating conditions, obtained from reported data [4] [7] (raw data obtained from authors) and [8] [22] (data digitised from publication by authors, Appendix D). The diversity of the data sources highlights the generic aspect of the chromatic methodology as a holistic approach to PD signals monitoring. The data have been preprocessed for chromatic analysis.

The signals are presented in two groups; those concerned with PD signals obtained from different kinds of PDs, and those obtained from the same PD source but at different applied voltages leading eventually to full electrical breakdown [4] [7] [8] [22].

In the first group, PD activities were from Corona, Surface, (Section 2.3.1) Internal, Floating in oil, new and contaminated oil, and oil with paper insulation layer (Section 2.3.2).

In the second group, PD activity is considered for the time variation of PD activity from a needle-plane epoxy resin geometry [8], a needle-plane XLPE cable source at approximately the same voltage but as electrical treeing occurred and for increasing voltages in contaminated oil [22].

A summary of the conditions addressed is given in Table 3.1.

TABLE 3.1: Summary of PD activity data preprocessed

PD signals groups	**Applied Voltages**	**Source PD data**
1^{st} Group: PD signals obtained from different sources:		Hao *et al* [7]
Corona PD	6.9,8 and 10 kV	
Internal PD	21 and 24 kV	
Floating on oil PD	23 and 25 kV	
Surface PD	6 and 9 kV	
PD in oil (New + Aged) and paper insulation	15 and 18 kV	Ariastina *et al* [4]
2^{nd} Group: PD signals leading to breakdown:		
PD activity with time	11 kV	Lai et al [8]
PD activity with voltage:		Ariastina *et al* [4]
PD in Moderately contaminated oil	3,4,5,6 and 7 kV	
PD in Highly contaminated oil	3,4 and 5 kV	
PD activity with time and voltage	7 and 8 kV	Cavallini et al [22]

The preprocessing of the data involved taking the average value of the PD amplitudes with each 1^o degree interval, this value is then added to the Standard Deviation of the PDs of the same interval to produce graphical representations based upon the PD activity in terms of pC charges as a function phase angle during the two half cycles of the applied alternating voltage oscillation [18]. Significant features on these various graphs are highlighted.

3.2 PD signals from different sources

3.2.1 PD activity in basic geometries

Four different artificial PD sources to simulate four typical PD types existing within power equipment have been used by Hao *et al* [7]. Conventional PD detection (Robinson PD detector) as well as a radio frequency current transducer (RFCT) were used to detect PD signals [7].

In order to generate partial discharge data from these PD sources, a simple experiment has been designed by Hao *et al* [7]. One potential PD measurement point is at the bushing tap of high voltage apparatus such as large auto-transformers. The discharge current flowing to earth can be measured at the bushing tap point using a radio frequency current transducer (RFCT). This approach has been applied to on-line PD monitoring of power transformers in the field [89].

3.2.1.1 Artificial PD Source Models

Four PD source models (Figure 3.1) have been deployed by Hao *et al* [7] in order to generate different types of PD signals for simulating common PD events which can occur within an oil filled power transformer.

Figure 3.1 (a) illustrates a system for producing a corona using a length of thin aluminum wire suspended from a high voltage electrode and lying above a grounded plane.

A surface discharge was simulated by using a needle as the high voltage electrode, a plane as grounded lower electrode and a piece of perspex as an insulation block between those two electrodes (Figure 3.1 (b)).

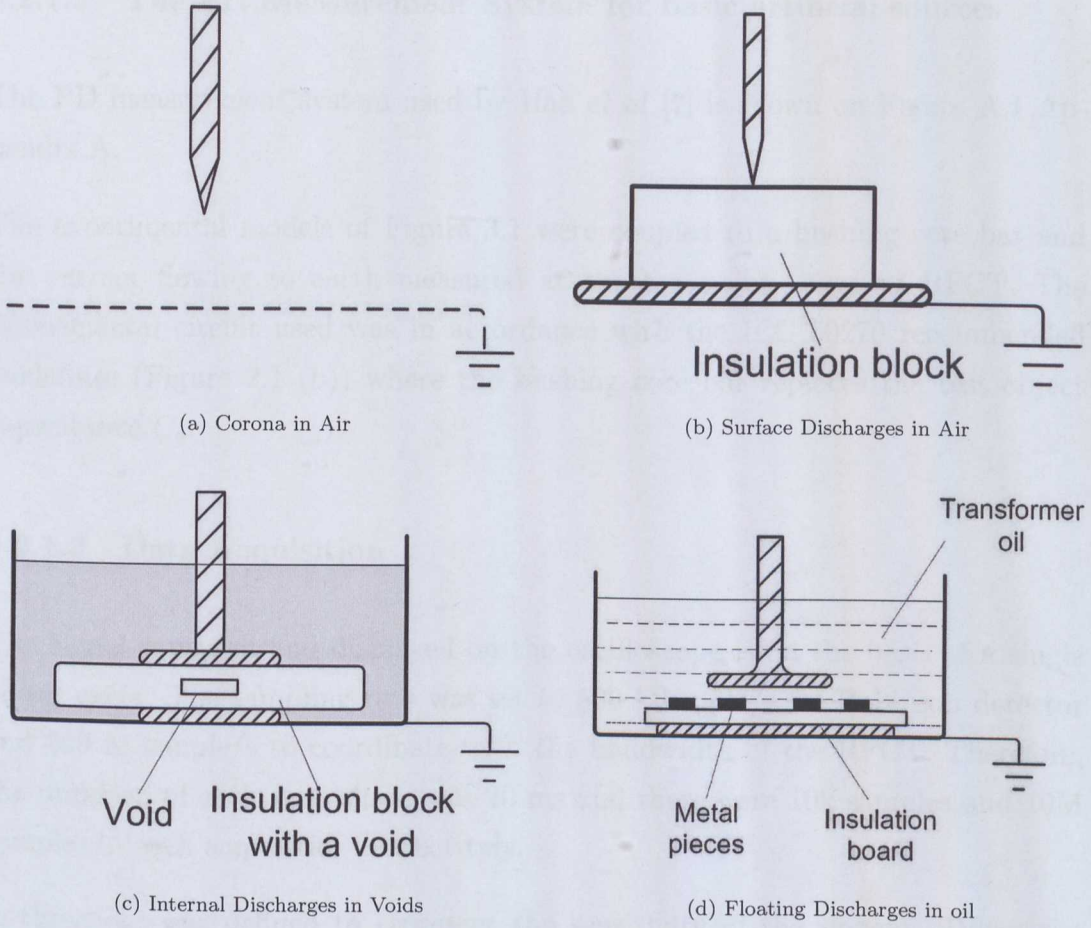

(a) Corona in Air

(b) Surface Discharges in Air

(c) Internal Discharges in Voids

(d) Floating Discharges in oil

FIGURE 3.1: Artificial PD sources [7]

A model used to generate discharges internally within a void is shown in Figure 3.1(c). The void (5 mm(diameter) 1 mm(depth)) was embedded between two pieces of perspex, which were placed between two symmetric planar electrodes.

A model was used to generate a floating discharges in an oil void in Figure 3.1(d). This consisted of two plane electrodes with a 5 mm gap left between the upper electrode and some separated metal pieces laid on an insulation board, the whole arrangement being immersed in transformer oil.

In both Figure 3.1(c) and (d), the HV source was connected to the upper electrode and the lower electrode earthed.

3.2.1.2 The PD Measurement System for basic artificial sources

The PD measurement system used by Hao *et al* [7] is shown on Figure A.1 Appendix A.

The experimental models of Figure 3.1 were coupled to a bushing core bar and the current flowing to earth measured at the tap point using an RFCT. The experimental circuit used was in accordance with the IEC 60270 recommended guidelines (Figure 2.1 (b)) where the bushing core bar replaces the test object capacitance C_a.

3.2.1.3 Data Acquisition

The signal captured and displayed on the oscilloscope is on the basis of a single power cycle. The sampling rate was set to 500 kSample/s for Robinson detector and 500 MSample/s to coordinate with the bandwidth of the RFCT. Therefore, the duration of each acquisition was 20 ms and there were 10k samples and 10M samples in each acquisition respectively.

A threshold was defined to represent the sensitivity of the system. When the amplitude of the obtained signal was above the threshold, a hold-off time was set to extract the expected PD pulse. The peak amplitude and its phase occurrence were therefore recorded. The peak amplitude in voltage (V) can be calibrated in terms of apparent charge (pC). The three dimensional ($\varphi - q - n$) PD signal (Section 2.6, Chapter 2) can then generated [7].

3.2.2 PD activity in oil impregnated paper systems

Experiments have been reported by Ariastina *et al* [90] to investigate the characteristics of partial discharges in a cavity with both new and aged oil impregnated pressboard-paper samples. Two different measurement systems, which provide four different measurement bandwidths were used to observe whether they would produce similar characteristics of discharges.

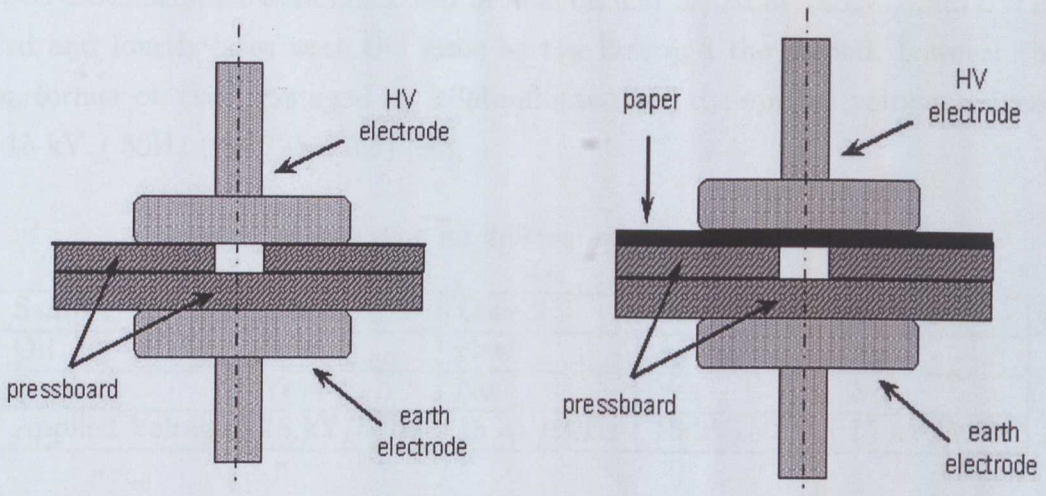

(a) With No extra insulation paper

(b) With extra insulation paper

FIGURE 3.2: Embedded air cavity in pressboard paper [4]

3.2.2.1 Samples and Electrodes Configuration - uniform field

Two 3 mm thick pressboard pieces, one with a hole to simulate a cavity, were sandwiched and used as the test sample [90]. Two different configurations were used in this experiment. Plane high voltage and earth electrodes with diameter of 40 mm were used to produce a uniform electric field. The high voltage electrode was placed on the top sample and covered the hole. Figure 3.2 shows the basic diagram of the samples and electrode configurations used in the experiment.

The first configuration was modeling trapped gas bubbles in a cavity bounded by the electrode and by the dielectric walls Figure 3.2(a).

The other configuration was for modeling a cavity bounded by two different kinds of insulation. In order to examine this effect, four pieces of crepe paper each with 0.3 mm thickness were inserted and pressed between the pressboard and the high voltage electrode. The size of the papers was similar to that of the pressboards Figure 3.2(b).

The samples and electrodes were mounted in a cylindrical glass cell filled with transformer oil. Testing was conducted at room temperature [90].

Four cases have been investigated during this experiment. The first case used a sandwiched pressboards and the second used the pressboards and the inserted

paper. Both samples were immersed in *new* oil and tested at 18 kV / 50Hz. The third and fourth cases were the same as the first and the second, however the transformer oil used was *aged* i.e. contaminated and the applied voltage reduced to 15 kV / 50Hz (see Table 3.2) [90].

TABLE 3.2: Notation for different sample configurations

Sample	Case 1	Case 2	Case 3	Case 4
Oil	New	New	Aged	Aged
Paper	Yes	No	Yes	No
Applied Voltage	18 kV/50Hz	18 kV/50Hz	15 kV/50Hz	15 kV/50Hz

3.2.2.2 The PD Measurement System for oil impregnated paper

Figure A.2 in Appendix A shows the PD measurement circuit used to generate the processed PD signals from the oil impregnated paper test of Ariastina *et al* [4]. The circuit for PD measurement and calibration procedure followed the IEC 60270 Standard [1], similar to Figure 2.1 (a), with a noise blocking filter Z_n incorporate in the Computerised Discharge Analyser (CDA3)

The PD pulses generated during the experiments were recorded using the (CDA3) system. This system displayed the integrated discharge quantities, such as discharge current, quadratic rate, discharge power and the repetition rate of the PD pulses. It also provided PD patterns for each half cycle of voltage and their various statistical distributions.

The capacitance of the test sample is denoted by C_s (Figure A.2). C_b represents a discharge free coupling capacitor. The analog output signal of the conventional PD detector is connected to the input of the CDA3 circuit board, which then performs further processes digitally.

Before testing, the measurement system was calibrated using an external calibration source. The parameter setup of the CDA3 system was also calibrated. This included the integration time, the detector calibration, the analyser calibration and the signal threshold.

To prevent interference from switching devices, the signal threshold of the CDA3 was set to 10 pC during measurements. Therefore any background noise lower than that specified value was rejected [91].

3.3 PD activity leading to breakdown

3.3.1 PD activity in oil impregnated paper systems

Ariastina *et al* in [91] investigated the effect of the voltage frequency variation in accelerating the deterioration of HV insulation. The experiments were also aimed at a detailed investigation of the effect of oil contamination on the partial discharge activity and its effect on deterioration of the insulation material. The same experimental circuit was used as in Figure A.2 in Appendix A.

3.3.1.1 Samples and Electrodes Configuration - non uniform field

Two 3 mm-thick pressboard pieces were sandwiched and used as the test sample. The pressboards had a square shape and dimensions of 50 mm x 50 mm. The upper sample has a circular hole with diameter of 7.9 mm, located centrally (Figure 3.3).

The HV electrode was a sphere of 11.5 mm diameter. It was a bare electrode made of brass. The HV electrode was placed on the hole of the upper sample., Hence both the electrode and sample form a cavity, bounded by the HV electrode (Figure 3.3). Because of this configuration, the electric field applied to the samples was nonuniform.

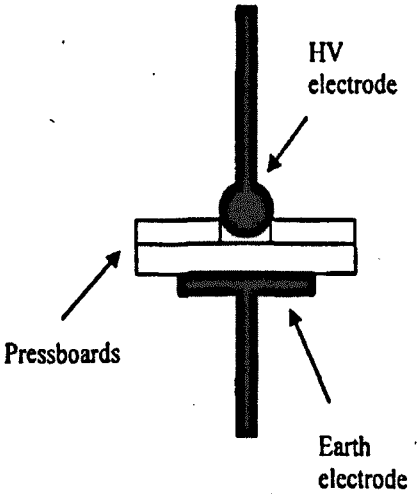

FIGURE 3.3: Sample configuration [4].

The samples were mounted in a cylindrical glass cell for testing at room temperature. Three cases have been investigated during this experiment. The first test

used dry less contaminated transformer oil , which had moisture levels of less than 20 ppm. For the second test, medium contaminated transformer oil with 20-30 ppm moisture was used. The oil with moisture more than 100 ppm was applied for the third test, which represented highly contaminated oil.

The test voltage level was varied from 3 to 7 kV during the experiment and the partial discharge activity initiated in the test sample was recorded [4]. To achieve higher frequency test voltage, a variable voltage frequency converter was utilised to drive a high frequency test transformer.

3.3.2 PD in *artificial* point plane geometry

Lai *et al* in [8] aimed at investigating the characteristics of PDs due to electrical treeing before the insulation breakdown. Several point to plane electrode specimens were prepared using epoxy resin as the insulation material, and tested under different voltage levels from 10kV to 12kV AC. While PD data acquisitions were in progress by means of a precision computer-based measuring system. The trends of the phase resolved patterns prior to breakdown and far before breakdown were compared.

3.3.2.1 Samples Configuration - non uniform field

For the experiment setup, a point to plane electrode configuration was implemented (Figure 3.4). The test specimens were manufactured by casting a needle with curvature radius of 1.2 μm into a block of epoxy resin as insulation. A thin conductive silver paint layer was used as the plane electrode, which was connected to the ground. The spacing between the needle tip and plane electrode was 2 mm. The needle was connected to a high voltage (HV) and the test sample was submerged in transformer oil to prevent corona and surface discharges.

3.3.2.2 Measurement circuit

The PD measurement test system used by lai et al [8] was set up according to IEC60270 standard is shown on Figure A.3 Appendix A. PD data was regularly recorded at a specific voltage level throughout the lifespan of the epoxy resin insulation.

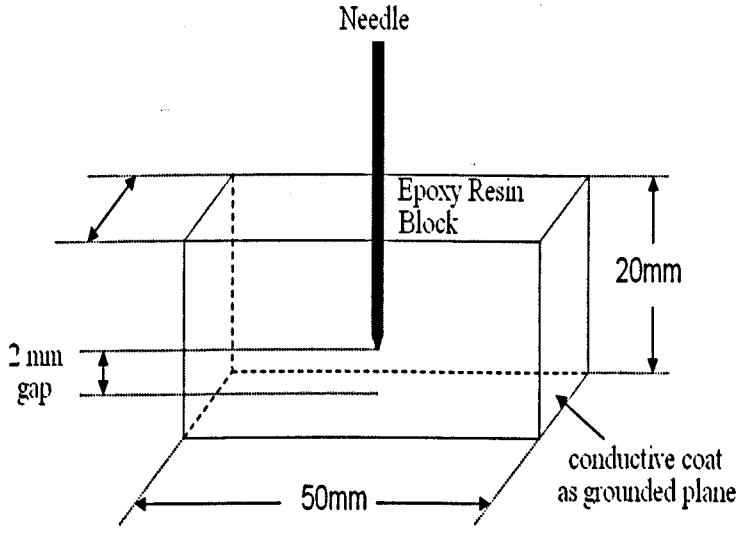

FIGURE 3.4: Sample configuration [8].

Three samples had been tested at applied voltage of 10kV, 11kV and 12kV respectively. Test voltage of 10kV was applied on the first sample and the total time from the initial PD monitoring until breakdown was about 87 minutes. The second sample was tested at 11kV and the time from start to breakdown was around 190 minutes (3 hours). The third sample was tested at 12kV and the time from start to breakdown was around 353 minutes (6 hours).

3.3.3 PD in *real* point plane geometry

Cavallini *et al* in [22] and [92] investigated PD inference for the early detection of Electrical Treeing.

The approach required the acquisition of a large set of discharge pulses, in order to be able to separate different PD sources in homogeneous clusters and reject noise contributions. Such a goal was achieved through a fuzzy clustering algorithm that operated on the basis of time-frequency parameters extracted from the acquired pulses in order to summarise their shape. Then, statistical processing was applied to PD derived quantities relevant to homogeneous data set, such as PD height, phase and time-of-occurrence distributions.

These quantities constituted input parameters for the identification algorithm, which consisted of a fuzzy engine. This processing-identification system was able to associate PD events to internal defects, surface and corona discharges [22].

The method used to infer electrical trees in electrical insulation systems is presented in [22].

3.3.3.1 Samples Configuration - non uniform field

The rules used for the construction of a fuzzy engine able to single out the presence of electrical trees were extracted from several experiments undertaken on artificial test objects, as well as cable joints with artificial defects and HV transformers.

The artificial test objects were realised by inserting a needle in a press-moulded cross-linked polyethylene (XLPE) slab, then retracting the needle by 1 mm, in order to form a cavity in front of the needle tip as in Figure 3.5. PD measurements were carried out at step-increasing voltage; each voltage step lasted from 1 to 2 h [22] and [92]

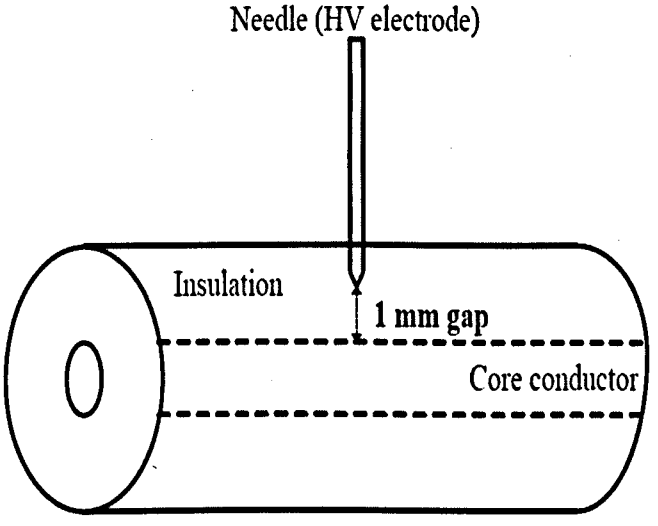

FIGURE 3.5: Sample configuration, HV used cable slab

3.3.3.2 Measurement circuit

The PD measuring circuit used was based on diagnostic routines operating on a personal computer. The interface between these routines and the investigated electric system consisted of an ultra wide-band (UWB) digitiser. A 50 Ω resistor suitable for radio frequency applications was used as a measuring impedance (i.e.,to convert current pulses to voltage pulses compatible with the digitiser TTL input). The signal was preprocessed by an analog high-pass filter to suppress the

low frequency components associated to supply voltage. Operator protection was obtained by connecting a digitiser and PC through a fiber optic cable. A schematic description of the system is shown in Figure A.4 Appendix A. The PD measurement and diagnosis used was based on a digitiser which stored the whole shape of the recorded PD pulses [9]

3.4 2D representation of PD activity from different sources

Data have been available from various sources [4] [7] [8] [22] for PD activity from the different investigators described in Section 3.2 above. These results are presented graphically where the vertical axis represents the PD amplitudes in Volts and the horizontal axis their corresponding phase angles. Particular attention is paid to the following features : the PD signal amplitudes, the phase angle for the onset of PD activity and phase angle duration of the PD activity. These features are considered for both positive and negative half cycles of the voltage oscillation and the results are summarised on Table 3.3.

TABLE 3.3: PD activity from various sources

		Positive Half Cycle				Negative Half Cycle			
PD source	Voltage (kV)	Max PD (V-pC)	Onset Phase	Phase Duration	Number of PDs	Max PD (V-pC)	Onset Phase	Phase Duration	Number of PDs
Internal	21	3.25 V	40^o	100^o	5178	3.5	220^o	100^o	5103
	24	4.5 V	30^o	100^o	7526	4.5	210^o	100^o	7435
Surface	6	2.4 V	0^o	130^o	39186	0.58	170^o	140^o	39338
	9	2.54 V	-10^o	140^o	23416	0.45	175^o	135^o	33560
Floating	23	1.94 V	-40^o	145^o	1866	1.94	-150^o	140^o	2110
	25	2.08 V	-40^o	145^o	1844	2.08	-150^o	140^o	2181
Corona	6.9	2.98 V	0^o	60^o	4658	2.98	180^o	180^o	45553
	8	3.00 V	0^o	180^o	101178	3.00	180^o	180^o	63759
	10	3.04 V	0^o	180^o	216200	3.04	180^o	180^o	209559
New oil	18	129 pC	-30^o	115^o	1071	213	-30^o	115^o	1578
Aged oil	15	161 pC	18^o	65^o	871	208	18^o	62^o	978
New oil + paper	18	113 pC	-20^o	100^o	365	120	-20^o	100^o	781
Aged oil + paper	15	125 pC	10^o	63^o	465	208	10^o	75^o	699

3.4.1 Internal PD source

Figure 3.6 (a) and (b) show results for PD activity from an internal source during both positive and negative half cycles of a 50 Hz voltage oscillation. They were plotted from the raw data provided by Hao *et al.* The X-axis represents the electrical phase angles in degrees, while the Y-axis represents the PD ampliudes recorded in volts, not in pC (as given by Hao *et al*).

Figure 3.6 (a) and (b) are from an alternating voltages of peak values of 21 kV and 24 kV respectively. A threshold of 0.36 V was set before any PD activity was recorded. Most of the PD activity during both half cycles with both voltages cover a phase angle range of 100°; (40° to 140°) during the positive half cycle and (220° to 320°) during the negative half cycle.

The PD activity becomes more peaked and higher in amplitude as the applied voltage increased. The increase of PD amplitudes, when the applied voltage had been increased, was accompanied by an increase of the number of PD events, from 10281 at 21 kV to 14961 at 24 kV. This is apparent in the difference of concentration of points from Figure 3.6 (a) and (b).

The PD events appear to be more or less evenly spread between the two half cycles; at 21 kV, (5178 PD event in the positive half cycle and 5103 in the negative half cycle), and at 24 kV, (7526 PD events during the positive half cycle, and 7435 PD events during the negative half cycle).

Also, the PD activity started occurring after the first 30° phase angle of the 1^{st} half cycle and after 210° (i.e. 180° + 30°) of the 2^{nd} cycle. At 21 kV, the PD activity reached a maximum level of 3.25 V in the positive half cycle and 3.5 V in the negative half cycle. At 24 kV, the PD activity reached a maximum level around 4.5 V in both half cycles. Little PD activity occurred outside the two stated phase angle ranges.

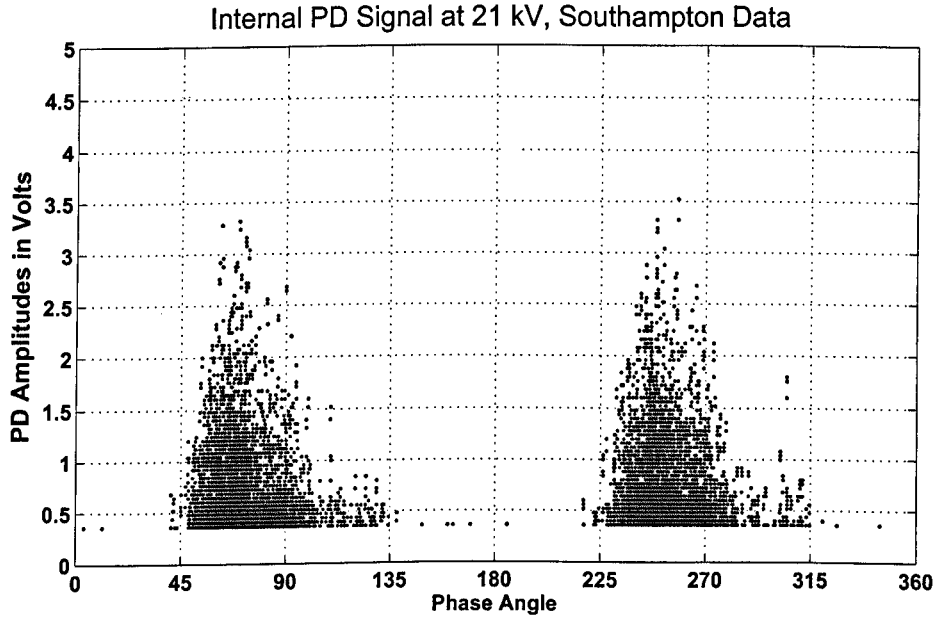

(a)

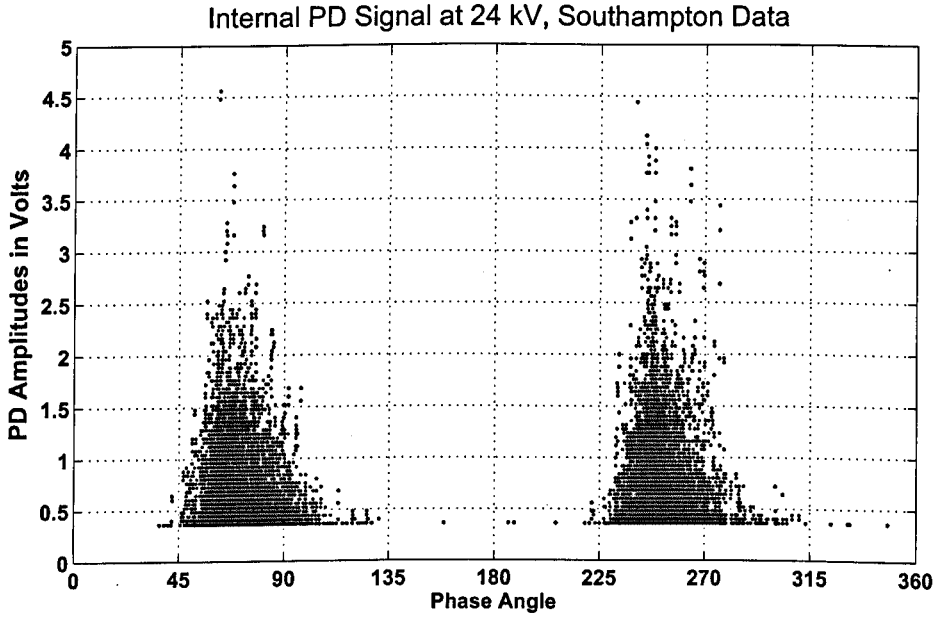

(b)

FIGURE 3.6: 500 x 20 ms accumulated Partial Discharge activity recorded from an Internal PD source at (a) 21 kV and (b) 24 kV.

3.4.2 Surface PD source

The surface PD tests were conducted with applied voltages of 6kV to 9kV . A PD threshold signal was set to 0.12 V, so that any PD activity below this threshold was counted as noise and therefore not recorded. The results are presented in Figure 3.7 (a) and (b). For both applied voltages, the highest amplitudes of PD activity occurred during the positive half cycle and reached 2.4 V for the 6kV applied voltage and 2.54 V for 9 kV. During the negative half cycle, at both voltages, the PD activity amplitudes didn't exceed 0.6 V; 0.58 V at 6kV and 0.45 V at 9 kV.

As the applied voltage increases, the spread of the PD activity seems to become narrower, especially during the negative half cycle, and slightly higher in amplitude, during the positive half cycle.

When the applied voltage increased, the number of PD events decreased, numerically, from 78421 PD events at 6 kV to 56976 PD events at 9 kV. The PD events were more or less evenly spread between the two half cycles at 6 kV, there were 39186 PD event in the positive half cycle and 39338 in the negative half cycle. At 9 kV, the difference was greater, 23416 PD events were recorded during the positive half cycle, and 33560 PD events were recorded during the negative half cycle.

The PD activity commenced before 0^o phase angle in both half cycles. During the negative half cycle, it commenced at about -10^o. Regions devoid of PD activity lay between 130^o and 170^o during the positive half cycle and between 310^o and 350^o during the negative half cycle, where the PD amplitudes were limited between 0.12 and 0.14 V.

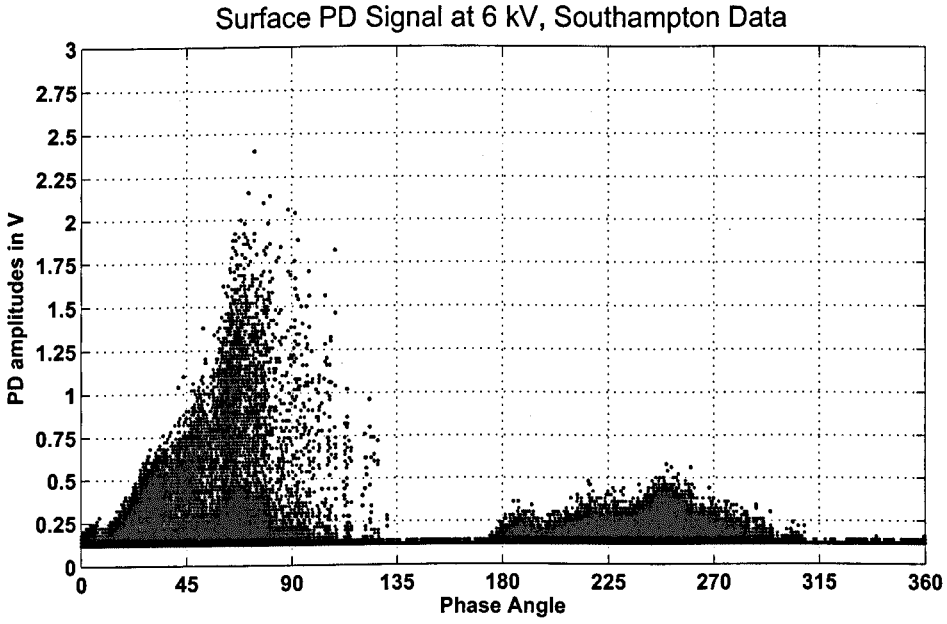

(a)

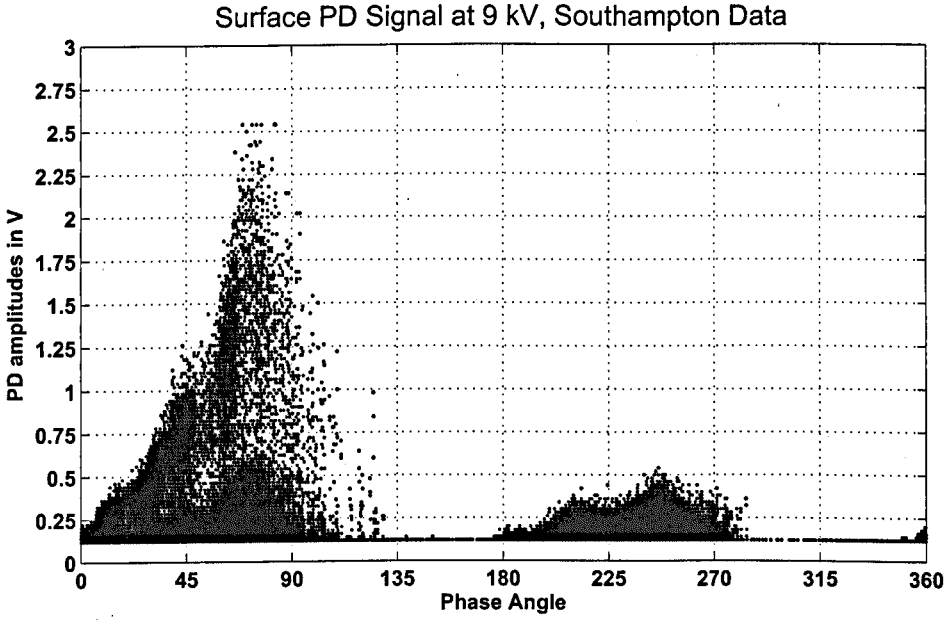

(b)

FIGURE 3.7: 500 x 20 ms accumulated Partial Discharge activity recorded from a Surface in air PD source at (a) 6 kV and (b) 9 kV.

3.4.3 Floating in oil PD source

The level of applied voltage used to generate PD activity for the floating in oil PD tests, was between 23kV-25kV. The results are shown in Figure 3.8 (a) and (b). A PD threshold signal was set to 0.12 V. At both applied voltages, the highest amplitudes of PD activity, which occurred during both half cycles, was around 2 V (1.94 V - 2.08 V). The PD activity seems to be evenly spread and more scattered above 0.75 V PD level.

The increase in the applied voltage did not have a large effect on the number of PD events. At 23 kV and 25 kV the number of PD events are 3976 and 4025 respectively. The distribution of the PD events between the two half cycles at both applied voltages was similar; the number of PD events during positive half cycle was 1866 at 23 kV and 1844 at 25 kV. The number of PD events during the negative half cycle was 2110 at 23 kV and 2181 at 25 kV.

The PD activity occurred before the 0^o phase angle in both half cycles. This commenced at -40^o during the 1^{st} half cycle and at -30^o (150^o-180^o) during the 2^{nd} half cycle. PD activity outside the active regions along the phase angle axis, between 105^o and 145^o during the positive half cycle and between 280^o and 320^o during the negative half cycle, was limited to 0.12 V, with the exception of some PD events which occurred at 25 kV around 297^o phase angle.

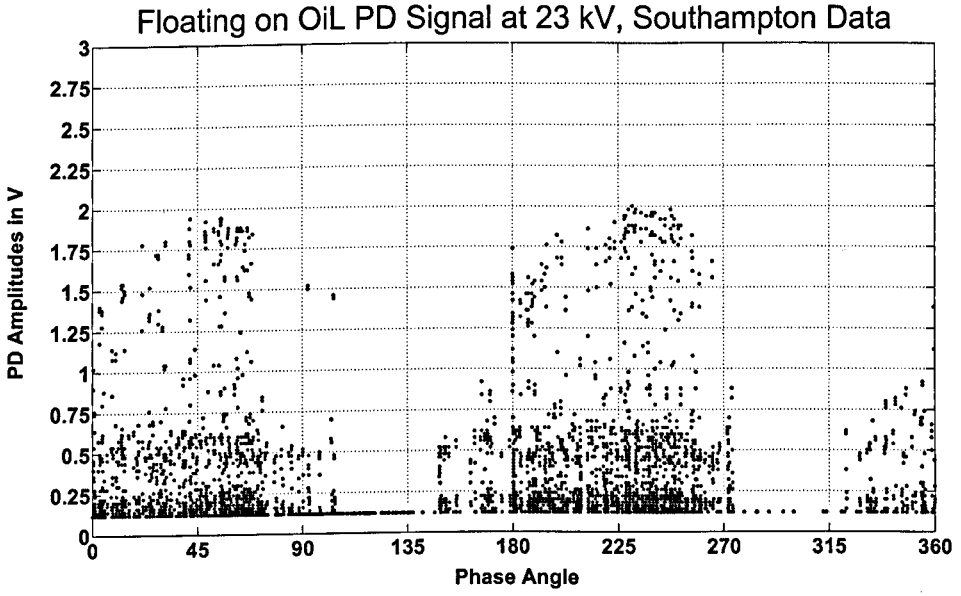

(a)

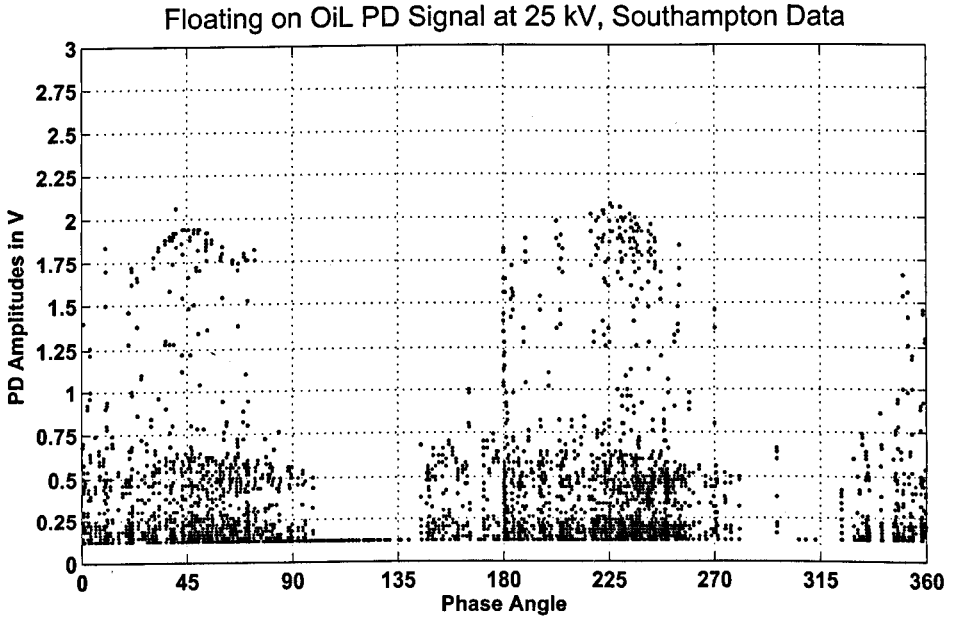

(b)

FIGURE 3.8: 500 x 20 ms accumulated Partial Discharge activity recorded from a Floating in oil PD source at (a) 23 kV and (b) 25 kV.

3.4.4 Corona in air PD source

Figure 3.9 (a),(b) and (c) shows the PD activity produced by a corona in air. The level of applied voltage was between 6.9kV and 10kV. A PD threshold signal was set to 0.4 V, so that any PD activity below this threshold was regarded as noise and therefore not recorded.

At all applied voltages, 6.9kV, 8kV and 10 kV, the highest amplitudes of PD activity, occurring during both half cycles, was around 3 V (2.98 V - 3.04 V). At 6.9 kV, a phase region with no PD activity is observed between the phase angles 30^o and 150^o. The increase of the applied voltage had a substantial effect on the number of PD events. The number of PD events at 6.9 kV, 8 kV and 10 kV were 50211, 164937 and 425759 respectively. This is noticeable in the difference in the concentration points between Figure 3.9 (a), (b) and (c).

A clear no PD activity gap is apparent in Figure 3.9(a), between 30^o and 150^o, a less PD activity concentration region in Figure 3.9(b) between 180^o and 270^o. Whereas in Figure 3.9(c), the PD activity occupied the whole power cycle. The distribution of the PD events between the two half cycles varies with the applied voltages. At 6.9 kV, the number of PD events during positive and negative half cycles were 4658 and 45553 (an order of 10 times magnitude increase). At 8 kV, the distribution was reversed; the number of PD events during positive and negative half cycles were 101178 and 63759 respectively. At 10 kV, the distribution was even; the number of PD events during positive and negative half cycles being 216200 and 209559.

The PD activity commenced at 0^o phase angle in both half cycles. At 6.9 kV, PD activity outside the active region along the phase angle axis, between 30^o and 150^o during the positive half cycle, was limited to 0.4 V.

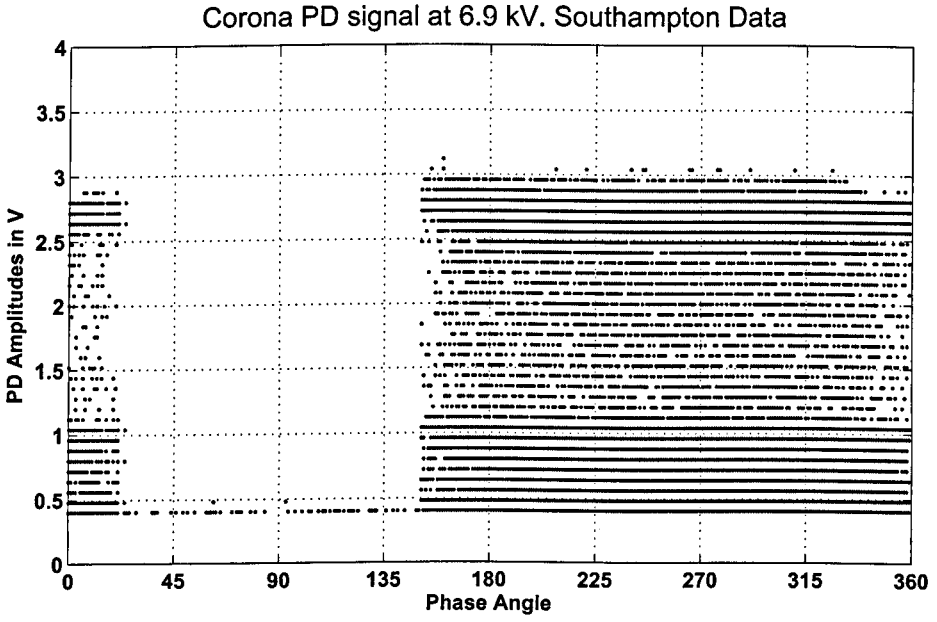
Corona PD signal at 6.9 kV. Southampton Data
PD Amplitudes in V
Phase Angle
0
0.5
1
1.5
2
2.5
3
3.5
4
0
45
90
135
180
225
270
315
360

(a)

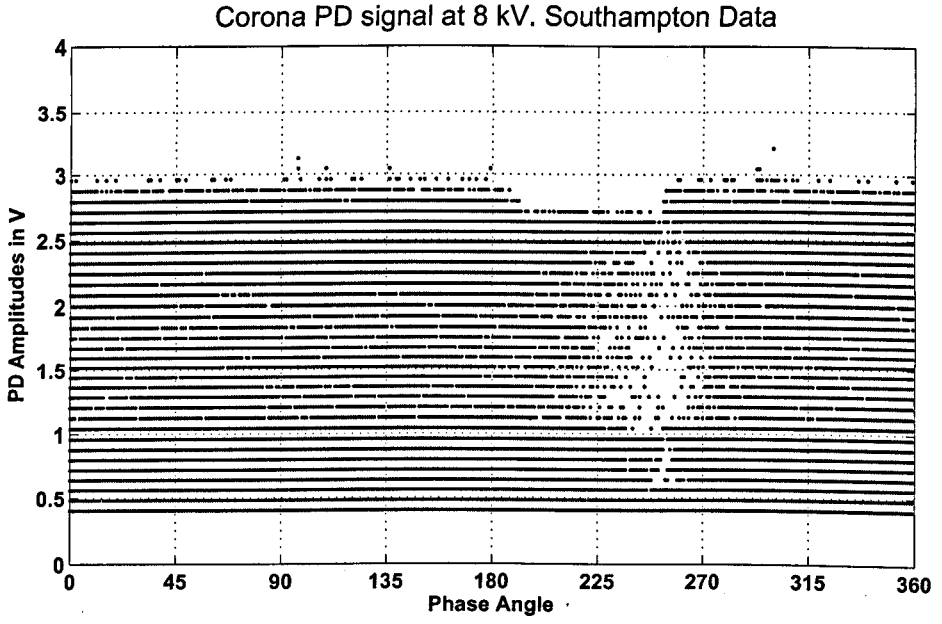
Corona PD signal at 8 kV. Southampton Data
PD Amplitudes in V
Phase Angle
0
0.5
1
1.5
2
2.5
3
3.5
4
0
45
90
135
180
225
270
315
360

(b)

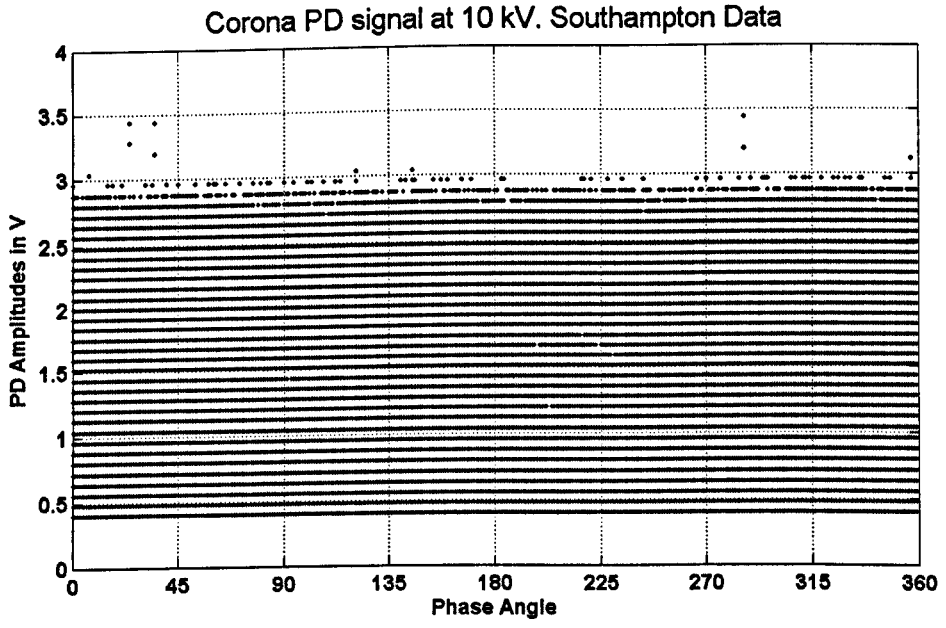

(c)

FIGURE 3.9: 500 x 20 ms accumulated Partial Discharge activity recorded from a Corona PD source at (a) 6.9 kV, (b) 8 kV and (c) 10 kV.

3.4.5 PD activity in New and Aged Oil

The PD producing arrangement used for the oil samples described in 3.2.2.1 was used to assess the effect of a layer of insulation paper between the air cavity and the upper electrode (Figure 3.2), at two different voltages (15 and 18 kV) and with two different oil qualities (new and aged). The results were summarised in Table 3.2.

Figure 3.10 (a) and (b) show the PD activity for a new oil at a voltage of 18 kV and for an aged oil at a voltage of 15 kV respectively, without the insulation paper between upper electrode and the air gap cavity.

At 18 kV and with no extra paper insulation (Figure 3.10(a)), during the positive half cycle, the PD activity extended over a range of phase angles of -30^o to 85^o, reaching a maximum of 129 pC and there were 1071 PD activity events recorded. During the negative half cycle, the PD activity extended from 150^o to 265^o, reached a maximum value of 213 pC and there were 1578 PD events recorded.

At 15 kV and with no extra paper insulation between the air cavity gap and the upper electrode (Figure 3.10(b)), during the positive half cycle, the PD activity occurred between 18^o and 83^o reached a maximum of 161 pC and there were 870 PD activity events recorded. During the negative half cycle, PD activity occurred between 198^o to 260^o, reached a maximum value of 208 pC and there were 987 PD events recorded.

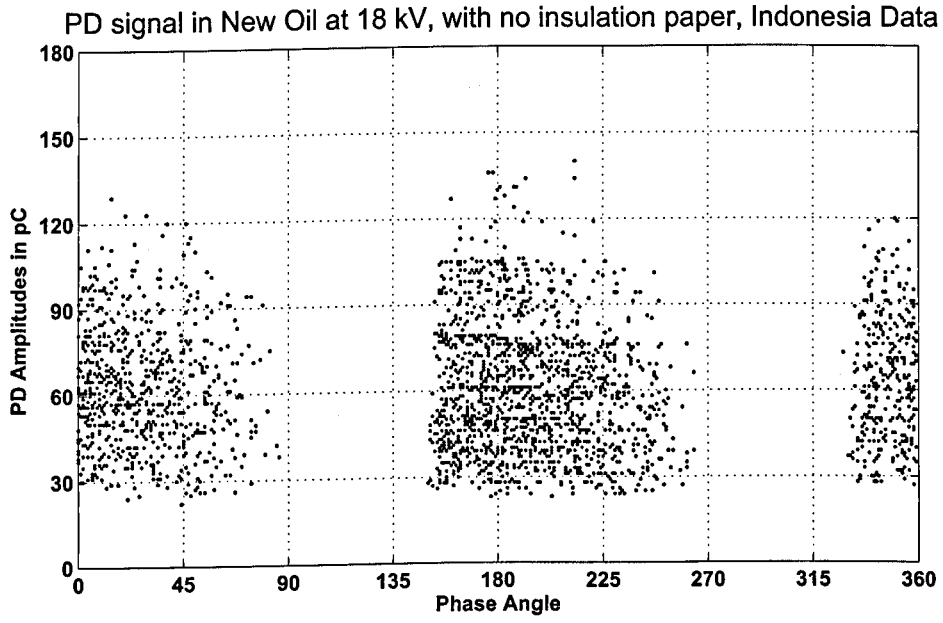

(a)

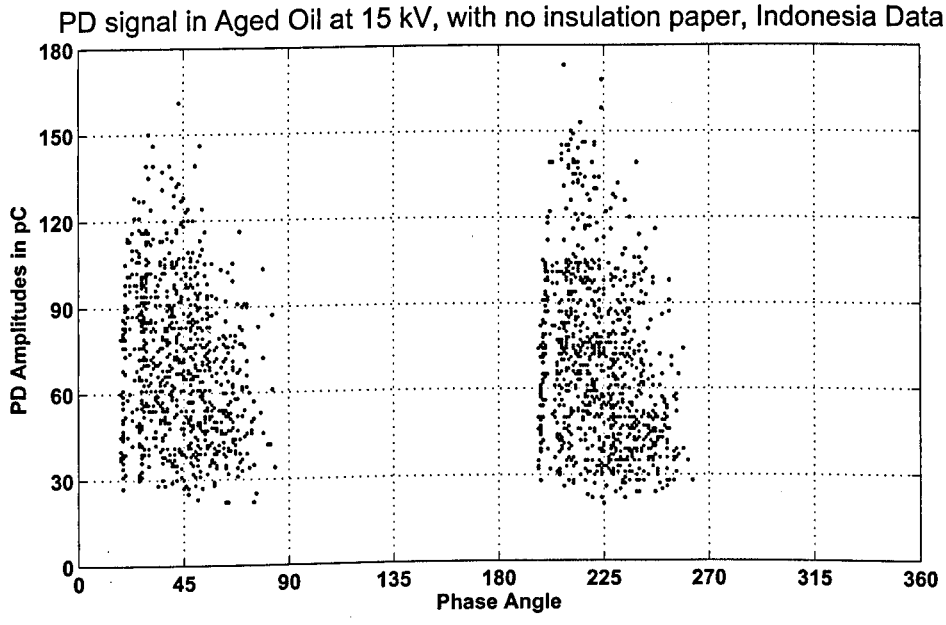

(b)

FIGURE 3.10: Accumulated Partial Discharge activity recorded without extra insulation paper in: (a) New oil PD sources at 18 kV. (b) Aged oil PD source at 15 kV.

3.4.6 PD activity New and Aged Oil plus insulation paper

Figure 3.11 (a) and (b) show the PD activity for a new oil at a voltage of 18 kV and for an aged oil at a voltage of 15 kV respectively, with the extra insulation paper.

At 18 kV and with the paper insulation, Figure 3.11(a), during the positive half cycle, the PD activity extended over a phase range of -20^o to 80^o, reaching a maximum of 113 pC and there were 365 PD activity events recorded. During the negative half cycle, the PD activity extended from around 160^o to 260^o, reaching a maximum value of 120 pC and there were 781 PD events recorded.

At 15 kV and with extra paper insulation between the air cavity gap and the upper electrode, Figure 3.11(b), during the positive half cycle, PD activity occurred between 10^o and 73^o, reached a maximum of 125 pC and there were 465 PD activity events recorded. During the negative half cycle, PD activity occurred between 190^o to 265^o, reached a maximum value of 208 pC and there were 699 PD events recorded.

With new oil and no paper insulation, at 18 kV , the PD activity first occurred at -30^o phase angle for both half cycles (Figure 3.10(a)), but occurred at -20^o when extra insulation paper was added Figure 3.11(a), i.e. the PD activity occurred again 10^o earlier with the extra paper added.

With aged oil and no paper insulation , at 15 kV, (Figure 3.10(b)) the PD activity commenced at 18^o phase angle for both half cycles, (198^o in 2^{nd} half cycle is 180^o + 18^o) but occurred at 10^o when the extra insulation paper was added, i.e. the PD activity occurred 10^o earlier with the extra paper.

With the new oil samples at 18 kV, Figure 3.11(a) the number of PD events decreased from 2649 to 1146 PD event when extra insulation paper was introduced. Also, at 15 kV with the aged oil,Figure 3.11(b) the number of event decreased from 1857 to 1155 PD event after adding extra insulation paper.

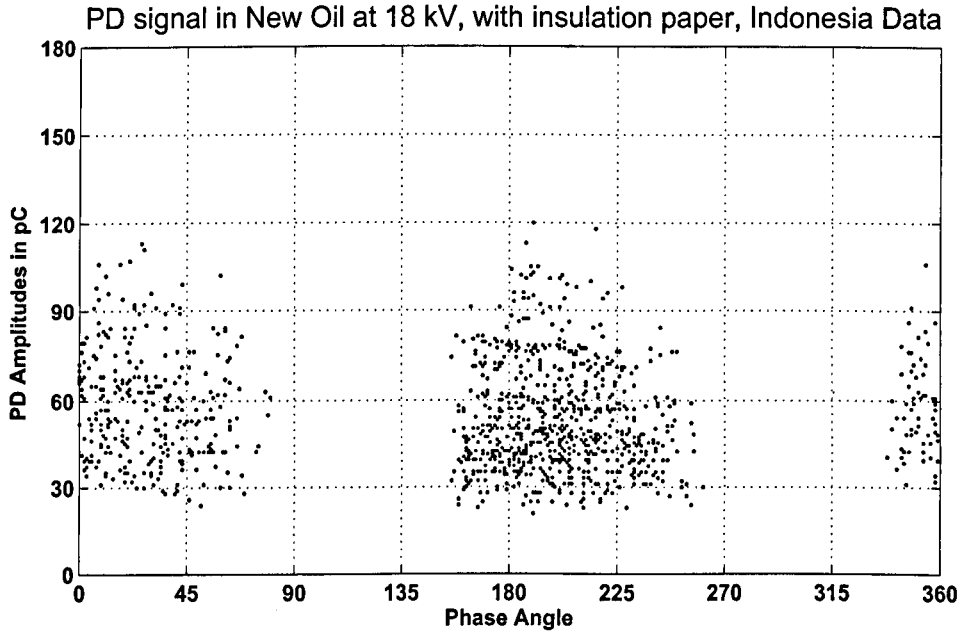

(a)

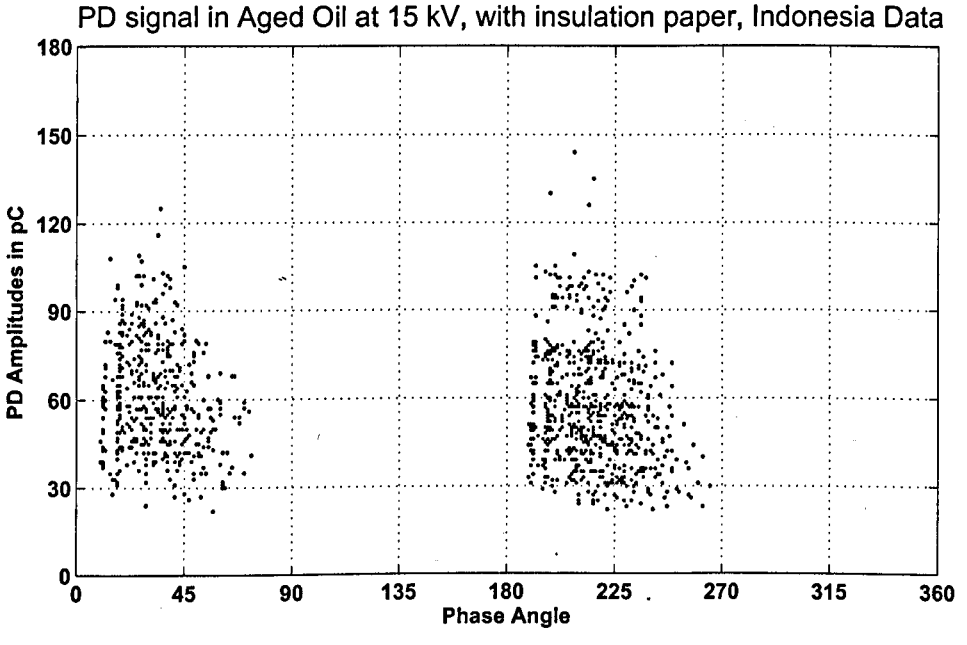

(b)

FIGURE 3.11: Accumulated Partial Discharge activity recorded with extra insulation paper in: (a) New oil PD sources at 18 kV. (b) Aged oil PD source at 15 kV.

3.5 2D representation of PD activity at various voltages and progression to full breakdown

3.5.1 Variation of PD activity with time

The second data set consisted of 3 phase resolved analysis (PRA) graphs of a needle-plane epoxy resin PD source (Section 3.3.2), taken at different stages towards breakdown, Lai *et al* [8].

3 PD signals were generated under laboratory conditions from the same PD source and the same applied voltage of 11 kV. As the raw data was not made available by Lai *et al*, the graphs were digitised from their publication [8] following the procedure described in Appendix D. The resulted data was then chromatically processed.

Figure 3.12 (a),(b) and (c) show the results for different times before full breakdown with the vertical axis representing the PD amplitudes in *pico* Coulombs (pC) and the horizontal axis their corresponding phase angles for both positive and negative cycles. Depending on the sensitivity of the PD detector used, a threshold of 7 pC was set before any PD activity was recorded. The vertical scales of Figure 3.12 (a) and (b) are up to 60 pC, for Figure 3.12 (c) it is up to 1400 pC. The results derived from these graphs are summarised on Table 3.4.

TABLE 3.4: PD activity parameters during approach to full breakdown (applied voltage 11 kV) for needle-plane epoxy resin

Time before breakdown	31 minutes		18 minutes		Just before breakdown	
Half cycle	1^{st}	2^{nd}	1^{st}	2^{nd}	1^{st}	2^{nd}
Phase angle duration	110^o	120^o	130^o	130^o	90^o	90^o
Onset phase angle	4^o	0^o	-10^o	-10^o	0^o	0^o
Max PD (pC)	39	37	53	55	1116	1266

Figure 3.12(a) shows the PD activity recorded 31 minutes before the insulation was compromised. During the positive half cycle, PD activity occurred at phase angles from about 4^o to 114^o and reached a maximum of 39 pC. During the negative half cycle, PD activity occurred from 180^o to 300^o and reached a maximum value of 37 pC.

Figure 3.12(b) shows the PD activity recorded 18 minutes before breakdown. During the positive half cycle, PD activity extended from -10^o to 120^o and reached a maximum of 53 pC. During the negative half cycle, PD activity extended from about 170^o to 300^o and reached a maximum value of 55 pC.

Figure 3.12(c) shows the PD activity recorded just before breakdown. It shows a background PD activity of 67 pC extending across the whole phase angle range from 0^o to 360^o. Superimposed upon this background are bursts of PD activity reaching a level of 1116 pC in the phase angle range 30^o and 120^o during the first half cycle and 1266 pC in the phase angle range 210^o and 300^o during the second half cycle.

The results of Figure 3.12(a),(b) and (c) taken together show that the phase angle at which PD activity commence changed from 4^o (31 minutes), via -10^o (18 min) to filling the whole phase angle range just before breakdown.

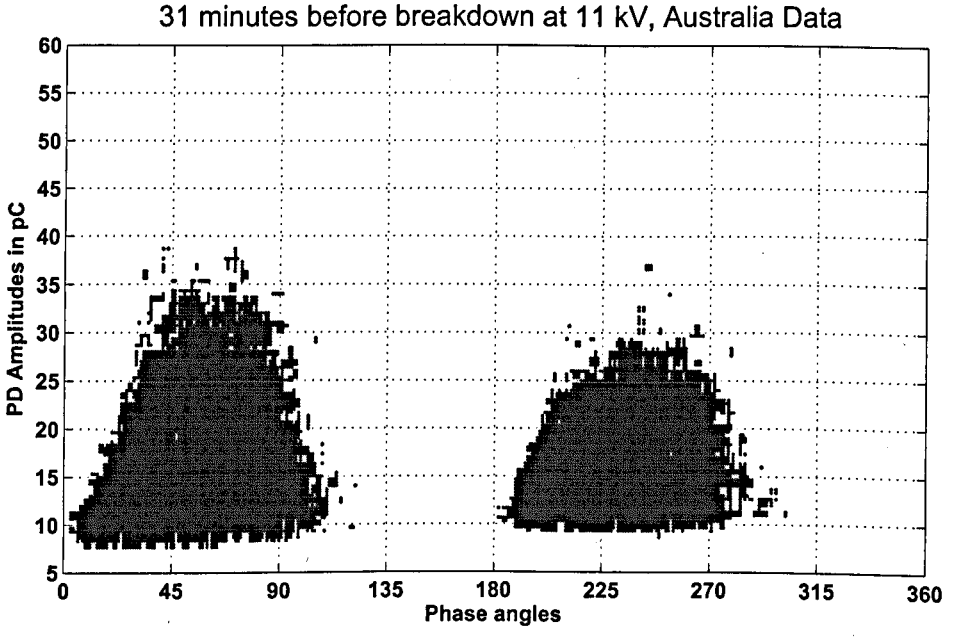

(a)

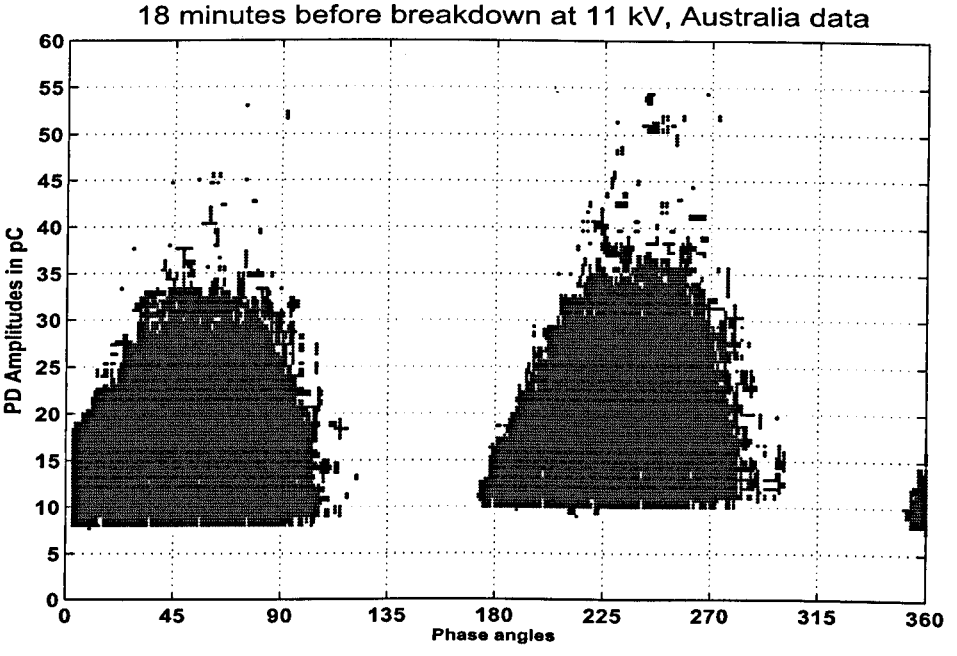

(b)

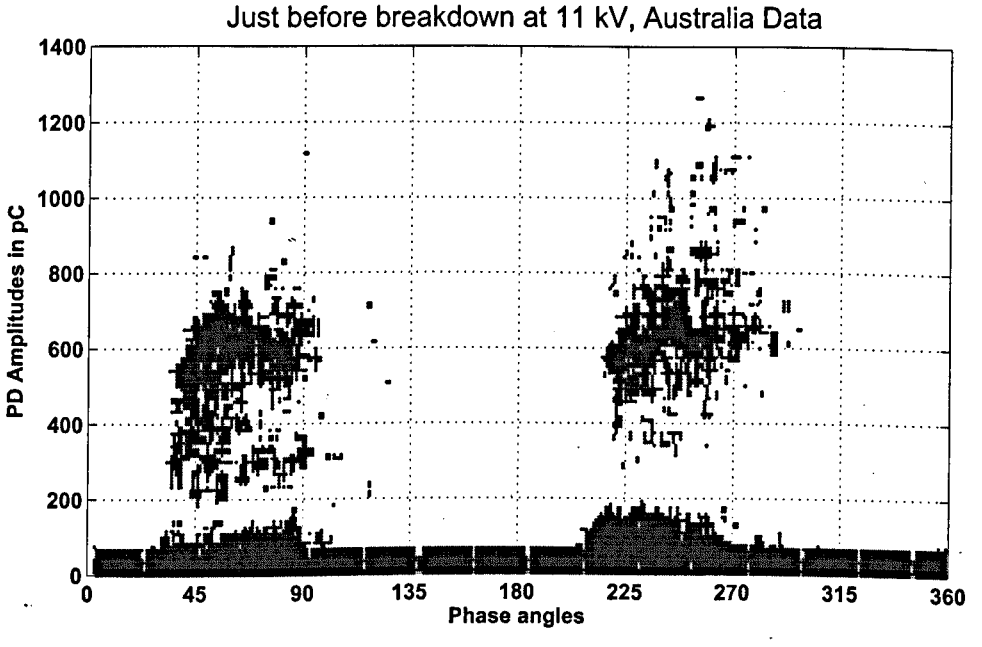

(c)

FIGURE 3.12: Accumulated Partial Discharge activity recorded in a needle-plane epoxy resin PD source at 11 kV applied voltage. (a) At 31 minutes before breakdown. (b) At 18 minutes before breakdown. (c) Just before breakdown.

3.5.2 PD activity in different oils at various voltages

The third data set was provided by Ariastina *et al* [4] from Udayana University in Indonesia. It consisted of 2 sets of PD signals generated under laboratory conditions from 2 different PD source configurations (Section 3.3.1)

In the following graphs, the vertical axis represents the PD amplitudes in *pico* Coulombs (pC) and the horizontal axis their corresponding phase angles. Both positive and negative cycles are shown sequentially on each diagram. A threshold of 10 pC was set before any PD activity was recorded.

3.5.2.1 PD activity in moderately contaminated oil at various voltages

Figure 3.13(a) to (e) show the PD activity results in moderately contaminated oil at different applied alternating voltages of peak values 3,4,5,6 and 7 kV respectively. The phase angle duration, phase onset, maximum pC values and number of PD events for each half cycle of the voltage waveform are summarised on Table 3.5.

TABLE 3.5: PD activity parameters for each half cycle from various applied voltages with moderately contaminated oil

Applied voltage (kV)	3		4		5		6		7	
Half cycle	1^{st}	2^{nd}	1^{st}	2^{nd}	1^{st}	2^{nd}	1^{st}	2^{nd}	1^{st}	2^{nd}
Phase angle duration	70^o	50^o	100^o	100^o	112^o	112^o	119^o	120^o	125^o	127^o
Onset phase angle	30^o	40^o	15^o	15^o	8^o	8^o	1^o	0^o	-1^o	-1^o
Max PD (pC)	274	354	640	418	782	689	916	903	1027	1074

Figure 3.13(a) represents PD activity at 3 kV. During the positive half cycle, PD activity spans from 30^o to 100^o, it reached a maximum of 274 pC and there were 607 PD activity events recorded. During the negative half cycle, PD activity spans from 220^o to 270^o, it reached a maximum value of 141 pC and there were 354 PD events recorded.

Figure 3.13(b) represents PD activity at 4 kV. During the positive half cycle, PD activity spans from 15^o to 115^o, it reached a maximum of 640 pC and there were

1448 PD activity events recorded. During the negative half cycle, PD activity spans from 195^o to 295^o, it reached a maximum value of 418 pC and there were 1704 PD events recorded.

Figure 3.13(c) represents PD activity at 5 kV. During the positive half cycle, PD activity spans from 8^o to 120^o, it reached a maximum of 782 pC and there were 2592 PD activity events recorded. During the negative half cycle, PD activity spans from 188^o to 300^o, it reached a maximum value of 689 pC and there were 2845 PD events recorded.

Figure 3.13(d) represents PD activity at 6 kV. During the positive half cycle, PD activity spans from 1^o to 120^o, it reached a maximum of 916 pC and there were 3847 PD activity events recorded. During the negative half cycle, PD activity spans from 180^o to 300^o, it reached a maximum value of 903 pC and there were 4195 PD events recorded.

Figure 3.13(e) represents PD activity at 7 kV. During the positive half cycle, PD activity spans from -1^o to 126^o, it reached a maximum of 1027 pC and there were 5027 PD activity events recorded. During the negative half cycle, PD activity spans from 179^o to 306^o, it reached a maximum value of 1074 pC and there were 5363 PD events recorded.

As the applied voltage was increased, the phase extent of the PD activity became wider at lower voltages and narrower at higher voltages. The increase of PD amplitudes, when the applied voltage had increased, was accompanied by an increase of the number of PD events, numerically, from 961 PD events at 3 kV to 10390 PD events at 7 kV, and can be noticed from the difference of points' density between graphs Figure.5.5 (a) to (e). The PD events at positive half cycle were always lower than those in the negative half cycle, except in the 3 kV sample.

The PD activity commenced after a phase angle of 30^o for the 1^{st} half cycle and 210^o (180^o + 30^o) for the 2^{nd} half cycles. The onset phase angle decreased, with increasing the applied voltage, until it reached -1^o at 7 kV. PD activity reached a maximum level of 274 pC at 3 kV and 1074 pC at 7 kV.

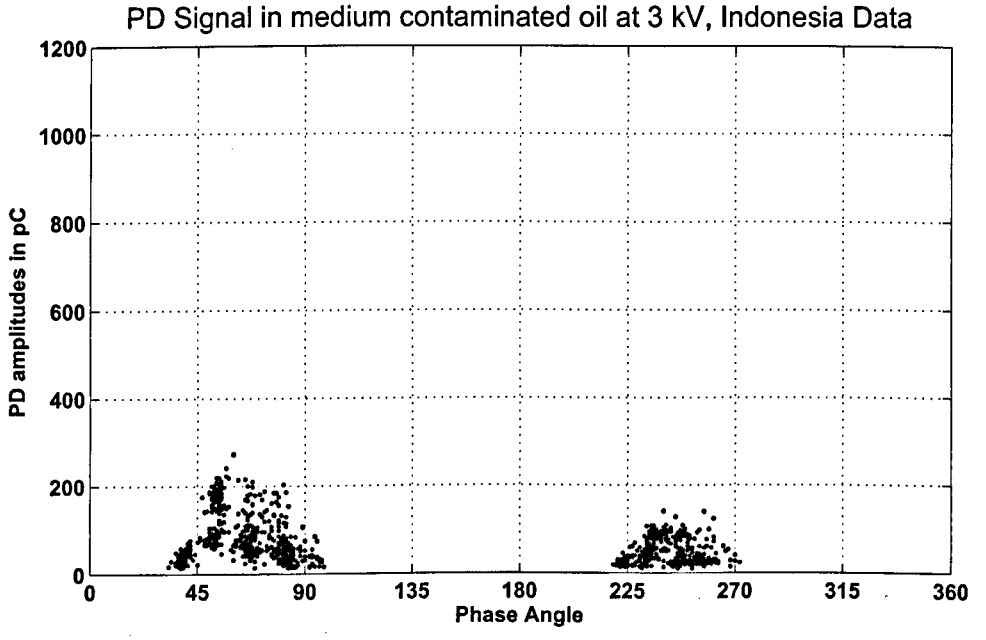
PD Signal in medium contaminated oil at 3 kV, Indonesia Data
PD amplitudes in pC
Phase Angle
0
200
400
600
800
1000
1200
0
45
90
135
180
225
270
315
360

(a)

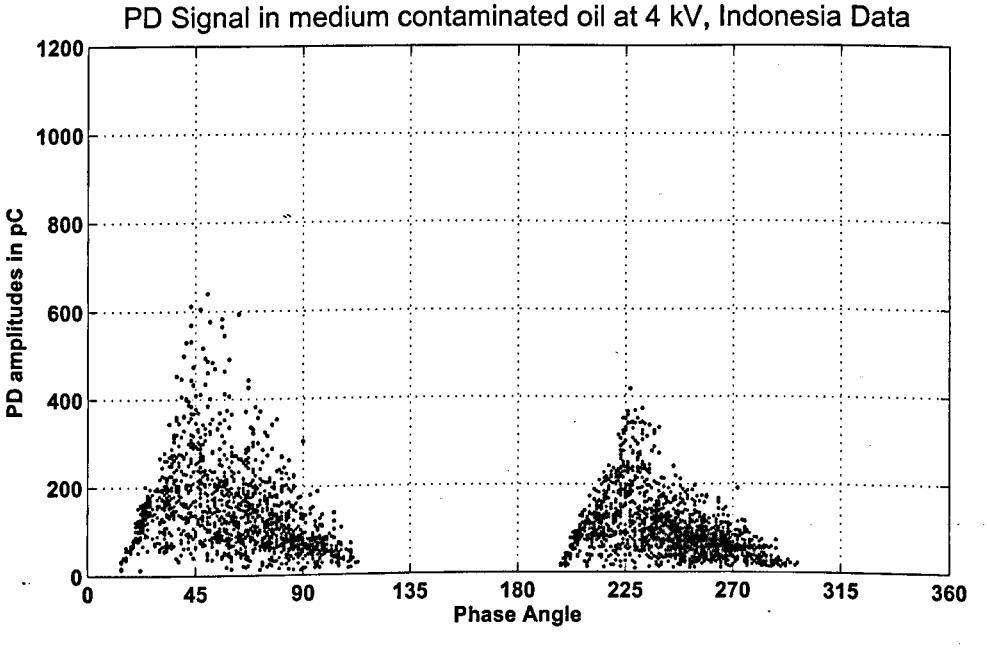
PD Signal in medium contaminated oil at 4 kV, Indonesia Data
PD amplitudes in pC
Phase Angle
0
200
400
600
800
1000
1200
0
45
90
135
180
225
270
315
360

(b)

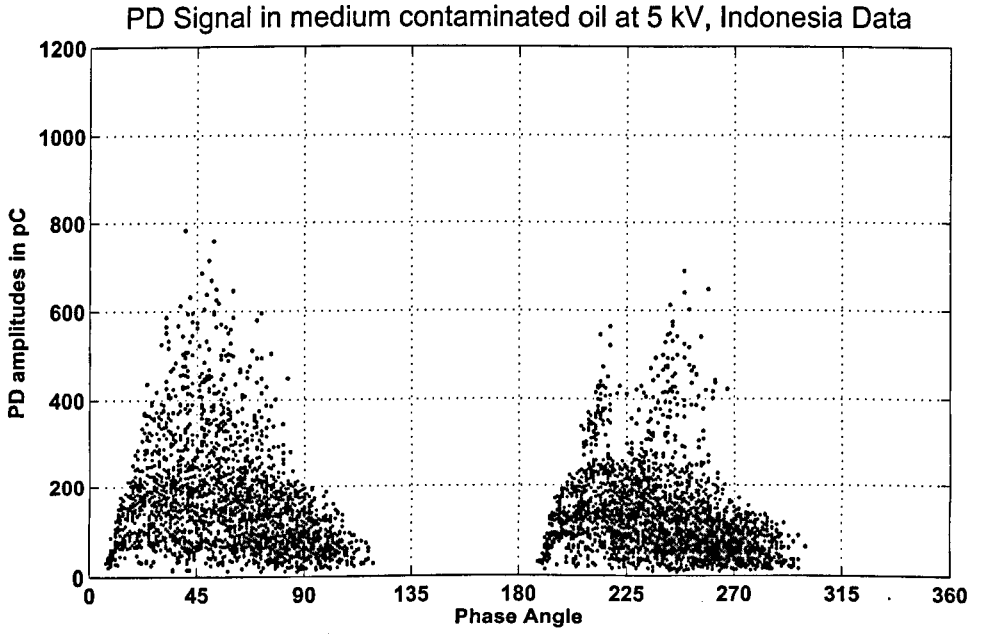
PD Signal in medium contaminated oil at 5 kV, Indonesia Data
PD amplitudes in pC
Phase Angle
0
200
400
600
800
1000
1200
0
45
90
135
180
225
270
315
360

(c)

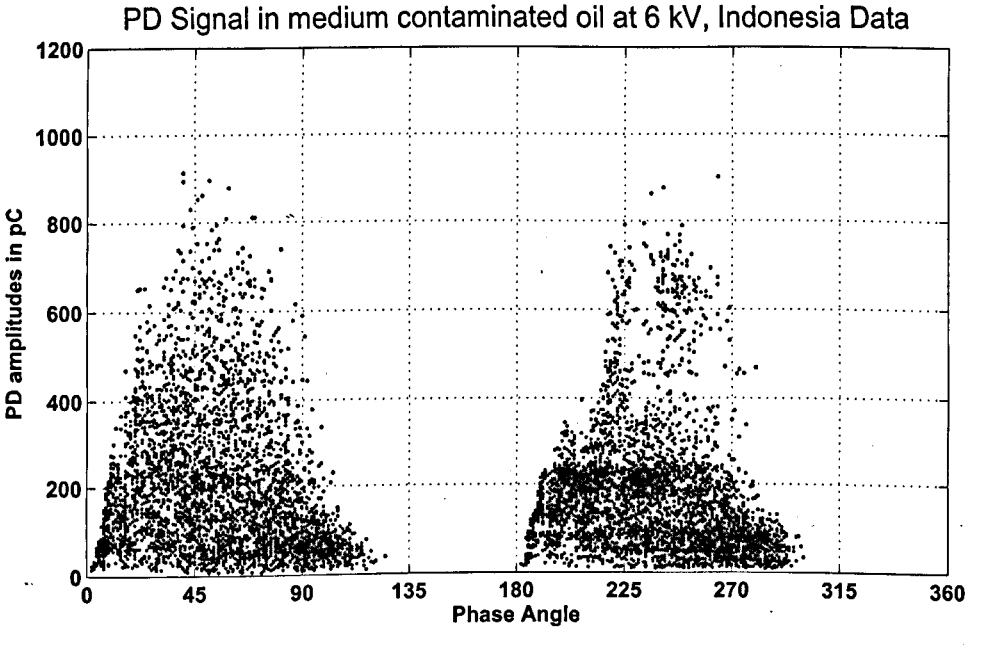
PD Signal in medium contaminated oil at 6 kV, Indonesia Data
PD amplitudes in pC
Phase Angle
0
200
400
600
800
1000
1200
0
45
90
135
180
225
270
315
360

(d)

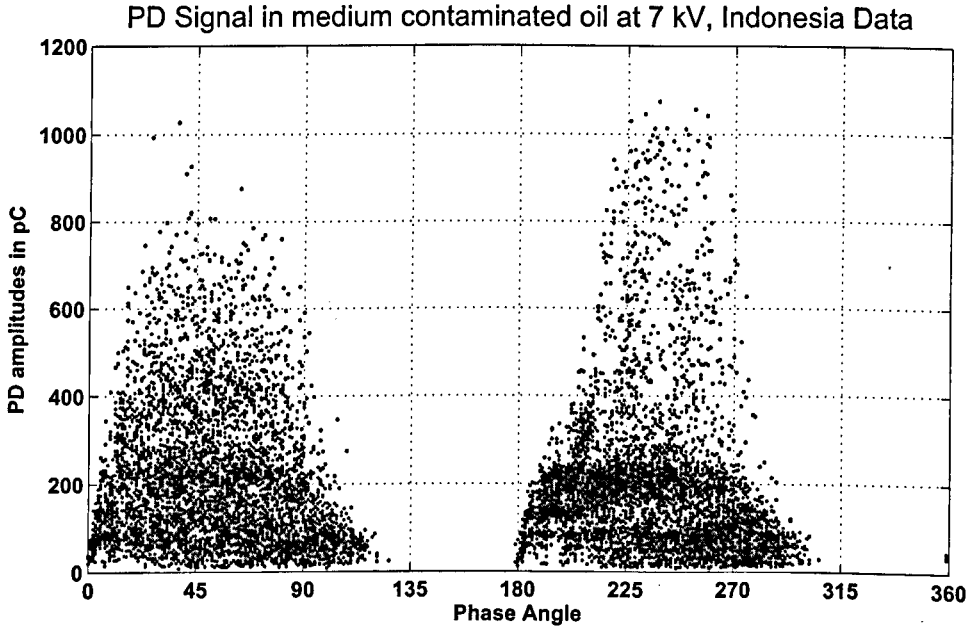

(e)

FIGURE 3.13: Accumulated Partial Discharge activity recorded in a medium contaminated oil PD source at different applied voltages; 3kV, 4kV, 5kV, 6kV and 7kV respectively (a, b, c, d, e).

3.5.2.2 PD activity in Highly contaminated oil at various voltages

Figure 3.14 (a),(b) and (c) represent results for the pC coulombs versus phase angles for highly contaminated oil at applied voltages of 3,5 and 5 kV respectively. The results are summarised on Table 3.6 in terms of the phase angle duration of PD, onset phase angle, maximum pC and number of PDs during each half cycle.

TABLE 3.6: PD activity parameters for each half cycle from various applied voltages with highly contaminated oil

Applied Voltage (kV)	3		4		5	
Half Cycle	1^{st}	2^{nd}	1^{st}	2^{nd}	1^{st}	2^{nd}
Phase angle Duration	70^o	70^o	100^o	95^o	110^o	110^o
Onset phase angle	30^o	25^o	15^o	15^o	10^o	15^o
Max PD (pC)	240	186	328	249	487	245

At an applied voltage of 3 kV (Figure 3.14(a)) during the positive half cycle, PD activity occurred between 30^o and 100^o, reached a maximum of 240 pC and there were 622 PD events recorded. During the negative half cycle, PD activity occurred between 205^o and 275^o, reached a maximum value of 186 pC and there were 791 PD events recorded.

At an applied voltage of 4 kV (Figure 3.14(b)) during the positive half cycle, PD activity extended from 15^o to 115^o, reached a maximum of 328 pC and there were 1524 PD events recorded. During the negative half cycle, the PD activity extended from 195^o to 290^o, reached a maximum value of 249 pC and there were 2001 PD events recorded.

At 5 kV (Figure 3.14(c)) during the positive half cycle, PD activity extended from 10^o to 120^o, reached a maximum value of 487 pC and there were 2520 PD events recorded. During the negative half cycle, PD activity extended from 185^o to 295^o, reached a maximum value of 245 pC and there were 3651 PD events recorded.

These results indicate that as the applied voltage increased, the PD activity extended over a wider range of phase angles at lower levels but narrower at higher amplitudes. This extention was accompanied by an increase of the number of PD events, from 1413 PD events at 3 kV to 6171 PD events at 5 kV. The PD events during the positive half cycle were always lower than those during the negative half cycle.

Also, the onset phase angle of the PD activity decreased with applied voltage for both half cycles, the change being from 30° to 10° during the first half cycle between 3 and 5 kV. PD activity reached a maximum level of 239 pC at 3 kV and 487 pC at 5 kV.

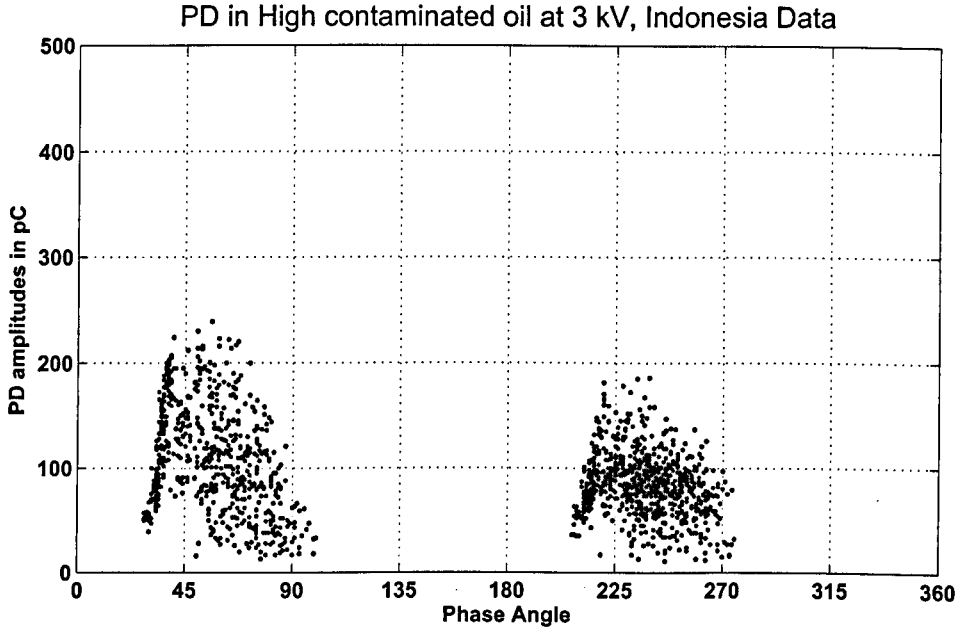

(a)

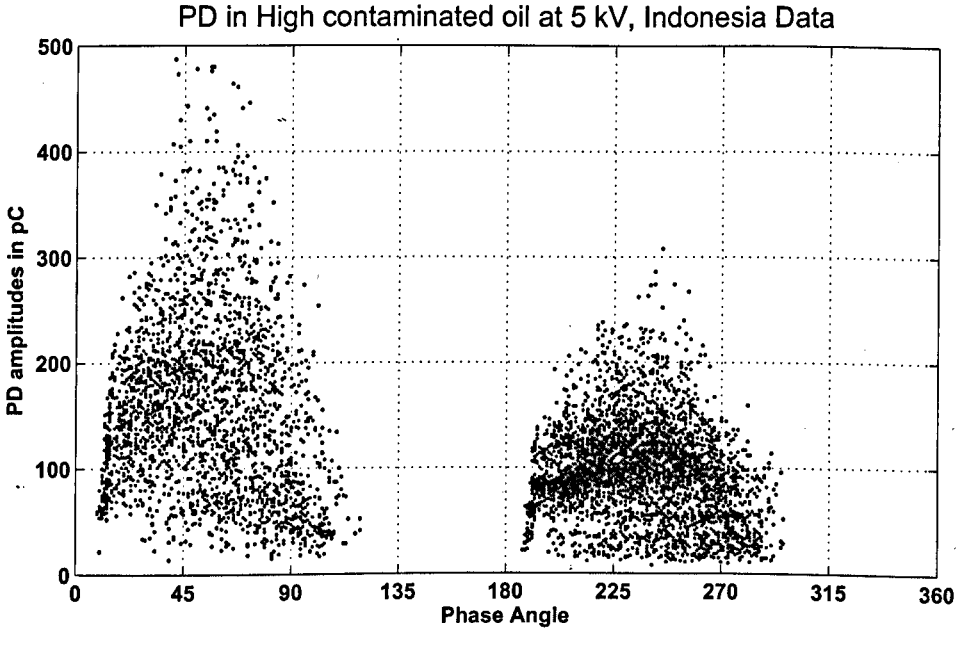

(b)

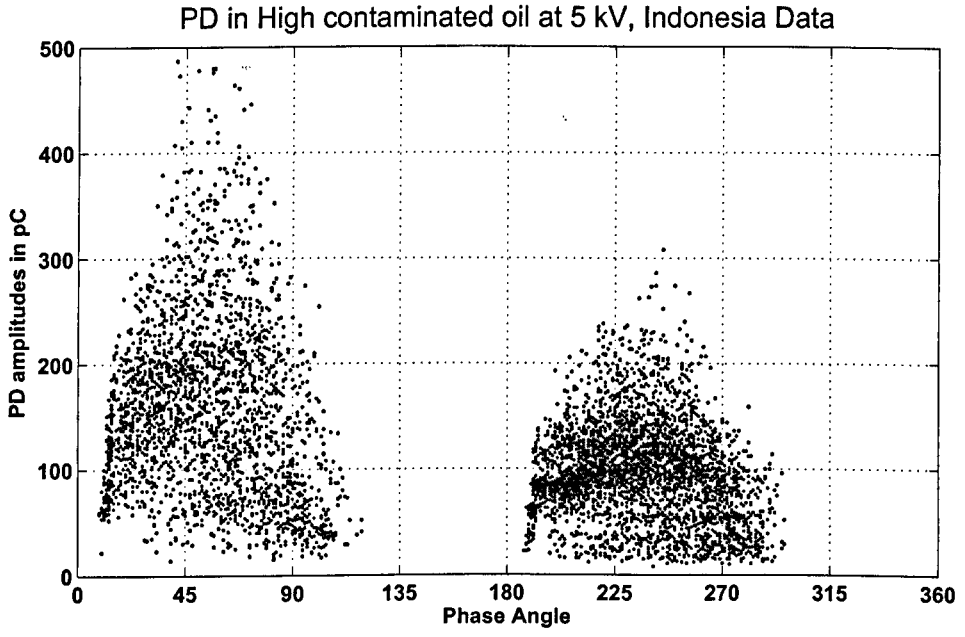

(c)

FIGURE 3.14: Accumulated Partial Discharge activity recorded in a high contaminated oil PD source at different applied voltages; 3kV, 4kV and 5kV respectively (a, b, c).

3.5.3 PD activity variation with time at various voltages

The fourth data set (Cavallini *et al* [22]) was 3 phase resolved analysis (PRA) graphs of a needle-plane geometry (Section 3.15) in a XLPE cable PD source, taken at different stages towards breakdown, under laboratory conditions from the same PD source. These results have been digitised from [22] (as the raw data was not made available by Cavallini *et al*).

The published diagrams were digitised following the procedure described in Appendix D to produce the graphs shown on Figure 3.15 (a), (b) and (c). The Y-axis represents the PD amplitudes in *pico* Coulombs (pC) while the X-axis depicts their corresponding phase angles, for both positive and negative half cycles. A threshold of 100 pC was set before any PD activity was recorded. The results derived from these graphs are summarised on Table 3.7 before and after tree inception and prior breakdown.

As the raw data was not made available by Lai *et al*, the graphs were digitised from their publication [8] following the procedure described in Appendix D. The

resulted data was then chromatically processed.

TABLE 3.7: PD activity parameters during approach to breakdown for needle-plane in XLPE cable

Applied voltage (kV)	7		7		8	
Half cycle	1^{st}	2^{nd}	1^{st}	2^{nd}	1^{st}	2^{nd}
Phase angle duration	115^o	115^o	135^o	130^o	145^o	130^o
Onset phase angle	-35^o	-35^o	-45^o	-55^o	-55^o	-50^o
Max PD (pC)	625	770	815	950	1566	950

Figure 3.15(a) shows the PD activity recorded before electrical tree inception in the insulation at 7 kV. During the positive half cycle, PD activity occurred from about -35^o to 80^o and reached a maximum of 625 pC. During the negative half cycle, PD activity occurred from 145^o to 260^o and reached a maximum value of 770 pC.

Figure 3.15(b) shows the PD activity recorded some time after electrical tree inception, at the same applied voltage of 7 kV. During the positive half cycle, PD activity occurred from -45^o to 90^o and reached a maximum of 815 pC. During the negative half cycle, PD activity extended from about 125^o to 255^o, it reached a maximum value of 950 pC.

Figure 3.15(c) represents PD activity recorded just before breakdown, after an increase of the applied voltage to 8 kV. During the positive half cycle, PD activity extended from -55^o to 90^o; it reached a maximum of 1566 pC. During the negative half cycle, PD activity occurred between 130^o and 260^o and reached a maximum value of 950 pC.

The results of Figure 3.15 (a),(b) and (c) taken collectively show that, before tree inception, the onset for the PD activity was -35^o phase angle during both first and second half cycles. After the tree inception, the onset phase angle during the 1^{st} half cycle decreased by 10^o (to reach -45^o) and the range of PD activity increased by 10^o , and during the 2^{nd} half cycle decreased by 20^o to reach 125^o. As breakdown was approached, the onset phase angle during the 1^{st} half cycle decreased further by 10^o to reach -55^o and during the 2^nd half cycle the whole PD activity phase angle range shifted forward by 5^o.

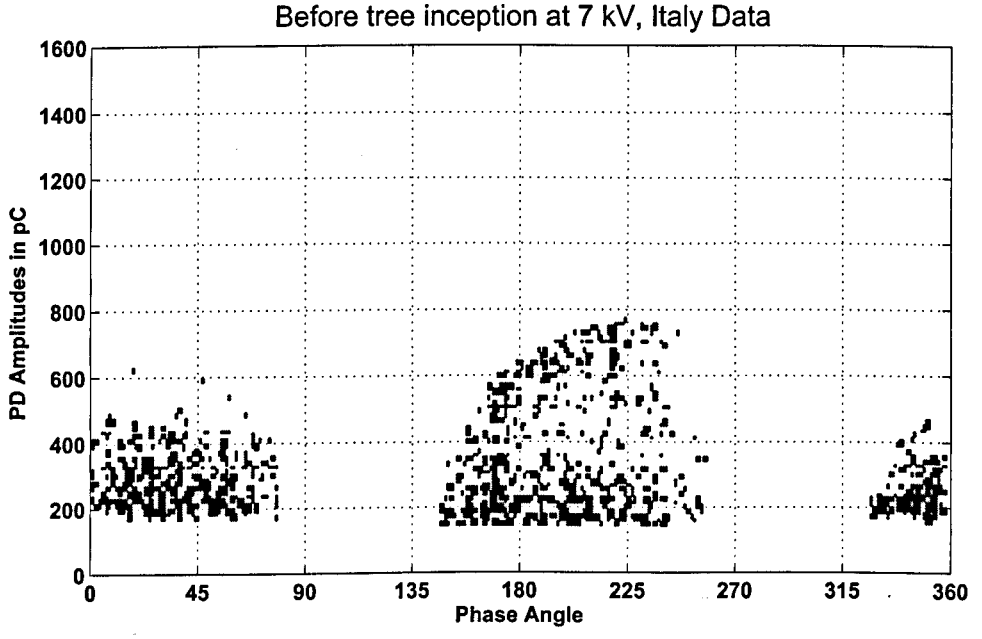
Before tree inception at 7 kV, Italy Data
PD Amplitudes in pC
Phase Angle
0
200
400
600
800
1000
1200
1400
1600
0
45
90
135
180
225
270
315
360

(a)

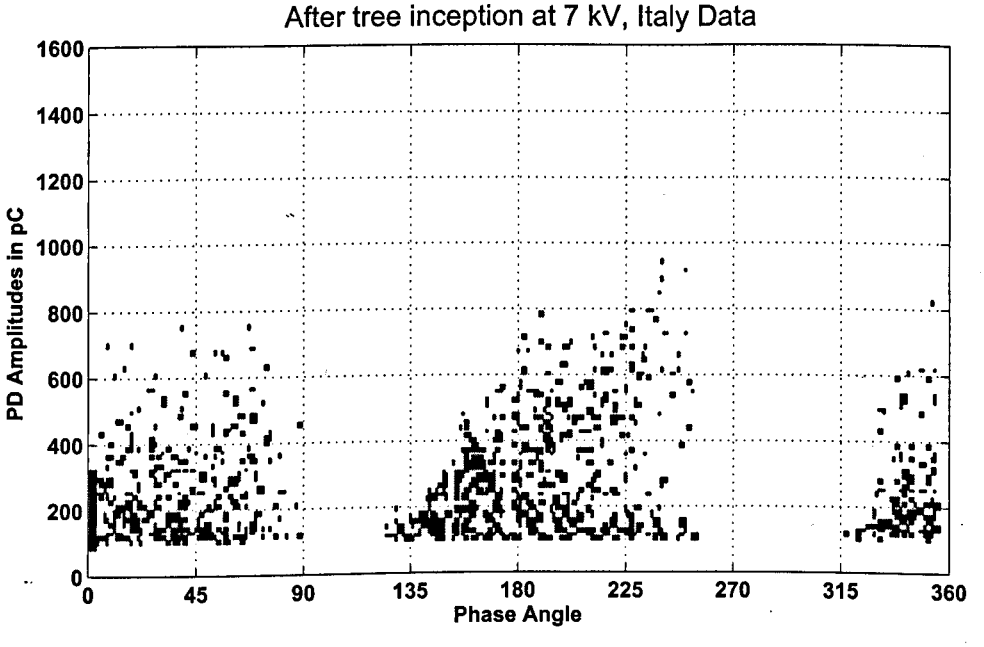
After tree inception at 7 kV, Italy Data
PD Amplitudes in pC
Phase Angle
0
200
400
600
800
1000
1200
1400
1600
0
45
90
135
180
225
270
315
360

(b)

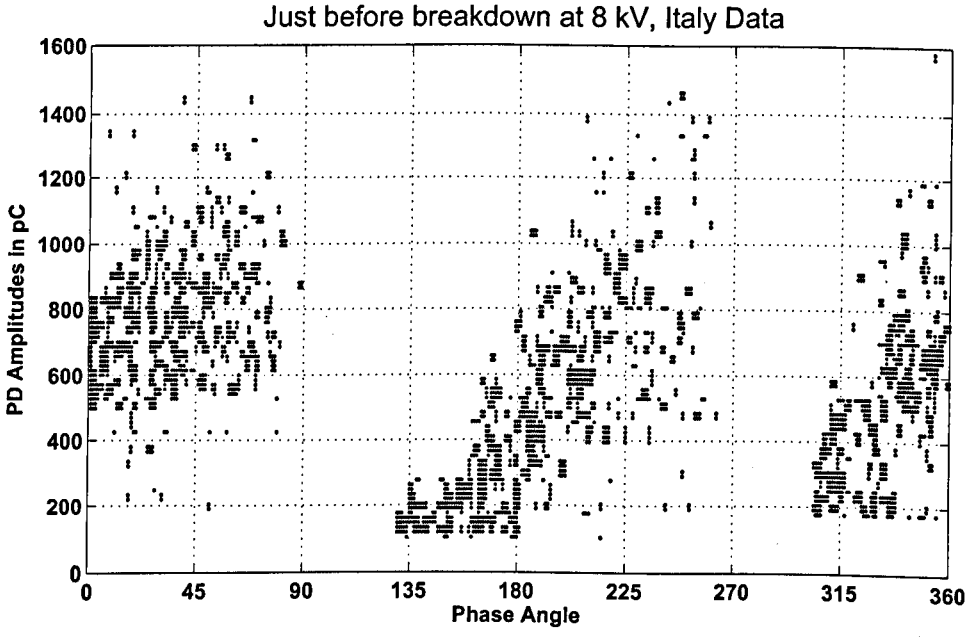

(c)

FIGURE 3.15: Accumulated Partial Discharge activity recorded in needle-plane geometry in a XLPE cable PD source at 7 and 8 kV applied voltages. (a) Before tree inception at 7 kV. (b) After tree inception at 7 kV. (c) Just before breakdown at 8 kV.

3.6 Summary

This chapter has presented an overview of all the PD data which have been pre-processed for chromatic processing. The data, which have been acquired from various investigators [4],[7],[8],[22] have been divided into two main categories : those concerned with PD activities produced by different sources and those obtained as the applied voltages have been increased for a fixed source condition and time variation progressing towards full breakdown.

The results presented show the complex nature of the data. Various features of the signals have been indicated. These are based upon the level of PD charge produced, the phase angle (during positive and negative half cycles) at which PD activity commenced. the phase angle duration of the PD activity...etc. This preprocessed data leads itself for quantification using phase angle domain, chromatic processing.

Chapter 4

Chromatic method of analysis

4.1 Introduction

This chapter describes the nature of the PD signals in their raw format first, taking one sample of Figure 3.14(c) from Section 3.5.2.2 as an example for illustration. The pre-processing method is then explained in detail. To illustrate the difference between different PD signal shapes encountered in real high voltage equipment, some examples of the pre-processed PD signals generated from multiple PD sources have been plotted.

The mathematical transformation of the pre-processed PD signals from the three non-orthogonal R, G, B filters to the x, y, z and H, L, (1-S) chromatic parameters sets is described. The inter-relationship between the different chromatic parameters of the same set, (e.g. x, y, z), is illustrated in a variety of diagrams.

Key diagrams highlighting the inter-relationship between the different chromatic parameters x, y, z are presented. The inter-relationship between the different parameters, H, L, (1-S) is also been described.

PD signals in real HV equipment can take various shapes and geometries. To assess the validity of the chromatic method with all types of PD signals which might occur in real situations, model signals were selected to imitate the variety of real PD signals which could occur. Key fundamental model signals as well as complex model signals are presented and chromatically processed.

4.2 Pre-processing of Raw Data

As stated in Chapter 3, the raw PD data collected from HV equipment using PD detectors can be recorded as time or phase varying signals. The most popular representation of PD signals is the 3-D $(\varphi - q - n)$ representation as shown in Figure 2.6 [4] [7] [8] [22] which is the phase varying signal that includes also the number of PD events per phase angle. One of the key derivatives of the latter form is the $(\varphi - q)$ distribution.

Figure 4.1 shows the 2-dimensional plot $(\varphi - q)$ of PD activity derived from the 3-D plot in Figure 2.6; it shows one period of the 50 Hz 5 kV applied wave along with a normalised accumulation of PD activity over 3 minutes duration of the test. The normalisation is achieved by dividing the the actual PD amplitude by the maximum range of the PD detector.

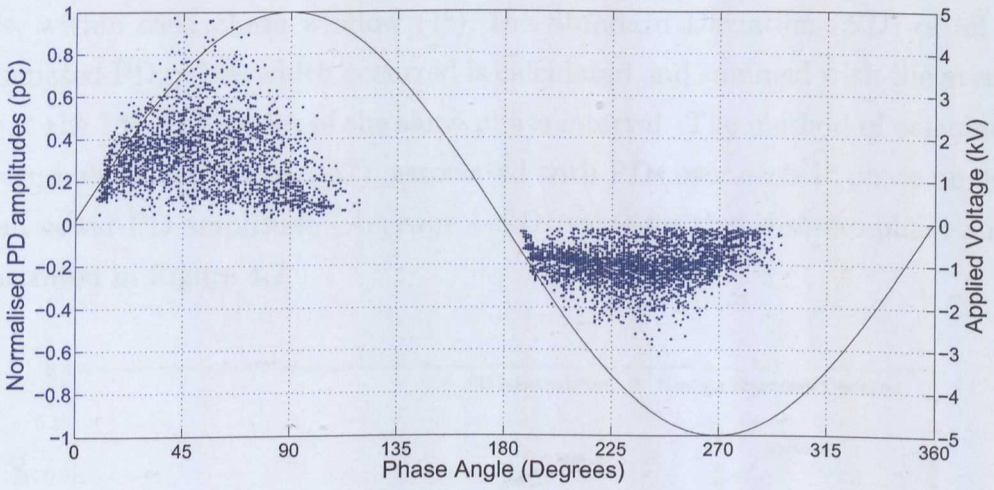

FIGURE 4.1: 50 Hz wave and the normalised PD accumulation (pC) for each phase angle over a 3 minute period.

Each discharge pulse in the pattern reflects the physical process at the discharge site and a strong relationship has been found between the features of these patterns and the type of defect causing them [3].

The profiles of $(\varphi - q)$ and $(\varphi - q - n)$ characteristics provide information about defects in insulation in which partial discharges are taking place. It is necessary to quantify the profiles for pattern recognition.

4.3 Pre-processing Method

The PD data signals are obtained in relation to the waveform of the AC test voltage. The test voltage is assumed to be held constant during each data acquisition and the voltage phase angle is divided into a suitable number of small intervals of 1^o width [3].

One can obtain both the magnitudes (q) of PD pulses and the number generated (n) in each phase window (φ). One of the resulting PD distributions would be the ($\varphi - q$) (*aka* PRA).

Of the two main possible distributions, which have been used for analysis by researchers to-date; ($\varphi - q_{max}$) and ($\varphi - q_{ave}$), (i.e.maximum and average PD pulse amplitudes as a function of their phase of occurrence), the ($\varphi - q_{ave}$) was chosen using the Standard Deviation of the signal for each 1^o phase interval.

Hence, within each phase window (1^o), the Standard Deviation (SD) of all the accumulated PD pulses which occurred is calculated and summed with the average value of the PD amplitudes of the same phase interval. The method of calculating the accumulation of charge (pC), associated with PDs over each 1^o phase angle to give an newer PD amplitude ($Average + SD$) value for that discrete phase angle, is illustrated in Figure 4.2.

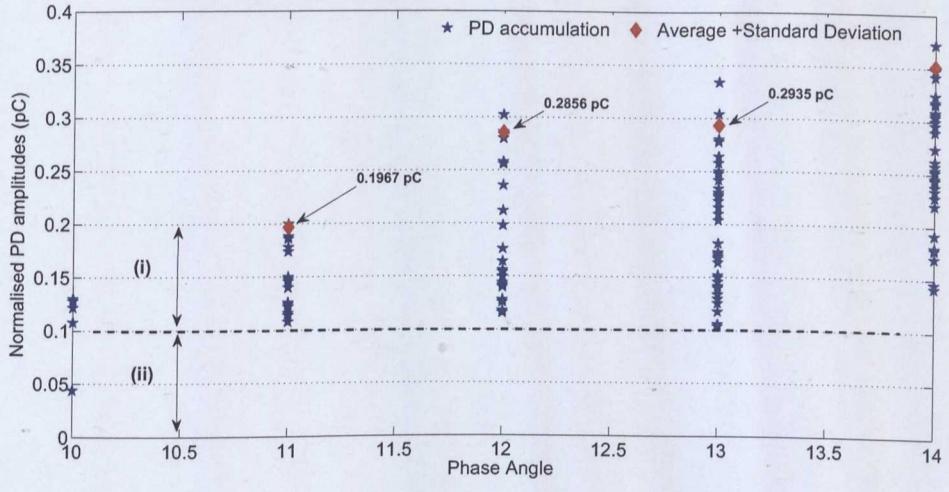

FIGURE 4.2: Individual PD amplitudes leading to PD accumulation (average value + standard deviation) per 1^o phase angle (i) : Signal (ii): Noise threshold

Figure 4.2 gives a numerical example of the calculation method, using three 1^o intervals of Figure 4.1, at 11^o, 12^o and 13^o respectively. For the first 1^o interval, at 11^o, the individual discharges $(Ave + SD)$ sum to give a total of 0.1967 (which corresponds to 98.35 pC before normalisation). PD levels below a threshold value of 0.1 (corresponding to 50 pC) were excluded from the accumulation in order to avoid excessive noise. The calculated standard deviations of normalised charges over the other two angles, 12^o and 13^o, were 0.2856 and 0.2935 respectively.

Figure 4.3 shows examples of accumulated PDs (calculated as shown on Figure 4.2) as a function of electrical phase angles through the 360^o period of the 50 Hz wave.

Since PD activity varies depending on its source, examples of pre-processed PD signals from various PD sources are shown in Figure 4.3. The PD amplitudes had been normalised (PD amplitude divided by the maximum range of the PD detector) throughout the data processing, as mentioned in the previous section.

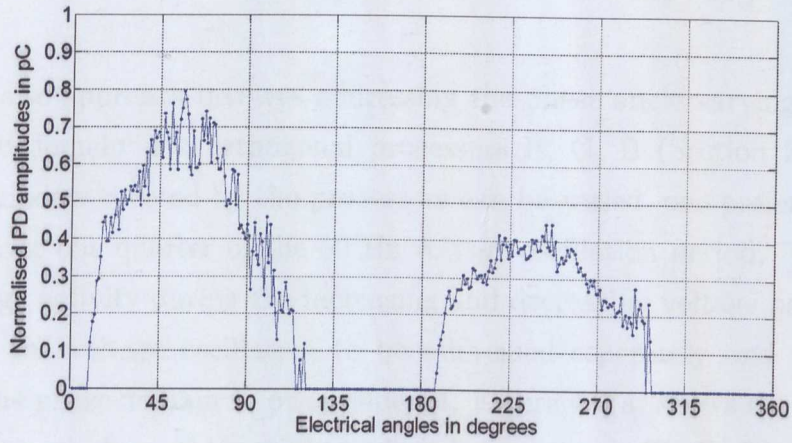

(a) From an Internal PD source at 5 kV [4]

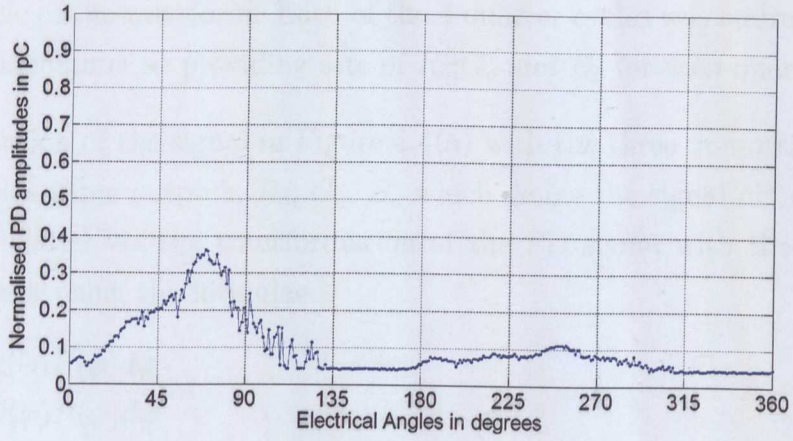

(b) From a Surface PD source at 6 kV [7]

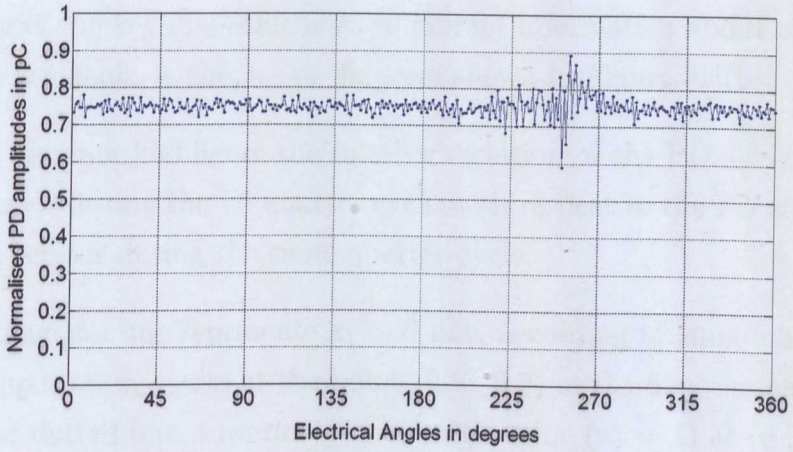

(c) From a Corona PD source at 8 kV [7]

FIGURE 4.3: Normalised accumulated PDs (calculated as shown on Figure 4.2) as a function of phase angle through the 360^o period of the 50 Hz wave from different PD sources

4.4 Chromatic Analysis of PD Activity

The chromatic approach involves addressing the phase angle varying signal with three phase domain non orthogonal processors R, G, B (Section 2.8 and [6]). The time window covered by the processors can be varied, one preferred window being to cover one quarter of the 50 Hz voltage oscillation period. This enables the discharge activity during the increasing and decreasing voltage parts for each polarity of the voltage oscillation to be addressed separately and for different sectors of the phase domain to be considered. Figure 4.4(a) shows the deployment within such a window, of three phase domain processors (R, G, B) covering the first quarter cycle of the voltage oscillation.

The overlapping R, G, B processors in Figure 4.4(a) are shown covering the 1^{st} quarter cycle of the waveform. Each of the 4 quarter cycles was addressed sequentially in this manner so providing sets of R_o,G_o and B_o for each quarter cycle.

The convolution of the signal in Figure 4.4(a) with the three non-orthogonal processors, yields three outputs, R_o, G_o, B_o which define the signal distribution and can be calculated via the transformation of the PD signal with the response of each processor using the formulae:

$$R_o = \int_0^{90} R(\varphi)P(\varphi)d\varphi$$
$$G_o = \int_0^{90} G(\varphi)P(\varphi)d\varphi$$
$$B_o = \int_0^{90} B(\varphi)P(\varphi)d\varphi$$

where P is the normalised PD signal as a function of the electrical phase angle φ.

An example of the key diagrams used to extract information about chromatically processed PD signals, is the $z_1 : y_1$ diagram shown in Figure 4.4(b).

The $z_1 : y_1$ diagram highlights the relative variation of the PD signal covered by the B processor during the 1^{st} quarter cycle with respect to the PD signal covered by the G processor during the same quarter cycle.

The green diagonal line represents $x_1 = 0$ line, according to equation 2.12. From the same equation, x_1 starts at the point (0.5 , 0.5) in the diagram and increases, following the dotted line, towards its maximum value ($x_1 = 1$) at (0 , 0).

As the value of x_1 increases, the values of z_1 and y_1 decrease. The 3 parameters, x_1, z_1 and y_1 would meet at an equi-distance point (*aka* the white point W) which

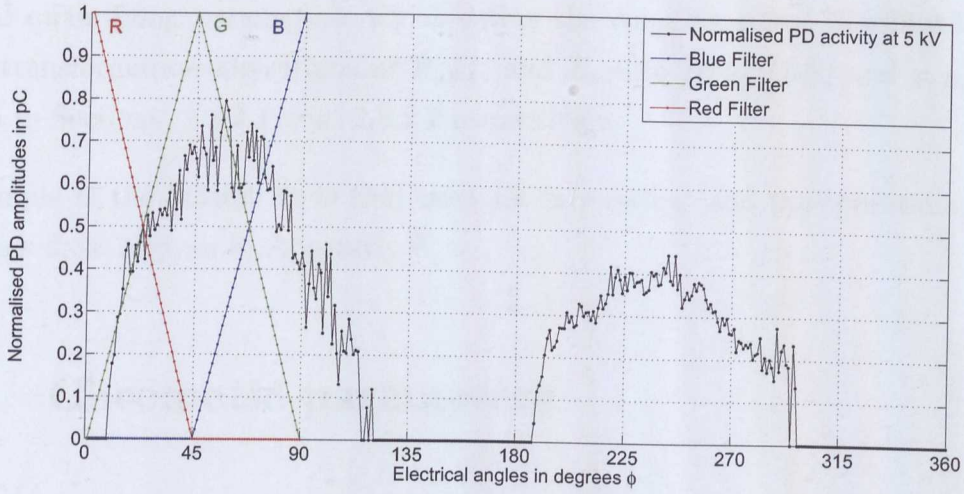

(a) R,G,B Non Orthogonal Processors deployed across the first Quarter Cycle

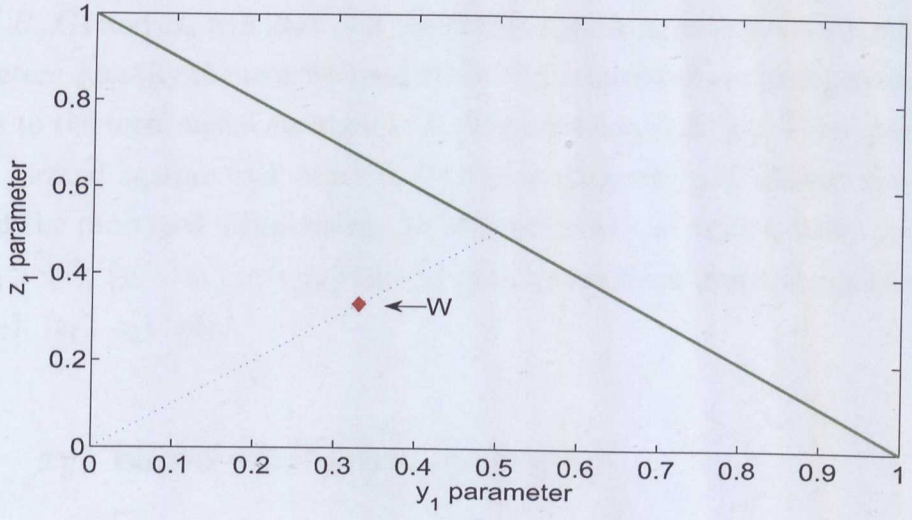

(b) $z_1 : y_1$ (the dominant phase angle diagram)

FIGURE 4.4: Normalised Amplitudes of PDs per Phase (integrated over 3 min) as a function of Phase Angle for PD activity at 5 kV, (Figure 4.3(a)) and key diagram $z_1 : y_1$

is at (0.33 , 0.33) in the $z_1 : y_1$ diagram. All parts of the PD signal under each processor, R, G, and B will have the same contribution at the W point.

More details about the $z_1 : y_1$ diagram and other different chromatic diagrams are given in Section 4.5.

These outputs may be transformed using various algorithms to produce other signal quantifying parameters, which define the complex signal distribution [6]. The transformation algorithms of R_o,G_o and B_o into H, L, (1-S) and x, y, z are given in Sections 2.8.2.1 and 2.8.2.2 respectively.

A sample of the Matlab code that used for processing (and pre-conditioning) of the raw data is given in Appendix B.

4.5 Chromatic parameters

4.5.1 The xyz chromatic parameters

It has been established, in Section 2.8.2 Chapter 2, that the chromatic transformation of R_o,G_o and B_o will lead to a signal distinguishing parameters x, y, z. These parameters quantify the relative magnitude of the output from each processor with respect to the total signal strength to satisfy equation 2.12 [6]. These parameters can be plotted against each other in Cartesian diagrams to highlight specific features of the processed signal using, parameters from the same quarter cycle; (z_1 : y_1), (z_1 : x_1), (y_1 : x_1) or a mixture of parameters from different quarter cycles; (z_1 : x_2), (z_1 : z_3)...etc.

4.5.2 xyz based chromatic diagrams

A signal may therefore be represented as a point on a chromatic Cartesian diagram with coordinates (x : z), (y : z) and (x : y). Significant features of such a diagrams are as follows, taking a y : z diagram as an example:

1. The locus $y + z = 1$ represents signals with no x (i.e. R) component
2. The locus $y = z$ represents a scale for the x component.
3. The point 0.33, 0.33 represents a signal with equal contributions from each of the three processors.

Corresponding interpretations exist for the $x : z$ and $x : y$ diagrams. Although each of these diagrams is two dimensional in nature (e.g $y : z$), the value of the third dimension (e.g. x) is also represented as a consequence of equation 2.12.

Depending on the features sought from the analysis, the results of such chromatic transformations for all the four quarter cycles of the AC wave may also be displayed using various chromatic diagrams. Each quarter cycle is represented by a set of x, y, z parameters; e.g. the 1^{st} quarter cycle is represented by x_1, y_1 and z_1, the 2^{nd} quarter cycle with x_2, y_2 and z_2 and so forth. Features of the PD signals can be extracted using these parameters of the 1^{st} quarter cycle or from the combination of the parameters of all the quarter cycles.

Figure 4.4(b) shows a Cartesian diagram of $z_1 : y_1$ from which an indication of the dominant phase angle can be obtained as the ratio for any part of (z_1 / y_1) [6]. The point W (0.33, 0.33) represents equal contributions from all sectors of the quarter cycle and is one indicator of possible full breakdown when a signal trajectory converges towards it.

An important aspect of such signal representation on the chromatic map is that the relationship between two signals is easily visualised and the superposition of two complex signals can be conveniently determined using simple moment equations [5].

4.5.3 Comparison of different quarter cycles in x, y, z

Figure 4.5 shows that the deployment of the R,G,B processors can be for any of the four quarter cycles of the whole phase angle range of the PD signal of Figure 4.4(a). The sectors within the half cycles that are represented by the chromatic parameters have been highlighted.

The part of the signal in the 1^{st} quarter cycle covered by the B_1 processor is represented by z_1, the adjacent part of the same signal in the 2^{nd} quarter cycle covered by the R_2 processor is represented by x_2. The symmetry between the two adjacent quarter cycles can be deduced from the characteristics determined from the R_1, G_1, B_1 and R_2, G_2, B_2 of Figure 4.5(a).

Figure 4.5(b) shows a chromatic diagrams of $z_1 : x_2$, which involves the 2^{nd} quarter cycle in addition to the 1^{st}. z_1 corresponds to the first quarter cycle processor

adjacent to the second quarter cycle and x_2 corresponds to the second quarter cycle processor adjacent to the first quarter cycle. The line from the origin through the white point W corresponds to both adjacent quarter cycles being symmetrical. Similarly the use of processors z_3 and x_4 can be used to consider the 3^{rd} and 4^{th} quarter cycles.

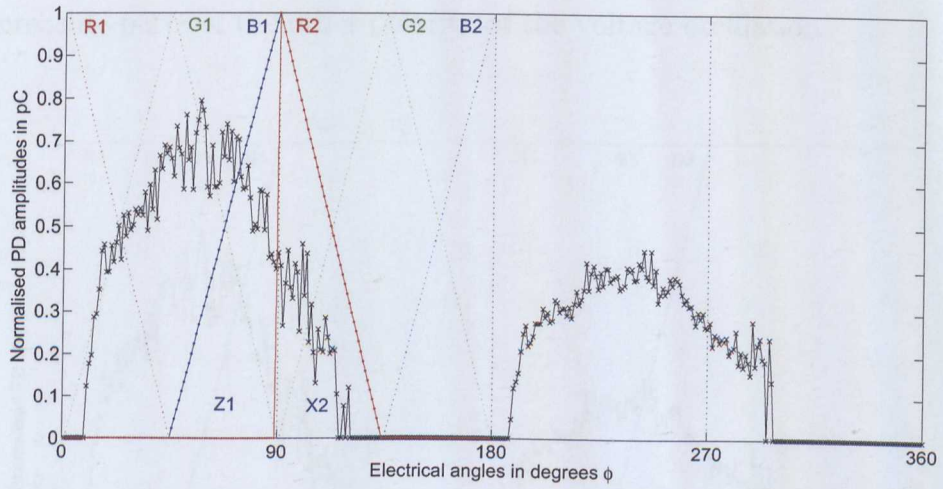

(a) R,G,B covering the 1^{st} and 2^{nd} quarter cycles, B_1 and R_2 highlighted

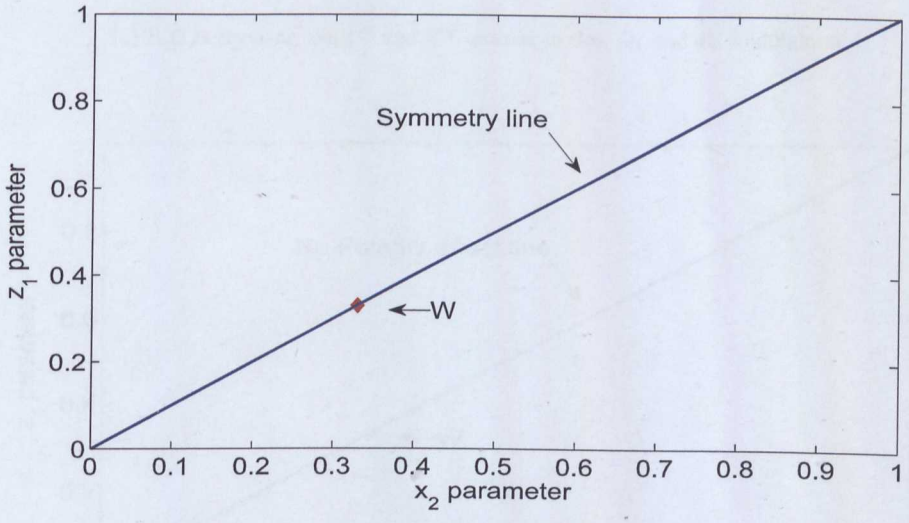

(b) The use of z_1 and x_2 for quantifying PD signal features (Symmetry)

FIGURE 4.5: Deployment of R,G,B processors on 1^{st} and 2^{nd} quarter cycles

In Figure 4.6(a), the processer B_3 covers the 3^{rd} part of the signal, which is represented by z_3. In conjunction with z_1, the effect of the sinewave polarity on the

PD activity could be deduced from the characteristics determined from the R_1, G_1, B_1 and R_3, G_3, B_3 of Figure 4.6(a).

Figure 4.6(b) shows a Cartesian diagram of $z_1 : z_3$ from which an indication of the polarity effect can be obtained. The line from the origin through the point W (0.33, 0.33) corresponds to both polarities making equal contributions (i.e. no polarity effect). The $z_2 : z_4$ diagram assesses the polarity during the decreasing and increasing parts of the other polarity of the voltage oscillation.

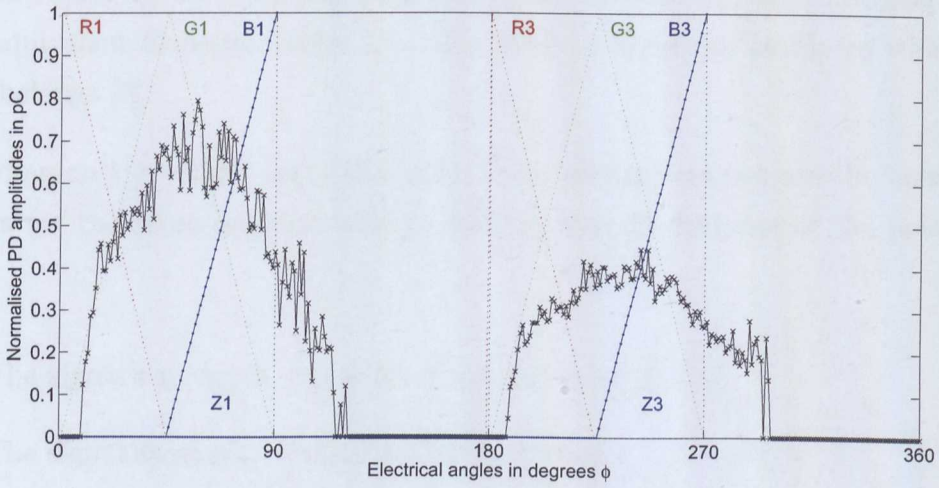

(a) R,G,B covering the 1^{st} and 3^{rd} quarter cycles, B_1 and B_3 highlighted

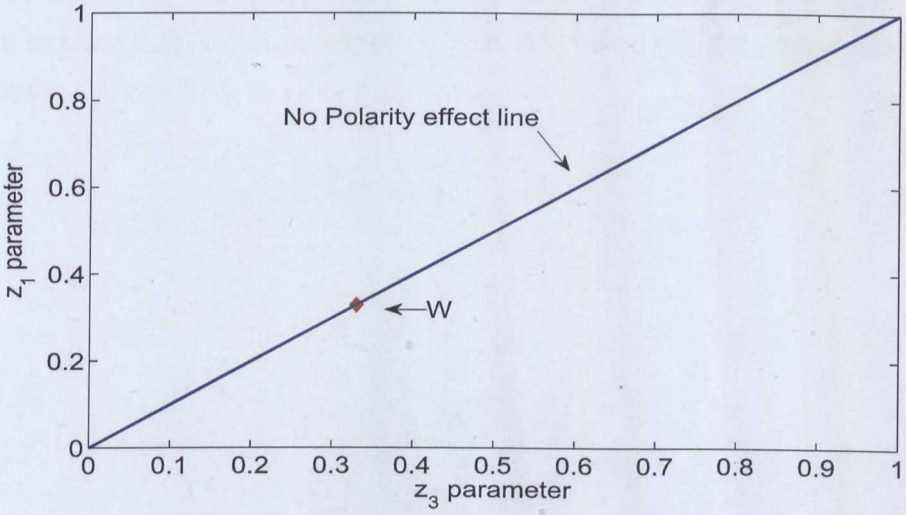

(b) The use of z_1 and z_3 for quantifying PD signal features (Polarity Effect)

FIGURE 4.6: Deployment of R,G,B processors on 1^{st} and 3^{rd} quarter cycles

4.5.4 H,L,(1-S) chromatic parameters

An alternative transformation of R_o,G_o and B_o leads to a different set of signal identifying parameters; H, L, S where H quantifies a dominating parameter value, L the effective strength of the signal and (1 - S) the nominal spread of the signal (Section 2.8.2, Chapter 2).

According to Jones *et al* [5], if the distribution of the signal was truly Gaussian, H, L, (1-S) would represent the features shown on Figure 4.7. Thus for a more complex signal, H, L, (1-S) may be regarded as representing the three attributes of an equivalent Gaussian signal i.e. they define a Gaussian family to which the signal belongs [6].

Depending on the sought signal features, these parameters can also be combined in pairs for the same quarter cycle to address specific features of the processed signal;

1. The signal's strength versus its dominant value $L : H$,
2. The signal strength versus its nominal spread $L : (1 - S)$,
3. The signal's spread versus its dominant value $(1 - S) : H$

Alternatively, these may be used in conjunction with the x, y, z parameters, for example as the signal effective amplitude versus the retaliative contribution of the B processor $L/(1 - S) : z$.

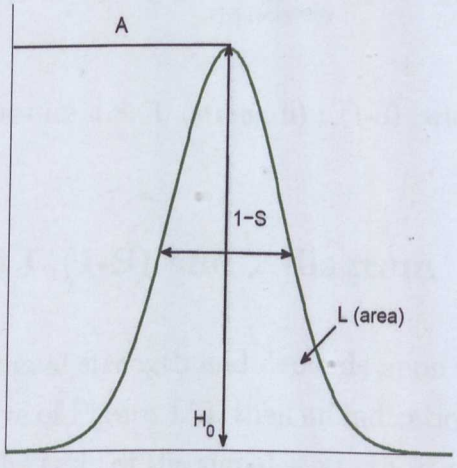

FIGURE 4.7: One interpretation of the Chromatic Parameters H, L, (1-S)

4.5.5 H,L,(1-S) based chromatic diagrams

In addition to the various chromatic diagrams and maps described in Section 2.8.2, Chapter 2, the inter-relationship between each parameter of the H,L,(1-S) set and parameters from the x, y, z set can highlight various signal properties and monitor PD signal behavior.

Figure 4.8 shows the Cartesian coordinates of the variation of the signal strength L with regard to the signal spread (1-S). The increase of L indicates a critical increase in the PD activity. The diagonal line shows a proportional relationship between the signal strength L and its spread (1-S).

One such a diagram can be important in terms of quantifying the physical relationship between L as an entity representing the area under the curve along with its width, and the spread of this entity along the parameter range.

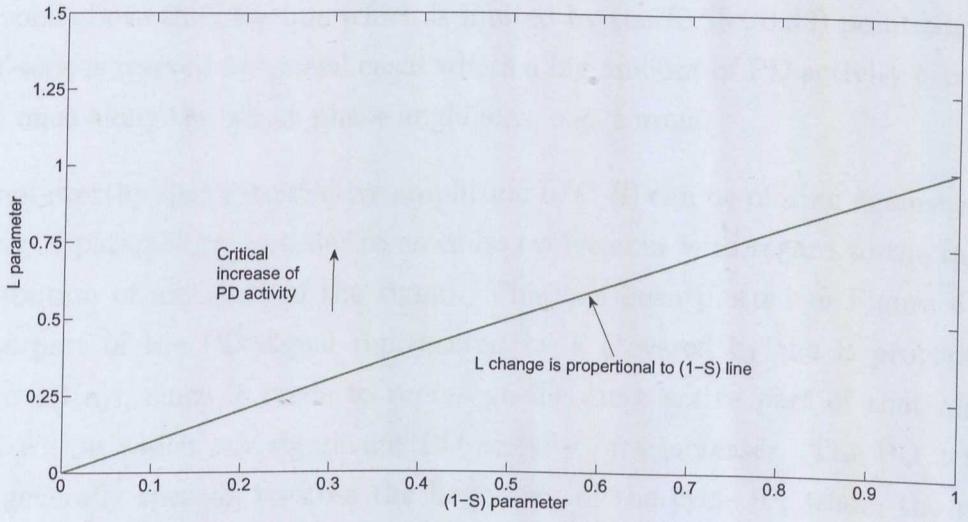

FIGURE 4.8: L (strength) : (1-S) (width)

4.5.6 Combined L,(1-S) and z diagram

Since L represents the signal strength and depends upon the amplitude and width (e.g. area under the curve of Figure 4.7), then an indication of the signal amplitude may be obtained from the ratio of the signal strength to signal width, i.e. L/(1-S). This new discriminating parameter can be plotted against z to highlight specific signal features.

Figure 4.9(a) represents the variation of the PD signal strength L with regard the relative contribution of the PD signal under the B processor, reflected by z. The decrease of z parameter will indicate a shift of the PD activity towards the beginning of the quarter cycle, since B covers the early phase angles. PD activity is known to start around the peak of the applied voltage, hence the choice of the of the chromatic parameters z which reflects the area under the B processor.

Figure 4.9(b) shows a chromatic diagram which quantifies the variation of the signal's effective amplitude L / (1 - S), with regard the relative contribution of the PD signal represented by z. The horisontal blue line corresponds to L and (1-S) having the same value, which indicates that the PD activity's strength is changing at the same rate as its spread. As PD activity increases, three distinctive zones will become distinctive in the diagram, normal, medium and high activity zone. The borders of these zones will be dictated by the levels of the real data processed, as PD activity varies with different conditions.

The zone above the blue line which is limited by the (0.33 , 0.33) point edge and the Y-axis is reseved to special cases where a big amount of PD activity is created all at once along the whole phase angle axis, e.g. corona.

It is noteworthy that the effective amplitude L/(1-S) can be plotted against any of the x, y, z parameters, in order to asses its evolvement with regard to the relative contribution of any part of the signal. This has been plotted in Figure 4.9(b), as the part of the PD signal represented by z (covered by the B processor in Figure 4.4(a)), since it tends to represent the most active part of that quarter cycle, within which any significant PD activity first increases. The PD activity then generally spreads towards the beginning of the cycle 0°, where the power frequency rate of change of voltage dv/dt is at its highest.

If the PD activity only occurred near the peak of the AC voltage, then $z = 1$ (since R = G = 0 according to equation 2.12, Section 2.8.2.2). As the PD spreads to lower voltages of the AC wave, then the value of z progressively decreases to being indicative of the spread of PD activity. This spread indication is different from (1-S) in highlighting the spread across the whole quarter cycle and not only one half of the quarter cycle.

The sensitivity of S is from zero to low when the signal lies only under the B and G processors, whilst z would give higher sensitivity in this case, as z quantifies the contribution of the signal under the B range.

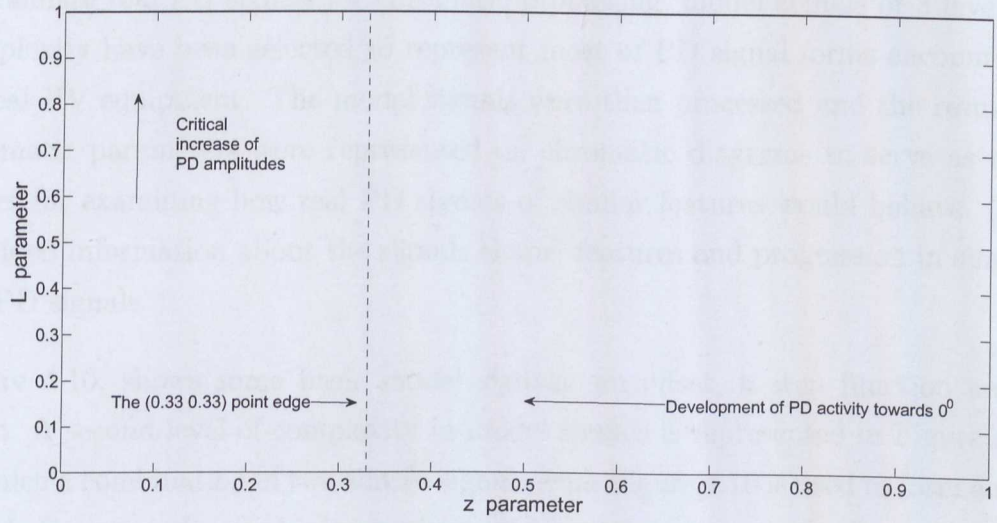

(a) Strength : z

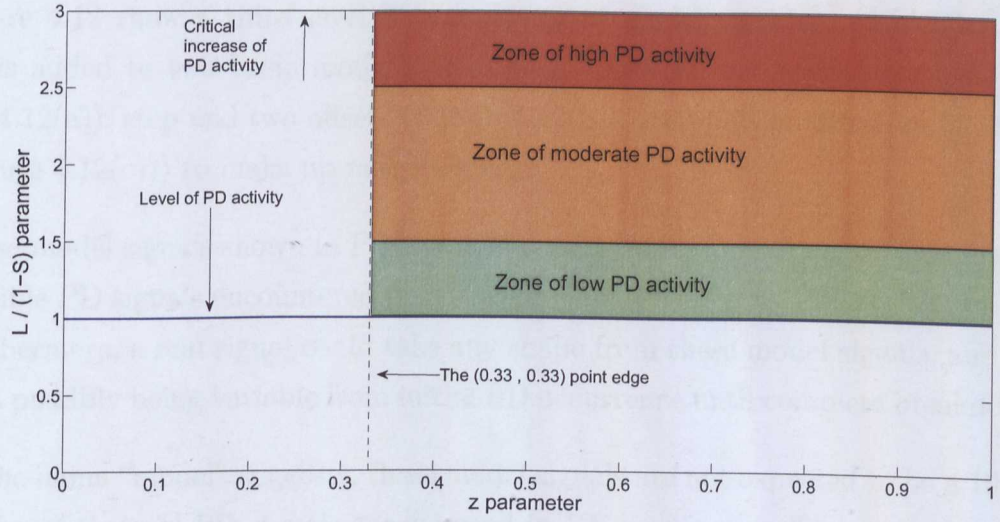

(b) Amplitude (L / (1 - S)) : z

FIGURE 4.9: Signal discriminations in terms of L, (1-S), z

4.6 Model Signals

Real PD signals can be diverse in form and magnitude, depending on various factors (PD source, dielectric used, applied voltage,...etc) [4] [7] [8] [22]. In order to simulate real PD signals for chromatic processing, model signals of 3 levels of complexity have been selected to represent most of PD signal forms encountered in real HV equipment. The model signals were then processed and the resulting chromatic parameters were represented on chromatic diagrams to serve as templates for examining how real PD signals of similar features would behave. This provided information about the signals shape, features and progression in time of the PD signals.

Figure 4.10, shows some basic model signals; an offset, a step function and a ramp. A second level of complexity in model signals is represented in Figure 4.11 in which a combination of two simple signals from Figure 4.10 is used to form a new signal. For example, combining positive and negative steps yields the rectangular distribution (Figure 4.11(a)), a ramp and a step gives the triangular distribution (Figure 4.11(b)), a ramp and an offset yields a clipped ramp (Figure 4.11(c)).

Figure 4.12 show a third level of complexity of model signals, in which an offset is added to two basic model signals (e.g. positive and negative steps (Figure 4.12(a)), step and two offsets (Figure 4.12(b)), step plus an offset and a ramp (Figure 4.12(c))) to make up newer signals.

These model signals shown in Figures 4.10 to 4.12 are representative of a range of possible PD signals encountered in HV equipment, as in [4] [7] [8] [22], Chapter 3. Furthermore, a real signal could take any shape from these model signals, and the form possibly being variable from initial PD occurrence until complete breakdown.

As the name "model" suggests, these model signals are not expected to be a 100 % replica of the real PD signals encountered in HV equipment. They would rather simulate a whole spectrum of PD signal shapes and their chromatic processing would give an indication about PD signal shapes and features from beginning of PD activity up to the total breakdown of the insulating material.

A visual inspection of Figures 3.6 - 3.15 indicates that all the PD signals processed fall in the range of the model signals selected.

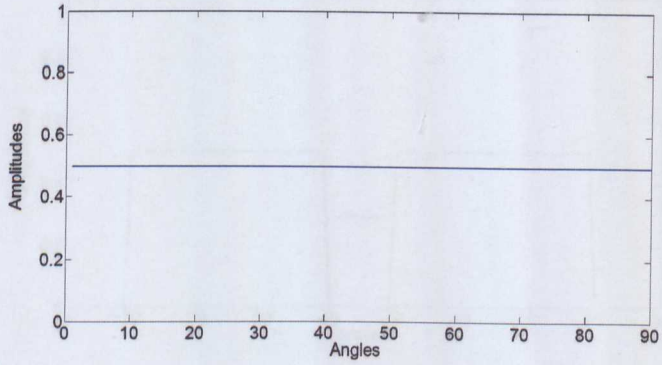

(a) An Offset

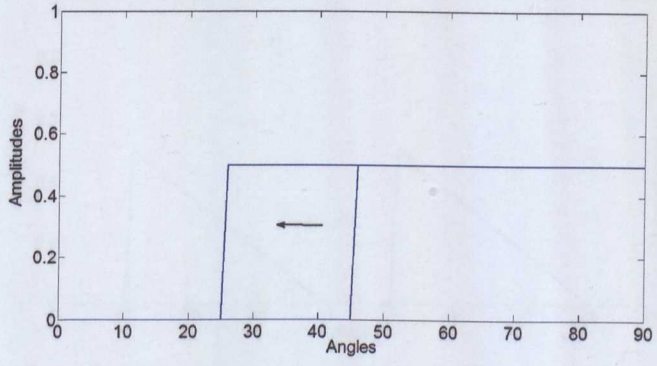

(b) Step Function

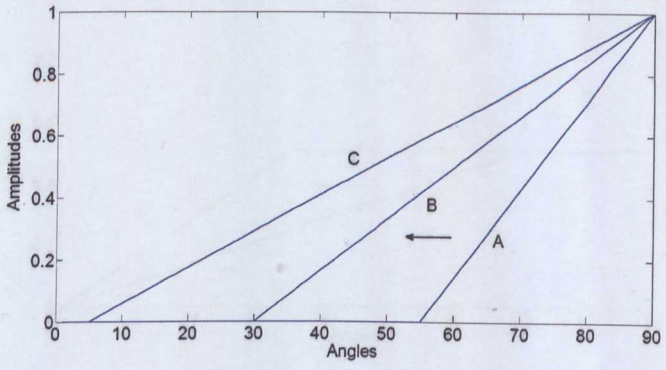

(c) A Ramp

FIGURE 4.10: Basic model signals.

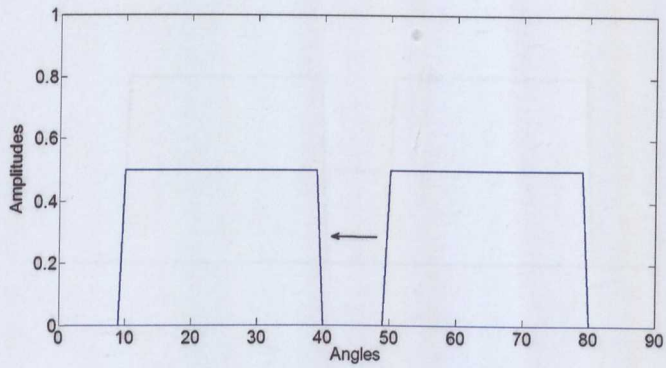

(a) Rectangular pulse

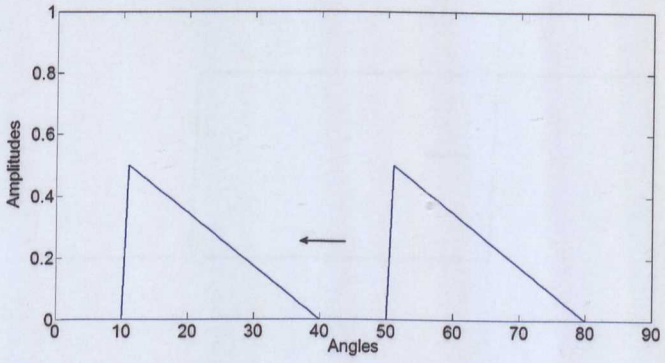

(b) Right Triangle pulse

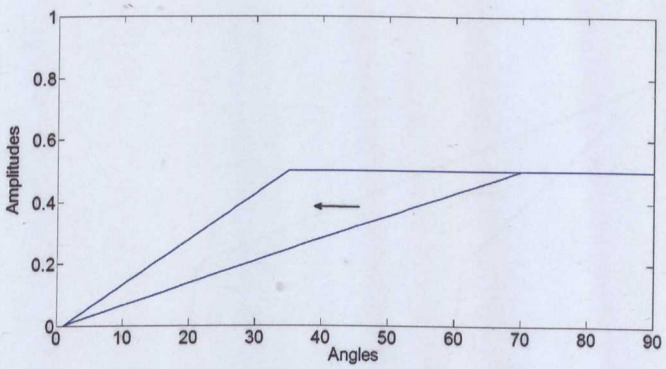

(c) Clipped Ramp Function

FIGURE 4.11: Complex model signals found from the superposition of two basic model signals.

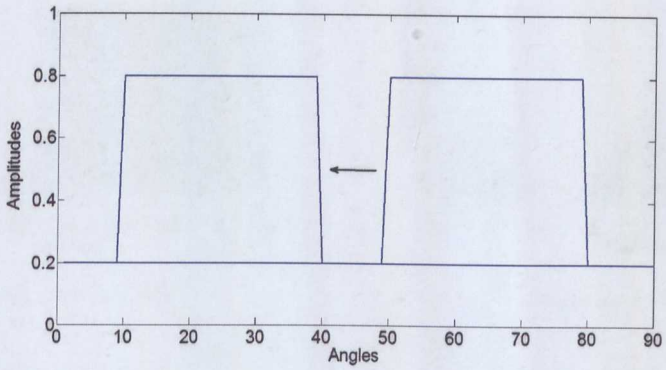

(a) Rectangular pulse with Offset

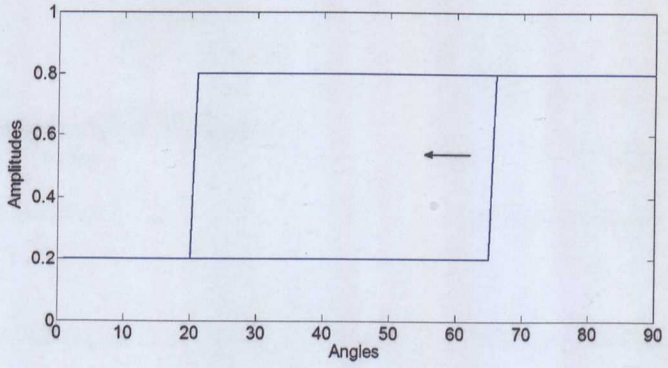

(b) Step with Offset

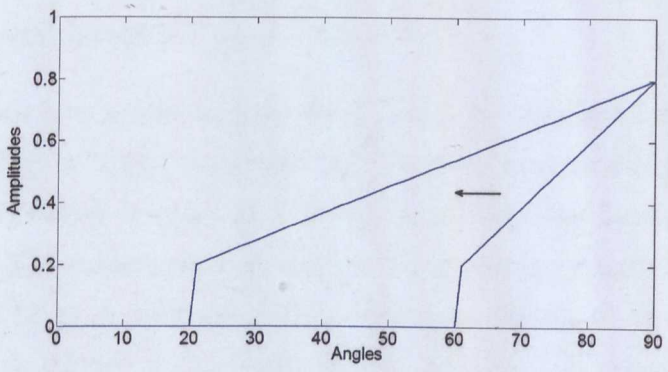

(c) Ramp with Offset

FIGURE 4.12: Complex model signals from an offset combined with other basic model signals.

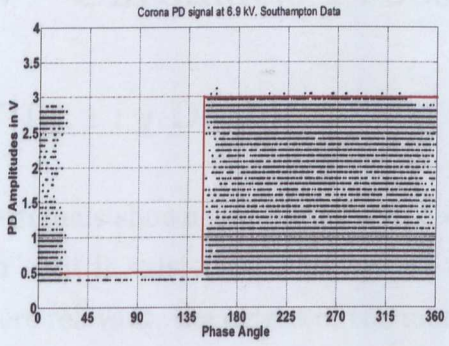

(a) Step with an offset

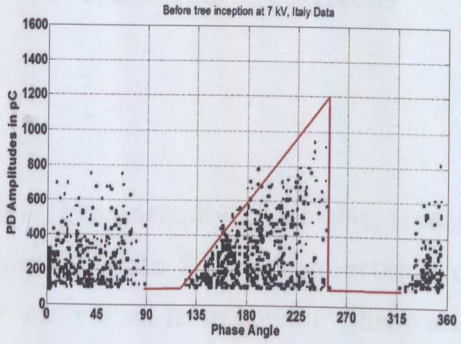

(b) Ramp wih offset

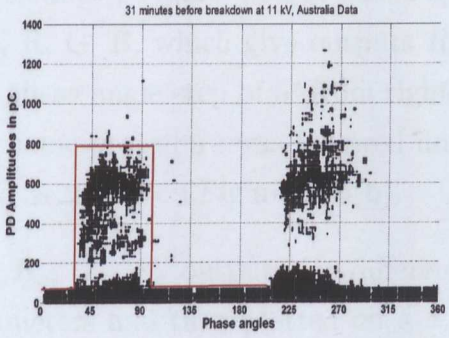

(c) Top hat with a step

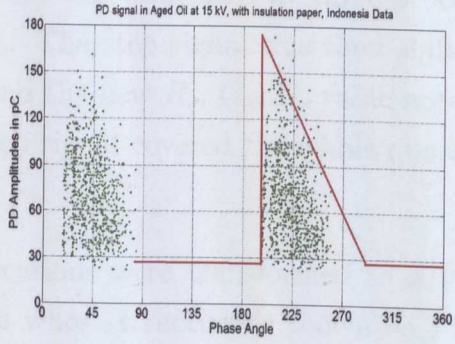

(d) Right triangular with an offset

FIGURE 4.13: Comparison between real and model signals.

The shapes of the model signals were initiated by a visual inspection of the real PD signals. Then the range of model signal shapes was extrapoltated to include different shapes which real PD signals might take.

Figure 4.13 shows how model signals were chosen to simulate few of the real PD signals. When Figure 3.9(a) is plotted on the same graph as Figure 4.12(b), the close similarity between the real and model signal becomes apparent as shown in Figure 4.13 (a). The same principal applies when plotting Figure 4.10(c) (with an offset), Figure 4.12(a) and Figure 4.11(b) (with an offset) on the same diagrams as Figure 3.15(b), Figure 3.12(c) and Figure 3.11(b). The resulting graphs are shown respectively on Figures 4.13 (b), (c) and (d).

4.7 Chromatic Processing of Model Signals

4.7.1 $z : y$ Diagrams

The signals shown in Figures 4.10 to 4.12 were chromatically processed, treating each as if it existed within a phase angle range of 0^o to 90^o i.e a quarter cycle. Where relevant, the extent of the model signal was varied from the 90^o phase angle in steps of 5^o towards 0^o phase angle.

For example, Figure 4.14(a) shows a step signal being addressed by three processors, R, G, B, which give outputs R_o, G_o, B_o. The step signal was then shifted one phase angle step of 5^o from right to left and the new R_o, G_o, B_o value noted. The same procedure was followed until the step signal covered the whole quarter cycle as shown on Figure 4.14(b).

The R_o, G_o, B_o outputs for different step locations were transformed to x, y, z parameters and then plotted on a $z : y$ graph whose structure is shown on Figure 4.15(a). Figure 4.15(b) shows the series of points on the $z : y$ graph corresponding to the step front but at different phase angles as per Figure 4.14(a).

This shows the points commencing at $z = 1$, $y = 0$ and progressing along the line $y + z = 1$ before deviating to approach $z = y = 0.33$ when the step extends across the 0^o—90^o phase angle range. This latter point corresponds to an effect whose $z : y$ position is $z = y = 0.33$ (Figure 4.15(a)).

Applying the same procedure to the ramp signal (Figure 4.10(c)) leads to the trajectory shown on Figure 4.15(c). In this case, the locus of points deviates from the $z + y = 1$ line earlier and do not reach the $z = y = 0.33$ point when the foot of the ramp extends across the whole 0^o—90^o angle range (curve c, Figure 4.10(c)).

Applying the procedure to the superposition of two basic model signals from Figures 4.11 (a, b, c) leads to the trajectories shown on Figure 4.16 (a, b, c) respectively. In these curves of the rectangular pulse and the right triangular pulse, the trajectory deviates from the locus $z + y = 1$ beyond its intersection with $z = y$. With the clipped ramp, the curve in Figures 4.16(c) is obtained.

Applying the procedure to the superposition of the basic model signals of Figures 4.12 (a, b, c) upon an offset leads to the trajectories shown on Figures 4.17 (a, b, c) respectively.

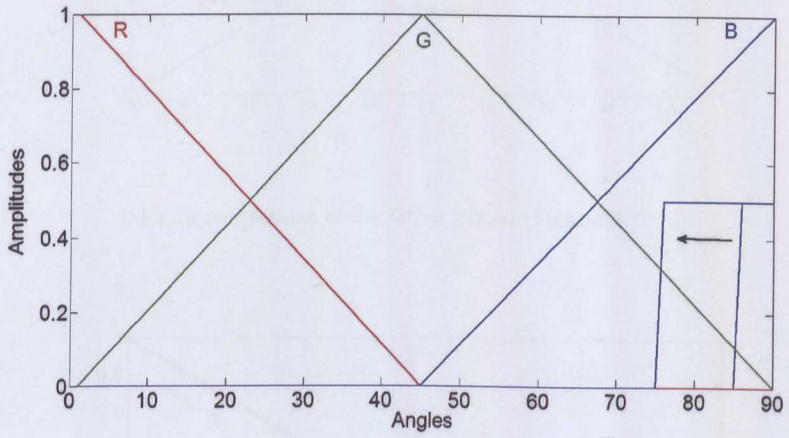

(a) Initial step location close to 90^o

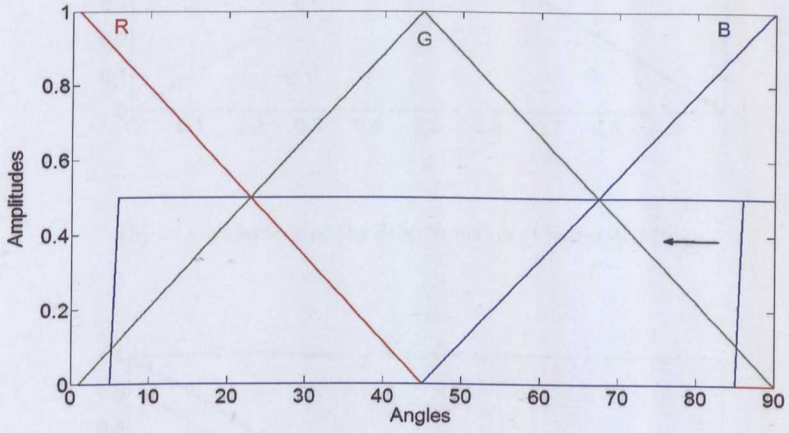

(b) Preliminary step location covering 90^o phase angle

FIGURE 4.14: Chromatic processing of a time stepped signal in the phase angle domain.

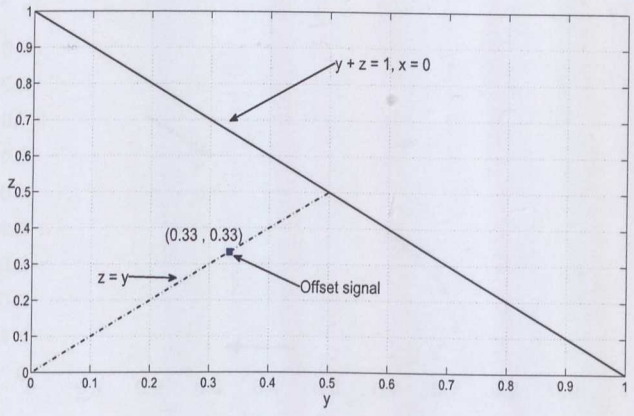

(a) $z : y$ coordinates of the Offset Signal (Figures 4.10(a))

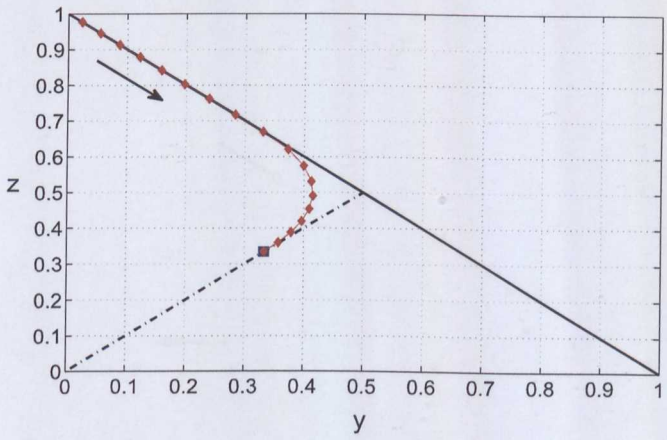

(b) $z : y$ trajectory of the Step Function (Figures 4.10(b))

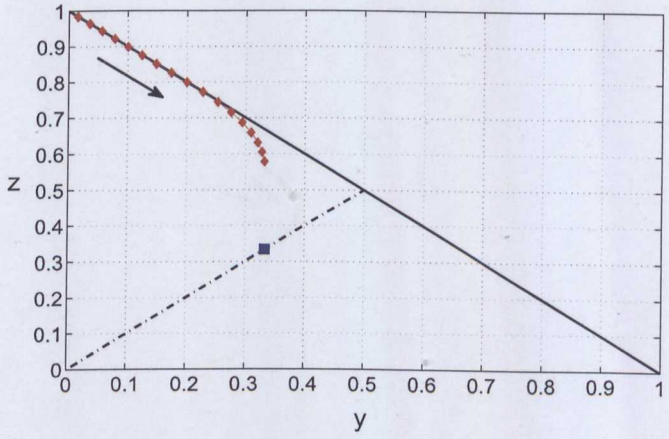

(c) $z : y$ trajectory of the Ramp Function (Figures 4.10(c))

FIGURE 4.15: $z : y$ characteristics of the basic Model Signals

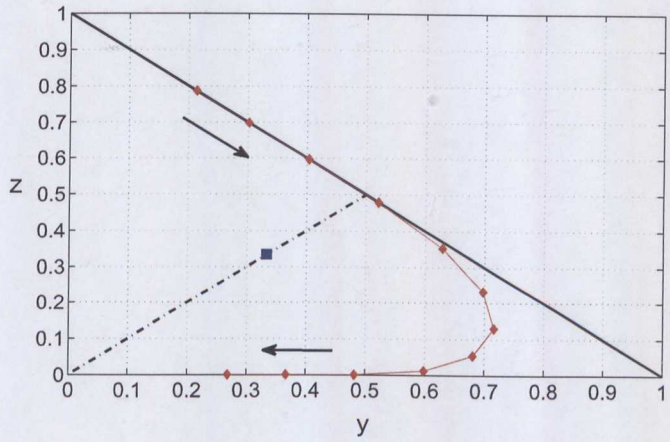

(a) $z : y$ trajectory of the Rectangular pulse (Figures 4.11(a))

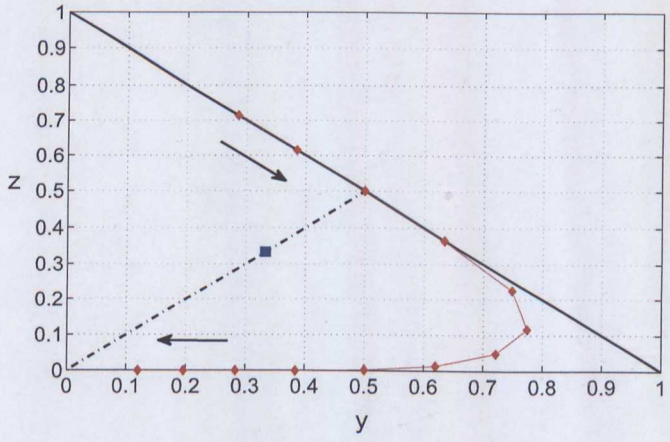

(b) $z : y$ trajectory of the Right Triangle Function (Figures 4.11(b))

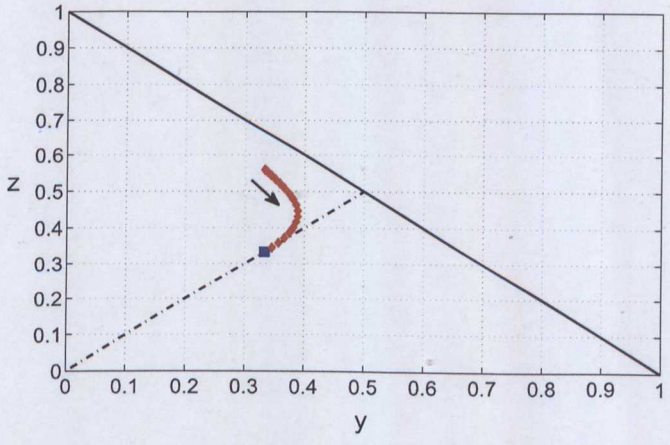

(c) $z : y$ trajectory of the Clipped Ramp Function (Figures 4.11(c))

FIGURE 4.16: $z : y$ characteristics of the superposition of two basic signals

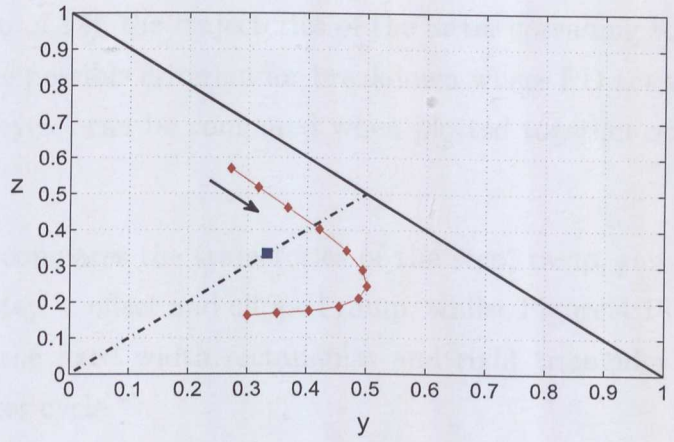

(a) $z : y$ of the Top Hat with Offset (Figures 4.12(a))

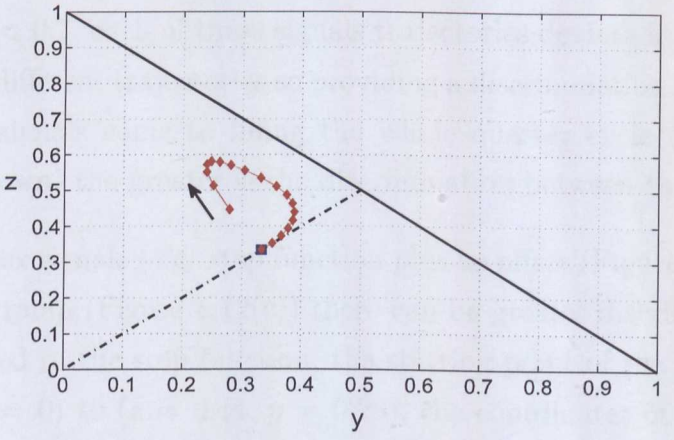

(b) $z : y$ of the Step with Offset (Figures 4.12(b))

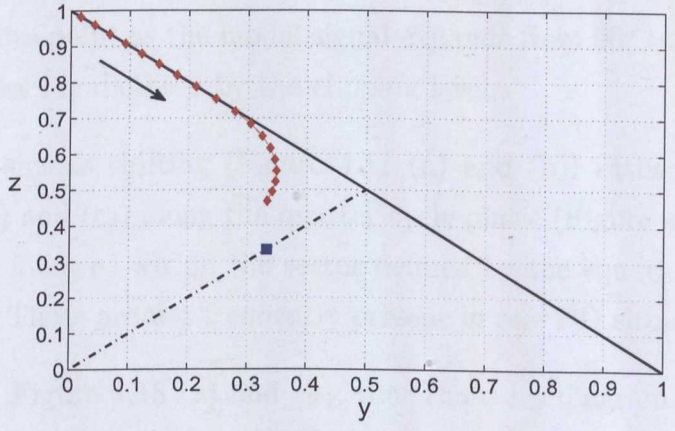

(c) $z : y$ of the Ramp with Offset (Figures 4.12(c))

FIGURE 4.17: $z : y$ characteristics of the Combined Model Signals with Offset

In order to appreciate the level of discrimination between different model signals (Figures 4.10 to 4.12), the trajectories of the latter spreading towards the (0.33 , 0.33) point (one possible criterion for breakdown where PD activity would fill the whole quarter cycle) can be compared when plotted together on a common $z : y$ diagram.

Figure 4.18(a) compares the trajectories of the step, ramp, ramp + offset (truncated ramp) , step + offset and clipped ramp, whilst Figure 4.18(b) compares the trajectories of the fixed width rectangular and right triangular pulses displaced along the quarter cycle.

Inspection of Figure 4.18(a) shows that initially (phase angle close to 90^o, $z > 0.7$), the Step, Ramp and Ramp + offset functions lie on the line $z + y = 1$ line. Consequently these signals cannot be discriminated on a $z : y$ diagram alone. However, for $z < 0.7$, each of these signals trajectories deviate from the $z + y = 1$ line and follow different trajectories so providing a discrimination possibility. Thus the closer the signals come to filling the whole quarter cycle (and progression towards breakdown) the greater is the discrimination between them.

For more complex signals (e.g. step function plus an offset (Figure 4.12(b)) or step function plus a ramp (Figure 4.12(c)) there can be greater discrimination. When an offset is added to the step function, the starting point of the trajectory shifts from ($z = 1$, $y = 0$) to ($z = 0.44$, $y = 0.28$), the coordinates of the latter being dictated by the offset level.

When the ramp is clipped from the top (Figure 4.11(c)), the trajectory of the new signal will commence from where the full ramp trajectory ended and progress towards the white point as the model signal expands from 90^o to 0^o. The starting point coordinates are dictated by the clipping level.

In the case of signals shifting (Figure 4.11 (a) and (b)) rather than extending (Figure 4.10 (b) and (c)) along the quarter cycle phase (Figure 4.18(a)), different trajectories are followed within the sector defined by the equations $x = z$, $z = 0$ and $z + y = 1$. These are not frequently present in real PD situations.

It is clear from Figure 4.18 (a) and (b), that the $z : y$ diagram can provide one level of discrimination between signals, particularly as the leading edge of the signal progresses towards a 0^o phase angle.

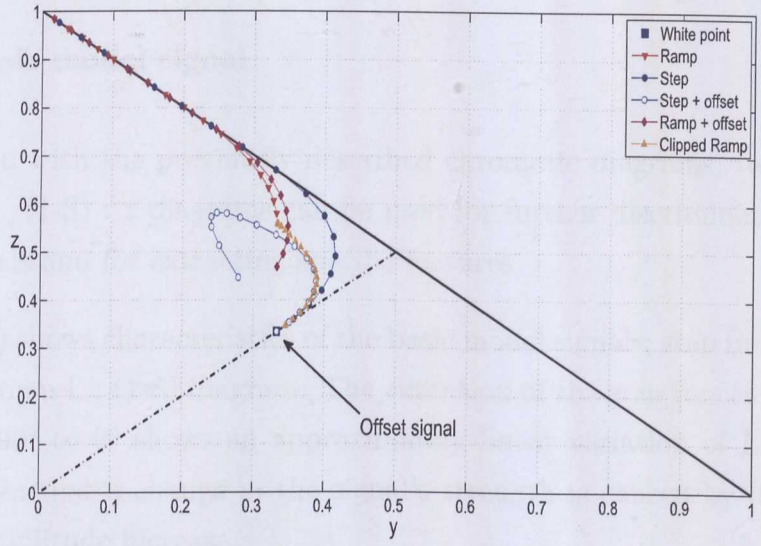

(a) Model signals where width gradually extends to fill the quarter cycle.

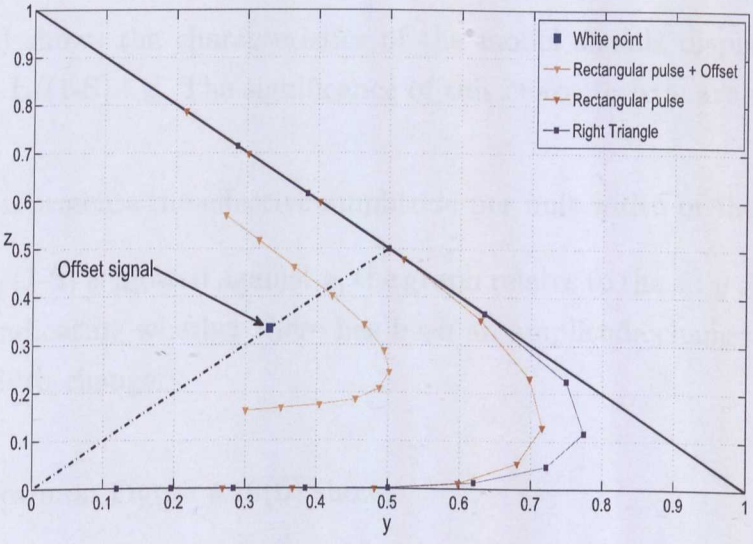

(b) Model signals of fixed width being displaced along quarter cycle.

FIGURE 4.18: Comparison of $z : y$ characteristics of basic and complex model signals with and without offset.

4.7.2 L, (1-S) Diagrams

4.7.2.1 Basic model signal

In conjunction with the previously described chromatic diagrams, (e.g. $z : y$), L : (1-S) and L /(1-S) : z diagrams can be used for further discrimination between different signals and for extracting specific features.

Figure 4.19(a) shows characteristics of the basic model signals; step function, ramp and an offset on a L : (1-S) diagram. The extension of the step function and ramp signals from 90^o to 0^o shows an approximately linear variation of L with (1-S), which indicates that a change in the signal's strength is caused by its spreading without an amplitude increase.

Steps and ramps of different amplitudes produce a change in the gradient of the L : (1-S) characteristic (compare Step and 1.5 Step in Figure 4.19(a)). An offset signal appears as a point (L = 1) (Figure 4.19(a)).

Figure 4.19(b) shows the characteristics of the model signals displayed on Figure 4.19(a) as L/(1-S) : z. The significance of this characteristic are :

1. L/(1-S) represents the effective amplitude per unit width of the signal.
2. When L/(1-S) is plotted against z, the graph relates to the $z : y$ characteristic (via z) indicating whether there has been an amplitude change as well as a signal width change.

The results shown on Figure 4.19(b) show:

1. For a step signal there is no substantial amplitude change (L = Constant) as it expands beyond $z = 0.9$.
2. A change in the step's height displaces the curve to a different L value.
3. A ramp signal also shows a tendency towards a constant L / (1-S) value but in a stepwise form (Step at $z = 0.8$).
4. The offset signal appears as a point with $z = 0.33$.

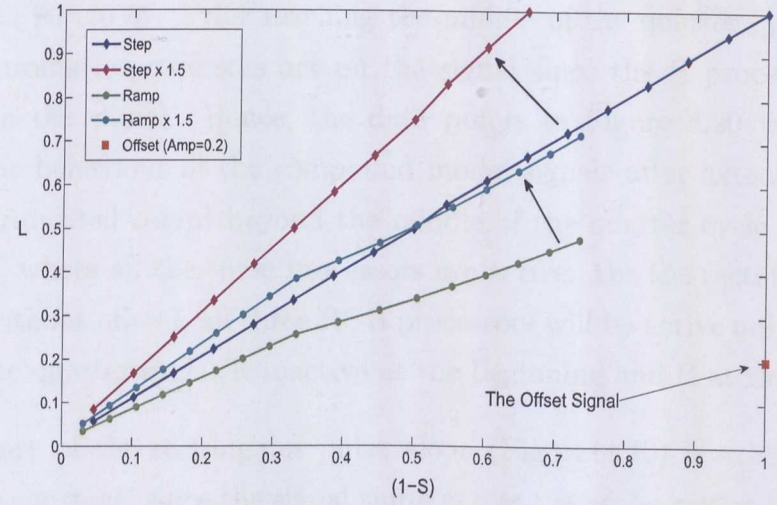

(a) L:(1-S) diagram.

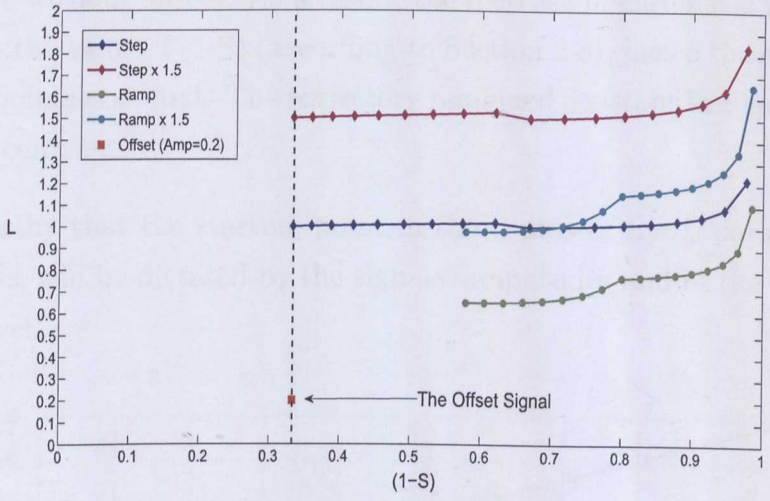

(b) L/(1-S) : z diagram.

FIGURE 4.19: L : (1-S) and L/(1-S) : z diagrams.

4.7.2.2 Compound model signal

Figure 4.20 shows L versus (1-S) characteristic curves for signals corresponding to a step + offset (Figure 4.12(b)), a truncated ramp (Figure 4.11(c)), a rectangular pulse (Figure 4.11(a)) and rectangular pulse + offset (Figure 4.12(a)).

The step + offset and the truncated ramp signals extend along the phase angle

domain whilst the triangular pulse with and without offset shifts along the phase domain from 90^o to 0^o. Prior reaching the middle of the quarter cycle, only the G and B chromatic processors act on the signal since the R processor will not overlap with the signal. Hence, the data points in Figure 4.20 were taken to represent the behaviour of the compound model signals after extending (step + offset and truncated ramp) beyond the middle of the quarter cycle 45^o up to 0^o phase angle, where all the three processors are active. For the rectangular pulses (with and without offset), all three RGB processors will be active only around the middle of the quarter cycle (R inactive at the beginning and B at the end).

The trajectory of the rectangular pulse alone (Figure 4.20) is a horizontal line because L is constant, since the signal shifts across the active region in the middle of the quarter cycle as an entity of constant width and fixed height.

The addition of the offset increases the part of the signal under the R processor (which was 0 without offset). As a result, the increase of chromatic parameter R_o will increase the value of (1-S) (according to Section 2.8), hence the starting point of the data points is shifted. The trajectory remained constant in Figure 4.20 since L remained constant.

It is noteworthy that the starting point in the L axis of the L parameter of the model signals, will be dictated by the signals' amplitudes and in the (1-S) axis by the offset level.

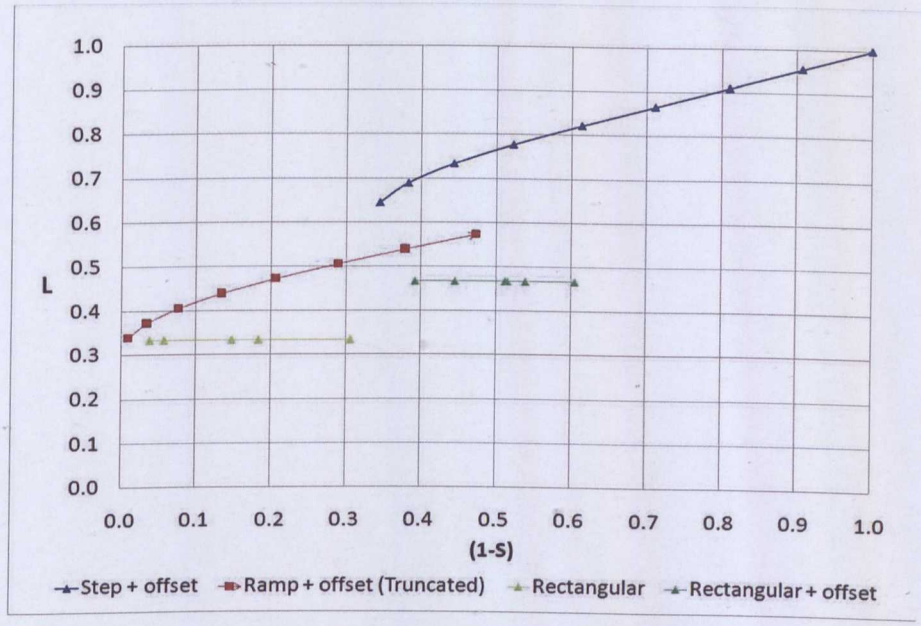

FIGURE 4.20: L versus (1-S) diagram for combined model signals. The gradient L/(1-S) = effective amplitude per unit width

For the truncated ramp (ramp + offset) , in Figure 4.20, L increased approximately linearly with the signal spread since the ramp expanded across the active region within the quarter cycle (beyond the middle).

For the step function, the starting point of the data points shifted from origin for the no offset case (Figure 4.19(a)) to (0.34, 0.64) with an offset of 0.2 (Figure 4.20), The L increase was approximately linearly proportional to the signal spread. When an offset was added to the step, an initial value of (1-S) was introduced, which created a gradual decrease of (1-S) as the signal extended beyond the middle of the quarter cycle.

4.8 Summary

An overview of the chromatic method used to analyse the PD data has been presented. The first stage of the analysis is the pre-processing of the raw data.

The chromatic processing of the data using tristimulus R,G,B processors produces the outputs R_o, G_o, B_o from which x, y, z and H, L, (1-S) parameters are derived.

Various chromatic diagrams can be generated from the chromatic parameters. These are Cartesian diagrams showing the variation of x, y, z, polar diagrams showing H, L, (1-S) or a combination of parameters from each of these two group. Examples of such diagrams have been presented and their implications explained.

Model signals, simulating real PD signals, have been selected and chromatically processed. Their resulting chromatic diagrams have been presented and serve as templates for consideration of real PD signals.

The following diagrams are of particular value for the purpose this research:

1. $z : y$ Cartesian diagram indicating the proportion of the signal in the first half of the quarter cycle from the 90^o limit. It enables the spread of the PD activity across the quarter cycle to relatively lower levels of the AC voltage to be obtained.

2. L/(1-S) : z Cartesian diagram indicating how the effective amplitude (taking account of the spread of the signal) varies as the signal progressively spreads across the quarter cycle. As such, it is a normalised indication of how the severity of the PD activity changes.

Chapter 5

Discussion of Results

5.1 Introduction

Chromatic analysis techniques have been described in Section 2.8. The outputs from such analysis are in the form of three parameters, R_o, G_o, B_o, which can be transformed into two main sets of other characterising parameters, x, y, z and H, L and (1-S). Various diagrams were introduced in Section 4.4 relating these parameters to each other, depending on the required signal features.

This Chapter presents the results of the chromatic processing of real test data for two purposes. The first relates to differentiating between PD data generated by different types of PD sources. The second relates to PD signals progressing -in time or with increasing voltage- towards full electrical breakdown. Both data sets were generated under controlled laboratory conditions and have already been presented in Chapter 3.

The resulting x, y, z and H, L, (1-S) parameters have been plotted in key diagrams of the form introduced in Chapter 4. The diagrams have then been analysed for various features and information about progression towards breakdown and for differentiating signals produced by different forms of PDs.

It has been established in Chapter 4 that $z : y$ diagrams provide an indication about the dominant phase angle, in that, they show the relationship between the highly active part of the signal (under the B processor) with regard the whole signal (covered by the G processor). The overlap of G and B processors will

increase the sensitivity of the filter and locate the center of gravity of the signal, referred to by the dominant phase angle, since the domain parameter of the signal is phase angles.

In an attempt to use this property to distinguish between PD signals depending on their generating sources, the two sets of data were chromatically processed and their $z_1 : y_1$ and $z_3 : y_3$ were plotted. The choice of the 1^{st} and 3^{rd} quarter cycles for discussion was based on the knowledge that high PD activity is mostly encountered during the rise of the applied voltage sinewave in both directions. Any sudden change in PD activity occurrence will appear in these regions first.

5.2 *xyz* Diagrams

In this section results displayed on x, y, z characteristic diagrams (Chapter 4, Section 4.5.2) are considered.

5.2.1 PD signals from different sources

The PD signals from different sources were:

1. Those by Hao *et al* [7], consisting of signals from 4 different PD sources (referred to in the diagrams as *Internal*, *Surface*, *Floating* and *Corona*) at different applied voltages (6.9 kV to 25 kV). (Section 3.2 Chapter 3).

2. Those by Ariastina *et al* [4], consisting of PD signals from a PD source, at 2 different applied voltages, where the dielectric (oil) used and cavity shape were changed simultaneously. (Section 3.2 Chapter 3). This PD source is referred to in the diagrams as *Indo1*.

The results have been analysed using the techniques described in Chapter 3 to produce data displayed upon chromatic $z : y$ and L/(1-S) : z diagrams (Figure 4.4(b) and Figure 4.9(b) in Chapter 4).

These results may then be compared with those obtained from the model signals considered in Section 4.6 of Chapter 4.

5.2.1.1 Processed results

Figures 5.1 (a) and (b) show analysis of the experimental data of Figures 3.6 to 3.11, Section 3.4, Chapter 3 for *Internal*, *Surface*, *Floating Corona* and *Indo1*, during the 1^{st} and 3^{rd} quarter cycles respectively of an AC waveform displayed upon $z : y$ diagrams for the first and third quarter cycles respectively (i.e. AC voltage increasing in both directions).

The results show the following features:

- *Corona* : Data points lying on and close to the (0.33, 0.33) point, at (0.4 , 0.14) and (0.38 , 0.41) for both 1^{st} and 3^{rd} quarter cycles respectively.
- *Floating*: Data points lying close the the (0.33 , 0.33) point and around the (0.35 , 0.5) point in both quarter cycles.
- *Internal*: Data points lying further from the (0.33 , 0.33) point.
- *Surface* : Data points lying around (0.25 , 0.6) during the 1^{st} quarter cycle and around (0.33 , 0.45) during the 3^{rd}.
- *Indo1* : The first two points (15 kV) lying on the z + y = 1 line and the last two points (18 kV) tending towards the (0.33 , 0.33) point in both quarter cycles.

The loci of the data representing points in the $z : y$ diagrams can be used to extract meaningful information from clear trends, in terms of points clustering or visible progression towards a certain locus (e.g. the (0.33 , 0.33) point).

It is apparent in Figure 5.1 (a) and (b) that the data points are scattered around the (0.33 , 0.33) point. However, the points representing data from the same PD sources are clustered together. This characteristic can be used as a means for distinguishing between various PD sources and assigning PD signals to categories depending on their generating sources. The same task was acheived by various methods in Chapter 2, however this time with a simpler method which is more informative and traceable.

Also shown on Figure 5.1 (a) and (b) are three color coded areas indicating nominal areas close to breakdown (i.e (0.33 , 0.33)) in Red with high PD activity,

medium PD activity areas in Orange and low PD activity areas in Green. An information which is not provided in the same explicit manner by the other methods in Chapter 2, in that, the progress of the PD activity can be easily traced as it moves between the 3 different areas.

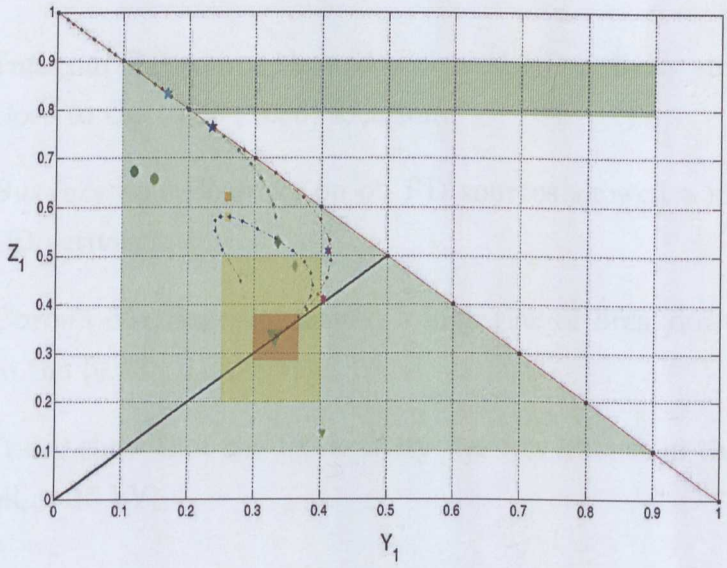

(a) 1^{st} Quarter cycle

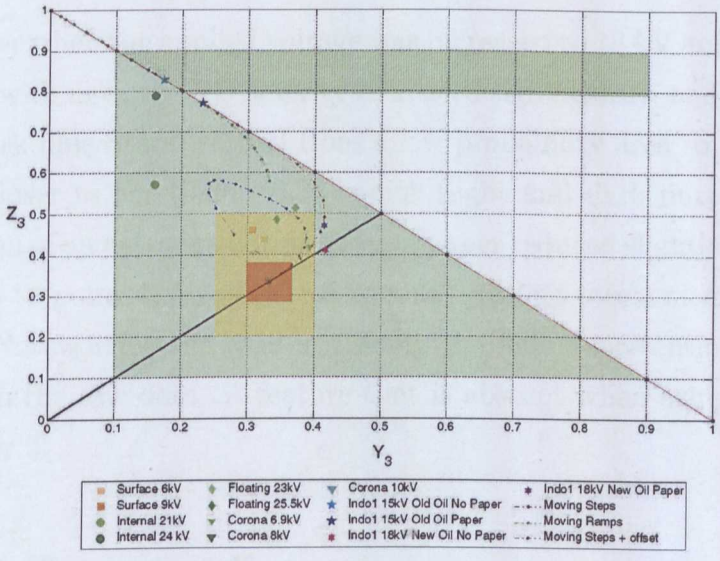

(b) 3^{rd} Quarter cycle

FIGURE 5.1: $z : y$ characteristics of data from different PD sources at various times/voltages.

5.2.1.2 Features of processed data

The results for the various types of PD may be interpreted as follows:

- *Internal* PD source showed a normal PD activity since the points are not close to the (0.33 , 0.33) location.
- *Surface* and *Floating* on oil PD sources showed a more extensive level of PD activity.
- *Corona* discharges presented a high risk of breakdown since they are close to the (0.33 , 0.33) point.
- *Indo1* show that the PD activity was not intense in the sample using an old oil at 15 kV.

The insertion of an insulation layer of paper (Figure 3.2 (b)), increased the PD activity but not to a great extent (the light and dark blue stars in Figure 5.1 (a) and (b) along the $z + y = 1$ line).

However when the applied voltage was increased to 18 kV and despite replacing the old oil with new, the PD activity increased significantly, and the data points (light and dark blue Stars) shifted from a low probability area to a medium probability area, closer to the (0.33 , 0.33) point (light and dark purple David-Stars). The insertion of an extra insulation layer of paper reduced slightly the PD activity, from point 3 to point 4, possibly due to a self healing mechanism within the dielectric (oil). Noteworthy, the ease in tracing the data representing points and relating them to the raw data. A feature that is abscent when using other methods from Chapter 2.

5.2.1.3 Symmetry effects

PD signals have always been recorded initially as voltage or current pulses and then converted into q pulses for further analysis. The PD pulse shape has always been the prime feature for PD signal discrimination [4] [7] [8] [22].

None of the researchers above nor others have considered, when doing the PD signal shape analysis, studying the PD pulse symmetry with regard a vertical

axis, neither at half nor quarter nor at any imaginary point along the phase angle axis, to use it as an extra tool for PD signal discrimination. A credit given to chromaticity.

The chromatic analysis assigns characterising parameters to each part covered by the R, G, B processors e.g. quarter cycles in this case. This will allow the comparison between various chromatic parameters of various quarter cycles to further discriminate between PD pulses.

Hence, one of the features of the PD signal that can be used for further discrimination by comparing between xyz chromatic parameters is the degree of signal symmetry between the two adjacent quarter cycles of a half cycle, e.g. by comparing z_1 with x_2 (first and second quarter cycles) and z_3 with x_4 (third and fourth quarter cycles) (Figure 4.5(a)).

To highlight the degree of symmetry, z_1 is shown as a function of x_2 in Figure 5.2(a), and z_3 versus x_4 in Figure 5.2(b). Totally symmetrical signals would lie on the locus $x = z$. Inspection of Figure 5.2 (a) and (b) shows that the data points seem to be clustered in groups depending on the PD source type and scattered around the symmetry line ($x = z$).

The symmetry of the data from different sources is as follows:

(a) *Indo1* data: the PD activity point for 15 kV is located during the first half cycle at (0.75 , 0.83) (Figure 5.2(a)) indicating a fair degree of symmetry. For the second half cycle, the point location is (0.78 , 0.82) (Figure 5.2(b)) also showing a fair degree of symmetry.

When the applied voltage increased to 18 kV and the new oil introduced, the data points coordinates are (0.75 , 0.4) (Figure 5.2(a)) for the first half cycle and (0.76 , 0.4) for the second half cycle (Figure 5.2(b)). This implies a shift of the signal envelope towards the second quarter cycle in both cases compared with the 15 kV results.

A similar shift in signal symmetry is apparent when insulation paper is introduced. At 15 kV without paper, the data points are (0.85 , 0.77) (first half cycle Figure 5.2(a)) and (0.8 , 0.38) (Figure 5.2(b)). At 18 kV, the data points are (0.8 , 0.5) and (0.79 , 0.78) for the first and second half cycles respectively.

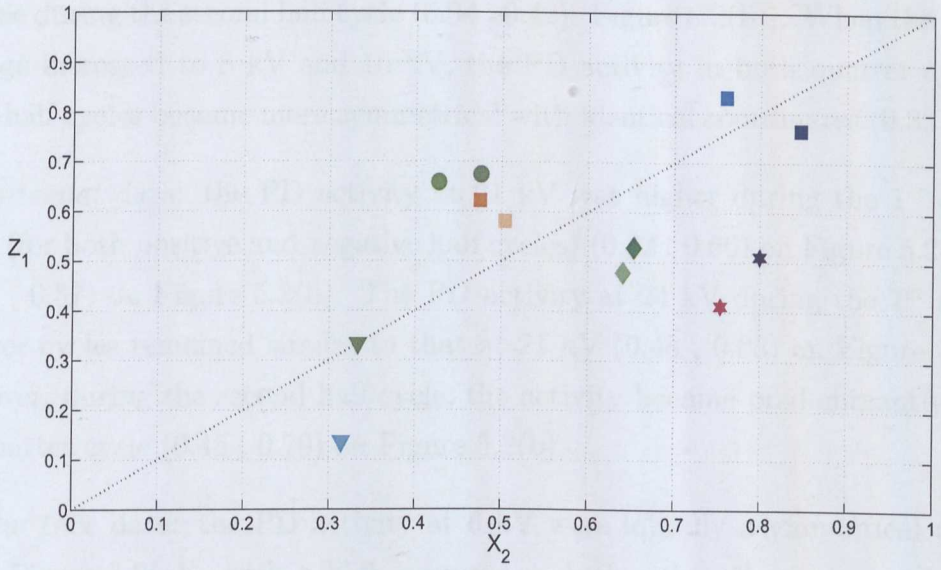

(a) 1^{st} half cycle

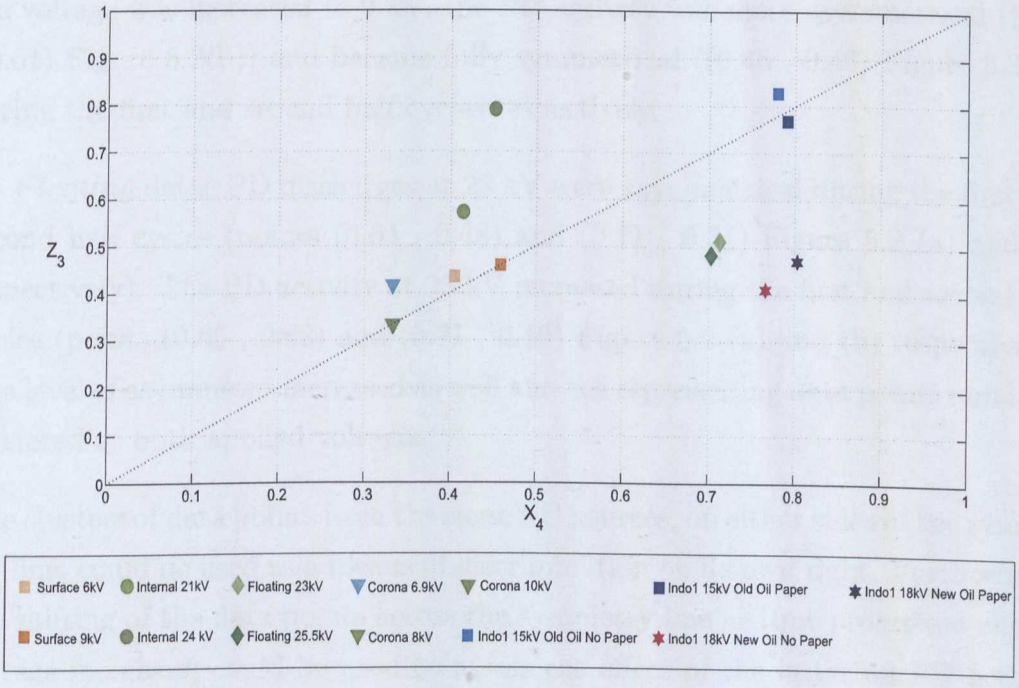

(b) 2^{nd} half cycle

FIGURE 5.2: z_a : x_b characteristics for identifying symmetry features of PD signals.

(b) *Corona* data: the corona discharges at 6.9 kV showed an asymmetry during

the first half cycle towards the 2^{nd} quarter cycle (0.3 , 0.1) (Figure 5.2(a)) but the reverse during the second half cycle (0.34 , 0.42) (Figure 5.2(b)). When the applied voltage increased to 8 kV and 10 kV, the PD activity in both quarter cycles of both half cycles became more symmetrical with identical coordinates (0.33 , 0.33).

(c) *Internal* data: the PD activity at 21 kV was higher during the 1^{st} quarter cycle (for both positive and negative half cycles) (0.42 , 0.66) on Figure 5.2(a) and (0.42 , 0.57) on Figure 5.2(b). The PD activity at 24 kV during the 1^{st} and 3^{rd} quarter cycles remained similar to that at 21 kV (0.48 , 0.68) on Figure 5.2(a) . However, during the second half cycle, the activity became predominantly in the 1^{st} quarter cycle (0.45 , 0.79) on Figure 5.2(b).

(d) *Surface* data: the PD activity at 6 kV were initially asymmetrical ((0.51 , 0.59) Figure 5.2(a)), with a high occurrence during the 1^{st} quarter cycle, compared to the 2^{nd} quarter cycle of the first half cycle. They ended being close to symmetrical during the second quarter cycle ((0.41 , 0.43) Figure 5.2(b)). When the voltage was increased to 9 kV, the PD activity was more asymmetrical ((0.48 , 0.61) Figure 5.2(b)) and became fully symmetrical ((0.46 , 0.46) Figure 5.2(b)) during the first and second half cycles respectively.

(e) *Floating* data: PD discharges at 23 kV were asymmetrical during the first and second half cycles (points (0.64 , 0.48) and (0.71 , 0.51) Figure 5.2 (a) and (b) respectively). The PD activity at 25 kV increased during the first and second half cycles (points (0.65 , 0.62) and (0.71 , 0.49) Figure 5.2 (a) and (b) respectively). The level of asymmetry increased as well and the representing data points remained clustered at both applied voltages.

The clusters of data points from the same PD sources, on either sides of the symmetry line, could be used as a means of discrimination on its own right. Furthermore, the shifting of the data points across the symmetry line as time progresses and/or voltage increases, could be used to assess the effect of the latter on PD activity and PD signal shapes. Again, this feature was overlooked by the various methods talked about in Chapter 2.

5.2.1.4 Polarity effect

Another feature of the PD signal, which was also overlooked by researchers and can be used for further discrimination by comparing between xyz chromatic parameters is the the effect of the applied voltage polarity on PD activity, which can be extracted by plotting the chromatic parameters (z_1) of the 1^{st} quarter cycle against those (z_3) of the 3^{rd} quarter cycle and the parameters (z_2) of the 2^{nd} quarter cycle against the 4^{th} (z_4). Such graphs are given on Figure 5.3 (a) and (b).

(a) *Indo1* data: at both applied voltages (15 and 18 kV) and in both environments (different oils and insulation papers), the change of polarity of the applied voltage sinewave had no impact on the PD activity occurrence in both half cycles (points (0.83 , 0.83), (0.78 , 0.78) and (0.41 , 0.41) Figure 5.3(a)). A slight effect during the 1^{st} QC at 18 kV in new oil with extra insulating paper occurred ((0.48 , 0.51) Figure 5.3(a)). During the fall of the applied sinewave in both half cycles, no PD activity was recorded (Figure 5.3(b)).

(b) *Corona* data: the PD activity was highly influenced by the polarity change at 6.9 kV applied voltage (points (0.42 , 0.14) and (0.34 , 0.39) Figure 5.3 (a) and (b) respectively). However, as the applied voltage increased to 8 and 10 kV, the amount of PD activity occurred in all quarter cycles was the same and the polarity of the applied voltage had no effect (point (0.33 , 0.33) Figure 5.3 (a) and (b) respectively).

(c) *Surface* data: at 6 kV, during the first half cycle, the effect of the positive rise of the sinewave (point (0.44 , 0.58) Figure 5.3(a)) on PD activity was higher, whilst during the second half cycle, the negative fall had the greater effect (point (0.24 , 0.14) Figure 5.3(b)). At 9 kV, the effect of polarity increased (point (0.46 , 0.62) Figure 5.3(a)) during the first half cycle, and had less effect during the second half cycle (point (0.16 , 0.14) Figure 5.3(b)).

(d) *Internal* data: at 21 kV, the PD activity was higher during the positive rise of the sinewave (point (0.58 , 0.68) on Figure 5.3(a)), the fall of the sinewave had little effect (point (0.21 , 0.19) on Figure 5.3(b)). At 24 kV, the effect of the rise of the sinewave in the negative direction was higher on the PD activity (point (0.79 , 0.68) on Figure 5.3(a)), whilst the fall of the sinewave in both directions had no effect on the PD activity (point (0.14 , 0.14) on Figure 5.3(b))

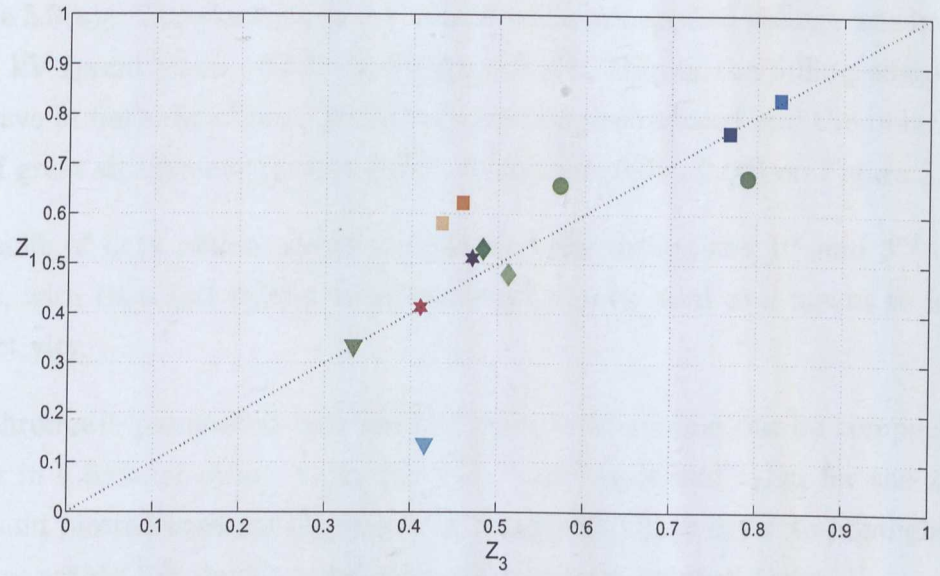

(a) 1^{st} / 3^{rd} quarter cycles

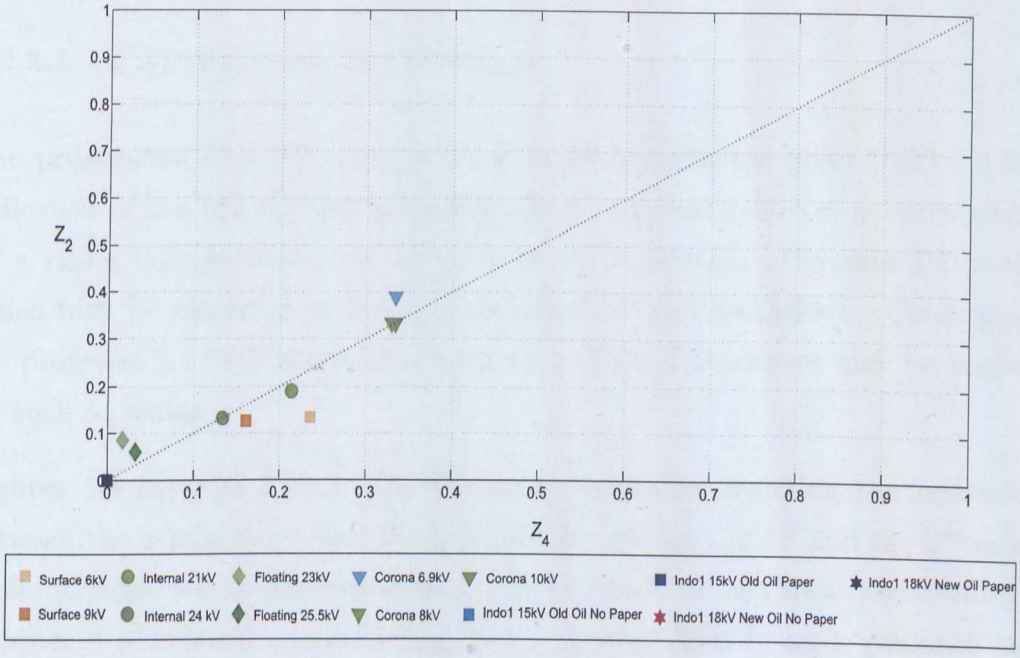

(b) 2^{nd} / 4^{th} quarter cycles

FIGURE 5.3: z_a : z_c characteristics for identifying the polarity effect on PD activity.

(e) *Floating* data: the In the floating on oil PD sources, the effect of the negative rise of the applied voltage at 23 kV on the PD activity occurrence was

slightly higher than the effect of the positive rising edge (point (0.52 , 0.48) on Figure 5.3(a)). The situation was reversed when the applied voltage was increased to 25 kV (point (0.48 , 0.52) on Figure 5.3(a)). During the falling edges of the sinewave in both directions, the PD occurrence was reduced and the polarity was not of great significance (points (0.02 , 0.08) and (0.04 , 0.06) on Figure 5.3(b)).

The shift of data points across the polarity line during the 1^{st} and 3^{rd} quarter cycles, with time and volatge increase, could also be used as a means to monitor PD activity.

The chromatic parameters representing each quarter cycle can be compacted together in a form of ratios, z_1/x_2 for the 1^{st} half cycle and z_3/x_4 for the 2^{nd} half cycle and plotted together (Figures C.1, Appendix C), in order to highlight other features within PD signals and further discriminate between them.

5.2.2 Progression in time towards Breakdown

5.2.2.1 $z : y$ diagrams indications

The progression of a PD along a $z : y$ locus towards the point (0.33 , 0.33) is indicative of the PD activity spreading along a quarter cycle i.e. occurring earlier on a rising voltage wave. As such, it is one indication of greater PD activity which may be expected in the approach towards full breakdown. Consequently, the progression of PD discharges from each of the PD sources may be inspected for such a change.

Figures 5.4 (a) and (b) are the Cartesian diagrams depicting the relationship between the z parameter and the y parameter during the 1^{st} and the 3^{rd} quarter cycles of three sets of processed data. The processed model signals of Section 4.6, Chapter 4 are shown on these diagrams as dotted lines being a guidance of the extent to which a signal may be progressing towards full breakdown.

The data sets considered are those listed in Chapter 3. These are:

1. PD signals from an air cavity created between 2 sandwiched pressboard pieces (Figure 3.3) [4] immersed in medium and highly contaminated oils and tested at different voltage levels (Section 3.2, Chapter 3). This data is referred to in the diagrams as *Indo2* and *Indo3* respectively.

2. PD signals from a needle plane geometry created within a XLPE used cable slab (Figure 3.5) [22] and tested at various voltages (Section 3.2, Chapter 3). This data is referred to in the diagrams as *Italy* data.

3. PD signals from a needle-plane geometry made within an epoxy resin filled cubic container [8] (Figure 3.4) and tested at various voltages (Section 3.2, Chapter 3). This data is referred to in the diagram as *Australia* data.

Also shown on Figure 5.4 (a) and (b) are corresponding to *normal* PD activity in *green* , *moderate* PD activity in *orange* and *high* PD activity in *red* (just before breakdown JBD).

Visual inspection of Figures 5.4 (a) and (b) indicates that the loci of the data points from various sets in both diagrams are similar. This indicates that there is no major influence of voltage polarity of the sinewave on the PD activity.

(a) *Indo*2 and *Indo*3 data: The PD activity was confined to phase voltages of the 1^{st} and 3^{rd} quarter cycles (z coordinates high, y low Figure 5.4). The data points are displaced along the locus $x + y = 1$ following a step function / ramp points trend (Figure 4.15 (b) and (c)) as the applied voltage increased in both cases. The implication is that all these conditions are far removed from full breakdown.

(b) *Italy* data: The data points are located in the medium risk area for both quarter cycles (Figure 5.4 (a) and (b)). As the voltage increased, the data points are displaced closer to the (0.33 , 0.33) point, which is an indication of progression towards breakdown. The final point just before breakdown has coordinates (0.33 , 0.39) for the first half cycle.

(c) *Australia* data: The data points at 31 and 18 minutes before breakdown lie on the $x + y = 1$ locus for both quarter cycles (Figure 5.4 (a) and (b)) implying that they are far removed from breakdown. However the 18 minutes data are displaced towards the (0.33 , 0.33) point being consistent with a ramp/step function about to fill the quarter cycle (Figures 4.10 (b) and (c)). Thereafter, the third data point (JBD) shifted off the $x + y = 1$ locus to (0.28 , 0.68) which indicates a change in the signal form to a pulse shape (Figure 3.12(c)). The insulation was compromised at this stage. Although the coordinates of this point are well displaced from the breakdown point of (0.33 , 0.33), breakdown occurred thereafter. This indicates that the insulation was compromised well before the data was recorded and visuali

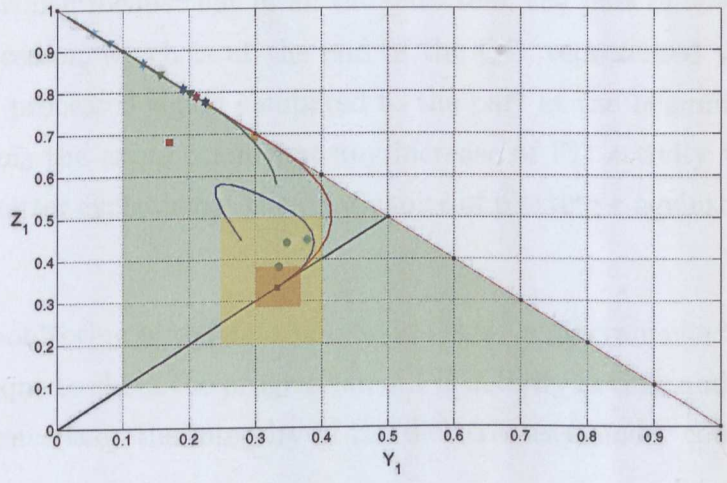

(a) 1^{st} quarter cycle

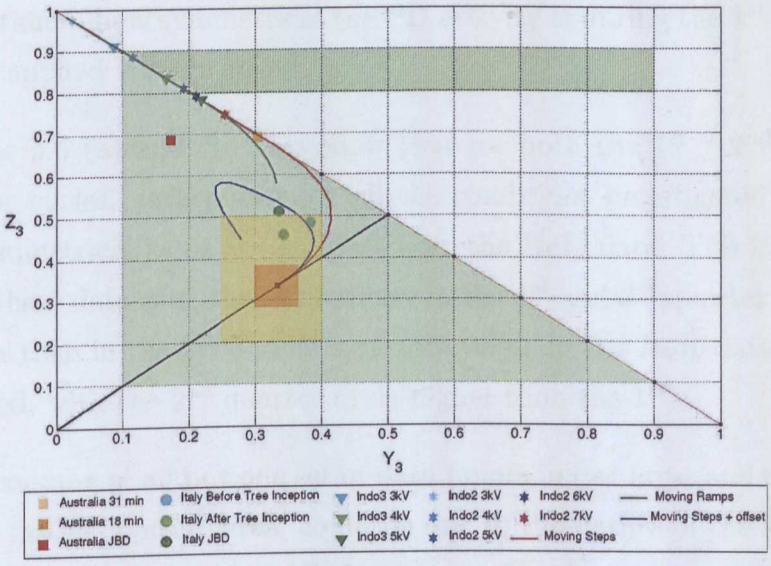

(b) 3^{rd} quarter cycle

FIGURE 5.4: Progression of PD activity with time.

inspected and/or that the location of a $z : y$ diagram alone is not a sufficient criterion for indicating imminent breakdown.

Noteworthy, the $z : y$ points in both QCs did not increase beyond $z < 0.33$ and

$y > 0.50$ (i.e the area limited by the y-axis, the $z = y = 1$ line and $z + y = 1$ line), which means that in all the data sets, the part of the signal covered by the B processor, which is at the end of the QC, represented the highest proportion of the processed signal compared to the part at the beginning of the signal. This confirms the assumption that any increase of PD activity will be in that part of the quarter cycle, hence the right choice of plotting z against y instead of x against y.

The monitoring of the data points on the $z : y$ diagram can be used as a predictive technique to check the progression of PD activity in time and with voltage increase, and hence keep the integrity of the dielctric used under constant supervision.

5.2.2.2 Symmetry effect

Figures 5.5 (a) and (b) show the data points representing the various data sets in terms of the relationships $z_1 : x_2$ and $z_3 : x_4$ respectively. This can be used as an indication of how symmetrical the PD activity is during the 1^{st} and 2^{nd} half cycles of the applied voltage sinewave.

Figures 5.5 (a) and (b) also show that for both the 1^{st} / 2^{nd} and the 3^{rd} / 4^{th} quarter cycles, data points for all the conditions investigated are located above the symmetrical locus $z = y$, apart from the *Italy* data. This is an indication that in all these data sets, the PD activity in the 1^{st} and 3^{rd} quarter cycles were always greater than in the 2^{nd} and 4^{th} quarter cycles. In the *Italy* data, the situation was reversed, with the 2^{nd} quarter cycle higher than the 1^{st}.

The grouping of all but one set of data points in one area, and only the *Italy* data points in the opposite area, could be due to the nature of the specimens in which the tests were performed. All the data analysed were from laboratory specimens except the *Italy* data, which were with a section of a real HV cable, which had been in service for many years and was used to form a needle-plane geometry (Section 3.15, Chapter 3).

Also, the grouping of the *Indo*2, *Indo*3, *Australia* and *Italy* data representing points' independently from each other can be used to discriminate between the types of geometries producing PD activity. This also confirms the conclusions drwan in Section 5.2.1.3.

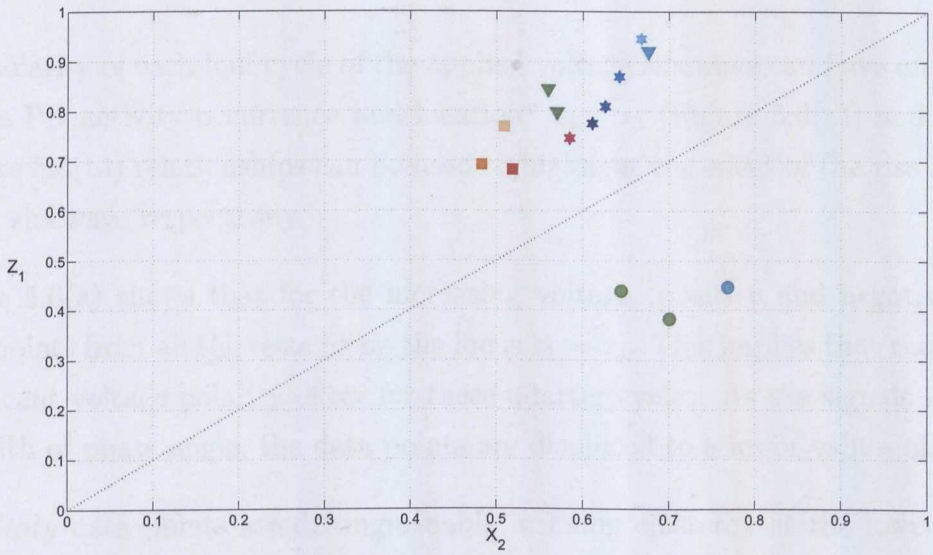

(a) 1^{st} half cycle

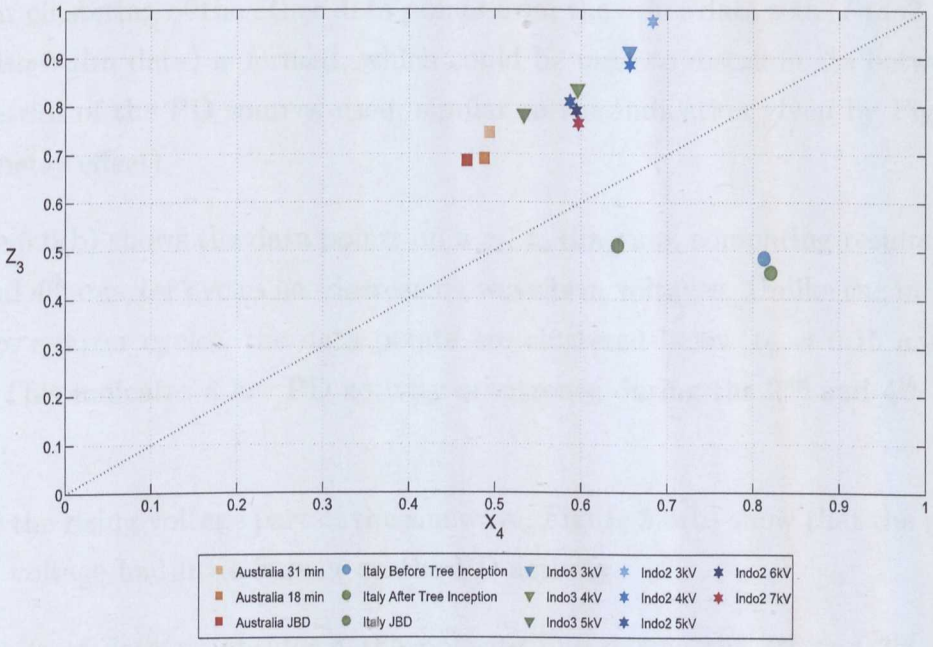

(b) 2^{nd} half cycle

FIGURE 5.5: $z_a : x_b$ characteristics for identifying the symmetry features of PD signals.

5.2.2.3 Polarity effects

The polarity of each half cycle of the applied voltage sinewave can have an impact on the PD activity occurrence and location. $z_1 : z_3$ (Figure 5.6(a)) and $z_2 : z_4$ (Figure 5.6(b)) relationships can be used to highlight the effect of the rise and fall of the sinewave respectively.

Figure 5.6(a) shows that for the increasing voltage (positive and negative), the data points from all the tests lie on the locus $z_1 = z_3$. This implies that there is no significant voltage polarity effect for these quarter cycles. As the signals increase in width of phase angle, the data points are displaced to a lower values of z_1, z_3.

The *Italy* data points are distinguishable in being clustered at the lower values of z_1, z_3 (0.4 , 0.5) implying signals extending over more than half the quarter cycle phase angle. In addition, the point just before breakdown has a predominant effect during the first positive voltage cycle.

A clear clustering of the other data points from the other data sets (*Indo*2, *Indo*3, and *Australia* data) is formed, which could be used to discriminate between the geometries of the PD sources used, similar to the indication given by Figure 5.5 (symmetry effect).

Figure 5.6(b) shows the data points on a z_2, z_4 diagram, comparing results for the 2^{nd} and 4^{th} quarter cycles i.e. decreasing waveform voltages. Unlike the increasing voltage quarter cycles, the data points are clustered below $z_2 = 0.15$ and $Z_4 = 0.15$. This indicates a low PD activity occurrence during the 2^{nd} and 4^{th} quarter cycles.

As for the rising voltage part of the sinewave, Figure 5.5(b) show that the polarity of the voltage had little impact on the PD activity.

The shift of data points down the polarity line during the 1^{st} and 3^{rd} quarter cycles, with time and volatge increase, could also be used as a predictive means to monitor PD activity towards breakdown.

Other features within PD signals can be highlighted by compacting the chromatic parameters representing each quarter cycle in a form of ratios, z_1/x_2 for the 1^{st} half cycle and z_3/x_4 for the 2^{nd} half cycle and plotting them together (Figures C.1, Appendix C).

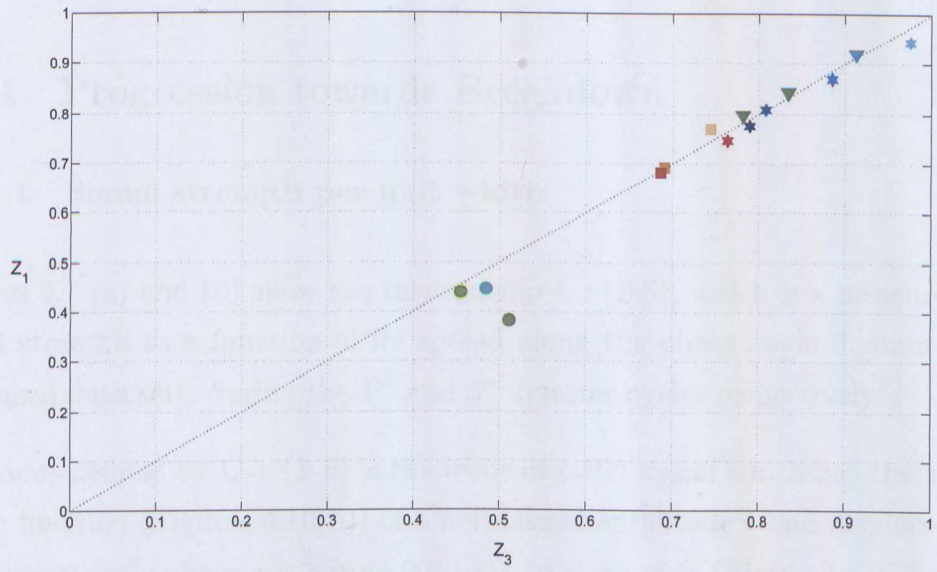

(a) 1^{st} / 3^{rd} quarter cycles

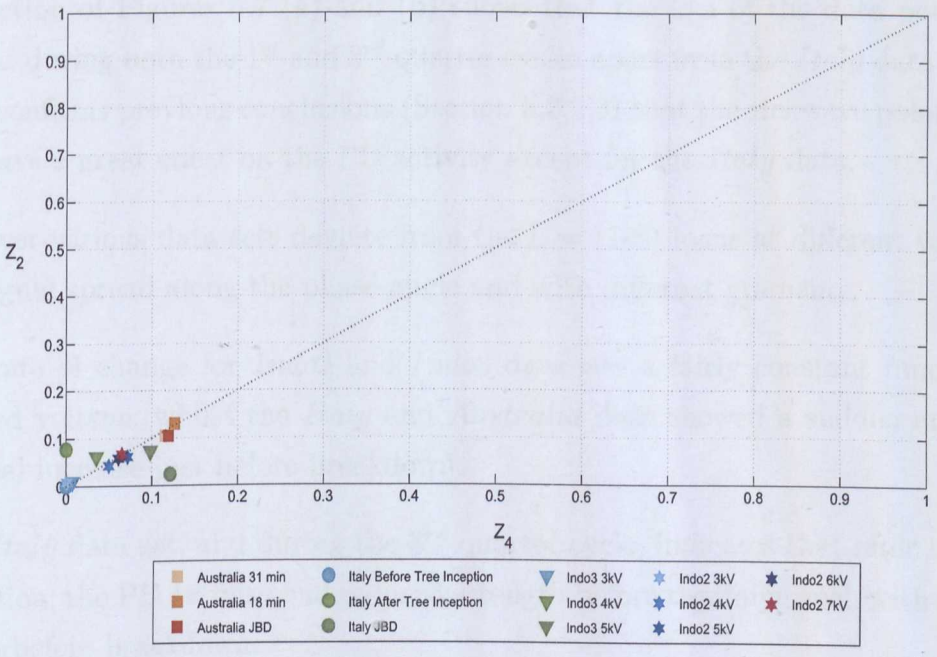

(b) 2^{nd} / 4^{th} quarter cycles

FIGURE 5.6: $z_a : x_c$ characteristics identifying the polarity effect on PD activity.

5.3 L, (1-S) Diagrams

5.3.1 Progression towards Breakdown

5.3.1.1 Signal strength per unit width

Figures 5.7 (a) and (b) show the relationship L : (1-S), which is a measure of the signal strength as a function of its spread along the phase angle domain for the processed data sets, during the 1^{st} and 3^{rd} quarter cycles respectively[1].

The locus defined by L = (1-S) is the locus of a PD signal which has the shape of a step function (Figures 4.10(b)) of a normalised amplitude 1 and displaced along the quarter cycle phase angle from 90^o to 0^o in steps of 5^o (Figure 4.8, Chapter 4). It has been chosen to serve as a template of a model PD signal in which the signal strength L is linearly proportional to its spread (1-S).

Inspection of Figures 5.7 (a) and (b) shows that the loci of the data points are similar during both the 1^{st} and 3^{rd} quarter cycles apart from the *Italy* data points. This confirms previous conclusions (Section 5.2.2.3) that the sinewave polarity did not have a great effect on the PD activity except for the *Italy* data.

However various data sets deviate from the L = (1-S) locus at different values of the signal spread along the phase angle and with different gradients.

The rate of change for *Indo2* and *Indo3* data was a fairly constant function of applied voltage, whilst the *Italy* and *Australia* data showed a sudden and substantial increase just before breakdown.

The *Italy* data set, and during the 3^{rd} quarter cycle, indicates that after the tree inception, the PD activity had reduced strength before regaining such with shorter width before breakdown.

The progression of the data points above the step function line, i.e. the increase of signal strength with its width, during the 1^{st} and 3^{rd} quarter cycles, with time and volatge increase, can be used as a predictive means to monitor PD activity and assess the dielectric integrety.

[1]The data points have been normalised with respect to the first data point in each case being on the step function characteristic. The remaining points were scaled accordingly.

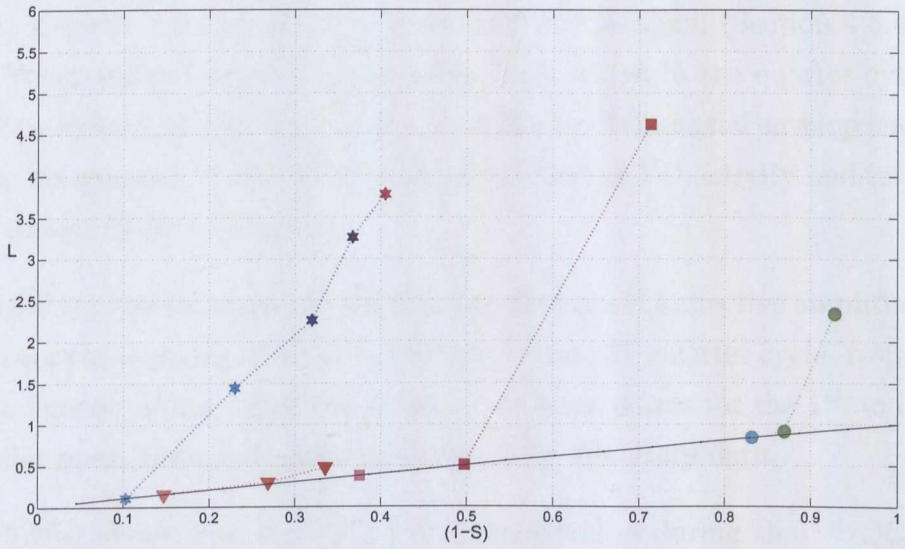

(a) 1^{st} quarter cycle.

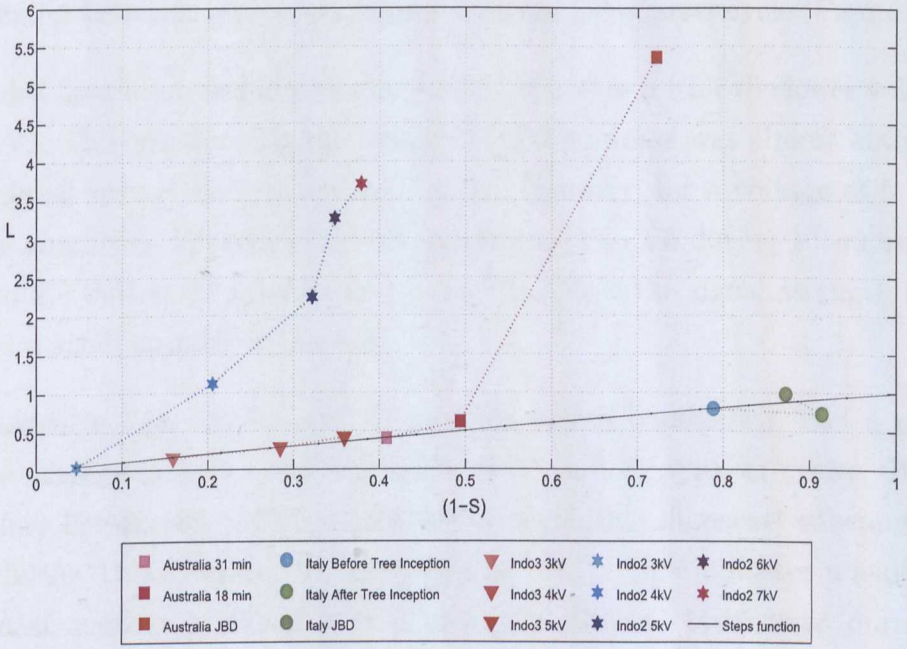

(b) 3^{rd} quarter cycle

FIGURE 5.7: Signal strength per unit width.

5.3.1.2 Effective amplitude measure

It has been indicated that the measurement of a signal strength per unit width (spread) L/(1-S) gives an effective amplitude of the signal (Section 4.5.4, Chapter 4). When plotted against z, this gives the location in the quarter cycle (part under B processor) of dominant amplitude location of the signal envelop and should show the progression of the effective amplitude of the PD activity and its concentration along the phase domain.

Figures 5.8 (a) and (b) show the relationship between the effective amplitude L/(1-S) and z for the 3 processed data sets for the 1^{st} and 3^{rd} quarter cycles respectively. The two figures indicate that the trend of the data points for the 1^{st} and 3^{rd} QC are similar apart from some small differences for the *Italy* data.

Figure 5.8(a) shows that the L/(1-S) : z relationship during the 1^{st} QC for the *Indo*2 data progressed rapidly to higher L/(1-S) levels within a short span of z. This indicates that as the signal spreads across the quarter cycle its effective amplitude per unit width also increases by almost an order of magnitude of (1 - 9.9). Similar behavior is also apparent during the 3^{rd} quarter cycle (Figure 5.8(b)).

The *Indo*3 data remained close to the locus L/(1-S) = 0.1 for the lower voltages (3 kV, 4 kV). This implies that the signal strength increase was almost entirely due to the signal spread at constant amplitude. However, for a voltage of 5 kV, the effective amplitude L/(1-S) increased somewhat (1 to 1.5 during 1^{st} quarter cycle and 1 to 2.2 during 3^{rd} quarter cycle) implying that the signal strength increase involved a small amplitude increase.

The *Australia* data, at 31 and 18 minutes before breakdown, had a constant effective amplitude $L/(1-S) \simeq 1$ for both 1^{st} and 3^{rd} quarter cycles. However, just before breakdown (JBD), the effective amplitude increased substantially (1 to 6.5 during 1^{st} QC and 1 to 7.3 during 3^{rd} QC). This indicates a sudden and substantial increase in effective amplitude just prior to breakdown during both quarter cycles.

With the *Italy* data, the effective amplitudes before and after tree inception were both of constant effective amplitude ($L/(1-S) \simeq 1$) for both quarter cycles. However just before breakdown, the effective amplitude during the 1^{st} quarter cycle increased from 1 to 2.5 and the z value tended to 0.33. During the 3^{rd}

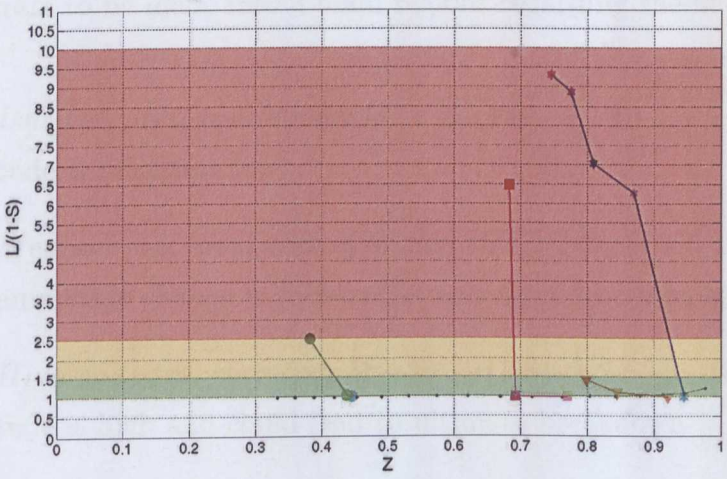

(a) 1^{st} quarter cycle

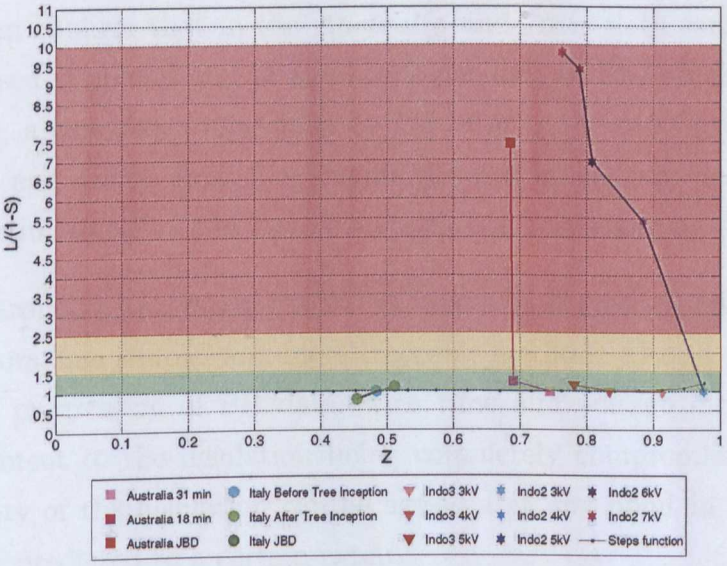

(b) 3^{rd} quarter cycle

FIGURE 5.8: The effective amplitude of PD signals.

quarter cycle such an increase in effective amplitude did not occur and the signal spread reduced ($z = 0.5$ to 0.45).

This analysis with experimental data allows an empirical division of the L/(1-S) : z diagram to be made into 3 main regions regarding the likelihood of breakdown.

1. *Low* risk area, corresponding to L/(1-S) = 1 to 1.5, i.e. the effective amplitude is relatively low.

2. *Medium* risk area, corresponding to L/(1-S) = 1.5 to 2.5, i.e the effective amplitude change is substantial and should be monitored closely.

3. *High* risk area, corresponding to L/(1-S) > 2.5, i.e. the effective PD amplitude is high and could lead to ultimate breakdown.

Of course, the limits of the *low*, *medium* and *high* risk bands are specific for the processed PD data, with the prior knowledge of *Australia* and *Italy* samples outcomes. They could be reset as more empirical data becomes available.

Taking the indications of the representing data points from Figures 5.4 and 5.8, one can confirm that in the *Australia* and *Italy* data samples, the PD activity increased in spread and in amplitude per unit width, which led to the insulation failure, a conclusion confirmed by Lai *et al* in [8] and Cavallini *et al* in [22]. In *Indo*2 and *Indo*3 data, the sample did not breakdown despite the high rate of change in L/(1-S) : z in *Indo*3, a conclusion confirmed by Ariastina *et al* in [4].

The chromatic analysis of the PD data sets confirmed the results obtained by their initiators, in a simpler and more traceable method. Also, it allowed the inspection of the progression of PD data, with time and voltage incease, from a PD free enviroment to the insulation being completely compromised. Furthermore, the integrity of the insulation can be assessed at any point in time and its life span can be predicted to a certain extent.

The results shown on Figures 5.4 (a) and (b) for L/(1-S) : z and on Figure 5.8 for $z : y$ are summarised on Table 5.1:

TABLE 5.1: Summary of processed PD activity data indicating the location of various data in Low, Medium or High possibility breakdown regions

Parameter	Activity spread $z : y$		Effective Amplitude L/(1-S) vs. z			
Quarter Cycle	1^{st} QC Figure 5.4(a)	3^{rd} QC Figure 5.4(b)	1^{st} QC Figure 5.8(a)	3^{rd} QC Figure 5.8(b)		
PD data set	Loci of data	Loci of data	Loci of data	Loci of data	Comments	Observation
Australia	Low+High	Medium+High	Low+High	Low+High	BD[1]	Insulation Compromised
Italy	Medium+High	Medium+high	Low+high	Low+ Below normalised line	BD[2]	Insulation Compromised
Indo3	Low	Low	Low+Medium	Low	NBD[3]	Check L/(1-S)
Indo2	Low	Low	Low+High	Low+High	NBD[4]	Check L/(1-S)

[1] Sample Broke down Lai *et al* [8]
[2] Sample Broke down Cavallini *et al* [22]
[3] No Signs of Breakdown Ariastina *et al*[4]
[4] No Signs of Breakdown Ariastina *et al*[4]

5.3.2 PD signals from different sources

5.3.2.1 Signal strength per unit width

Figures 5.9 (a) and (b) show the relationships between the PD signal strength L and its spread (1-S) during the 1^{st} and 3^{rd} quarter cycles respectively.

The locus L = (1-S) is that for a step function signal displaced from a phase angle of 90^o towards 0^o. The test data have been normalised also as indicated in Section 5.3.1.1, i.e. the first point is normalised to fit the step signal locus and the subsequent points scaled accordingly.

The loci of the data points of *Indo*1 and *Internal* lie below the normalised locus L = (1-S) for both 1^{st} and 3^{rd} quarter cycles. The loci for the *Floating*, *Surface* and *Corona* points lie above the L = (1-S) line for 1^{st} but not substantially so to reach a critical level as for the breakdown criteria of Section 5.3.1.2.

This indicates a negative rate of change between the signal's strength and its spread, i.e the PD activity reduced strength as it spread. During the 3^{rd} QC, in Figure 5.9(b), only the *Floating* data points were above the normalised line.

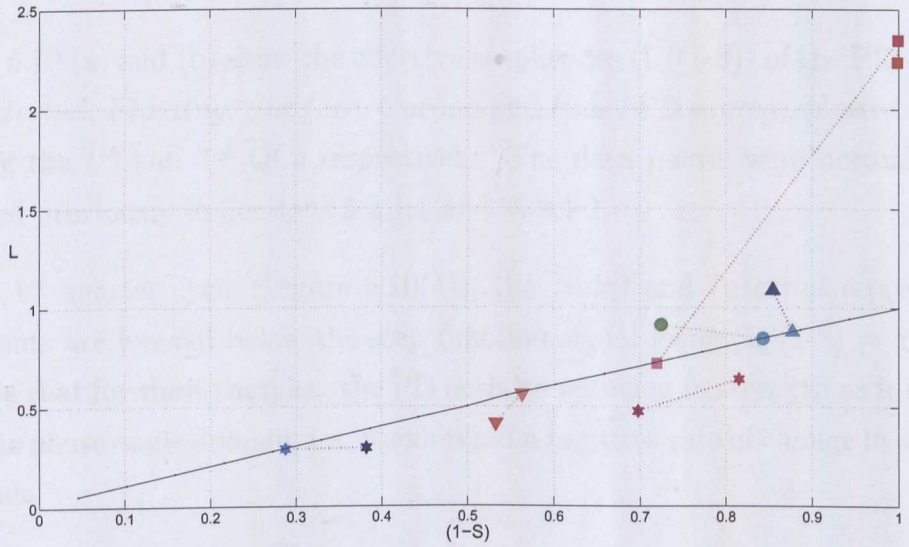

(a) 1^{st} quarter cycle

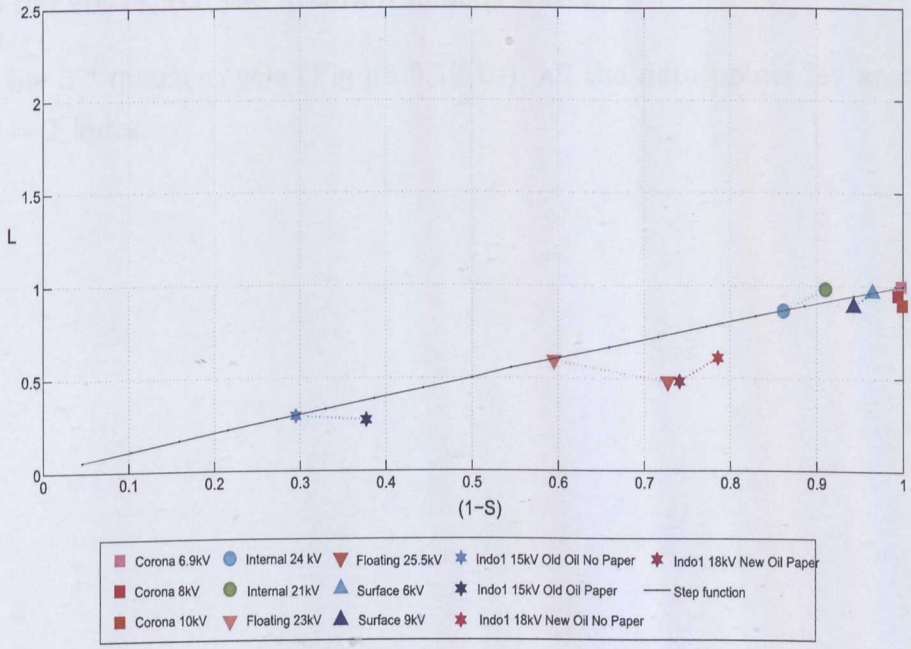

(b) 3^{rd} quarter cycle

FIGURE 5.9: Signal strength per unit width.

5.3.2.2 Effective amplitude

Figures 5.10 (a) and (b) show the effective amplitudes (L/(1-S)) of the PD activity from *Internal*, *Floating*, *Surface*, *Corona* and *Indo1* PD sources, plotted against z during the 1^{st} and 3^{rd} QCs respectively. The data points were normalised as described previously in Sections 5.3.1.1 and 5.3.1.2.

For the 1^{st} quarter cycle (Figure 5.10(a)), the *Indo1* and *Internal* representing data points are located below the step function signal locus (L/(1-S) = z). This indicates that for these samples, the PD activity reducing in strength as it spreads along the phase angle domain, i.e. it exhibited a negative rate of change in effective amplitude.

During the 1^{st} quarter cycle, the *Floating*, *Surface*, and *Corona* data exhibited a positive rate of change in the effective amplitude. The data points for *Floating* and *Surface* samples did not exceed the *Low* limit (1 to 1.5) and the *Corona* samples did not exceed the *Medium* limit (1.5 to 2.5).

During the 3^{rd} quarter cycle (Figure 5.10(b)), all the data points lay around the L/(1-S) = 1 locus.

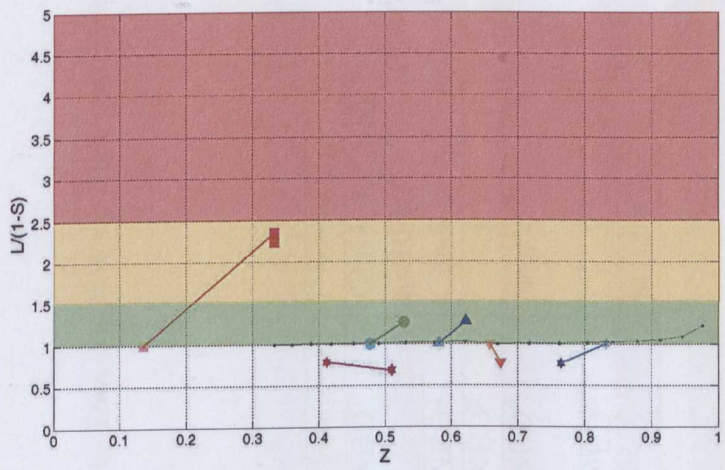

(a) 1^{st} quarter cycle

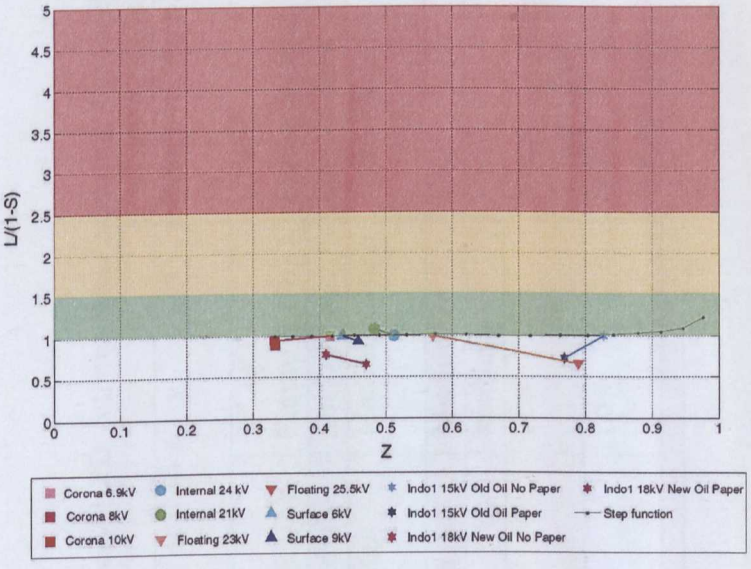

(b) 3^{rd} quarter cycle

FIGURE 5.10: The effective amplitude of PD signals as a function of z.

The results shown on Figures 5.1 (a) and (b) for L/(1-S) : z and on Figure 5.10 for $z : y$ are summarised on Table 5.2:

TABLE 5.2: Summary of processed PD activity data indicating the location of various data in Low, Medium or High possibility breakdown regions

Parameter	Activity spread $z : y$		Effective Amplitude L/(1-S) vs. z			
Quarter Cycle	1^{st} QC Figure 5.1(a)	3^{rd} QC Figure 5.1(b)	1^{st} QC Figure 5.10(a)	3^{rd} QC Figure 5.10(b)		
PD data set	Loci of data	Loci of data	Loci of data	Loci of data	Comments	Observation
Corona	Low+High	Medium+High	Low+Medium	Low	NBD[1]	Check L/(1-S) at 10 kV +
Floating	Medium	Medium	Low	Low	NBD[2]	Check z
Surface	Low	Medium	Low	Low	NBD[3]	Check z
Internal	Low	Low	Below normalised line	Below normalised line	NBD[4]	Safe
Indo1	Low	Low	Below normalised line	Below normalised line	NBD[5]	Check L/(1-S) at 18 kV+

[1] No Signs of Breakdown Liwei *et al*[7]
[2] No Signs of Breakdown Liwei *et al*[7]
[3] No Signs of Breakdown Liwei *et al*[7]
[4] No Signs of Breakdown Liwei *et al*[7]
[5] No Signs of Breakdown Ariastina *et al*[91]

The processed data points can be located in *Medium* and *High* concern areas on Figures 5.10 (a) and (b), however the final decision about the insulation breakdown can only be taken in conjunction with the other chromatic diagrams, e.g $z : y$, Figure 5.1 as the PD activity can exhibit a high rate of change in its effective amplitude however its representing z chromatic parameter is far from the (0.33 0.33), and vis-versa. In the *Corona*, *Floating*, *Internal*, *Surface* and *Indol* tests, the insulation was not compromised, as confirmed by Liwei *et al* in [7] and Ariastina *et al* in [91] respectively.

5.4 Summary

PD data sets from different sources have been chromatically processed. PD data from sources progressing in time or voltage level towards breakdown have also been processed.

Various chromatic parameters characteristics have been derived and presented for all the data investigated. These characteristics are based upon the chromatic parameters z, y (dominant location of signal in phase angle space), (L), the effective signal strength and (1-S), the effective signal spread with phase angle.

The characteristics can be used for quantifying the symmetry of PD signals, the polarity effect between positive and negative voltage half cycles, effective amplitude and dominant phase angle.

Using such quantified features, various types of Partial Discharges have been distinguished and progression towards full breakdown as a function of time or applied voltage identified. More empirical data is needed to tune the boundaries between *normal*, *medium* and *high* risk areas in various chromatic diagrams.

The decision regarding insulation breakdown can be based upon theree main criteria:

- The extent to which the signal dominant phase is displaced across the quarter cycle.
- The variation of the signal strength with regard its width.
- The effective amplitude of the signal.

Other chromatic features can be used also to confirm the outcomes leading to the above decision. Clusters of data points from symmetry/polarity effect diagrams and their progression around the symmetry/polarity lines, have been used as an indication of the PD activity progression towards breakdown and PD source discrimination.

Chapter 6

Conclusion

A new approach based upon the concept of chromaticity has been produced for interpreting signals emitted by partial discharges. It has advantages of flexibility and traceability in interpreting the nature of such signals.

Two different forms of chromatic filter responses have been considered for producing the various chromatic parameters (x, y, z and H, L, S). Truncated triangular filters were preferred since they could be more conveniently adapted for addressing various quarter cycles segments of an AC waveform.

Various chromatic diagrams have been generated from the chromatic parameters. For the purposes of this thesis the following diagrams are found to be useful:

- $z : y$ Cartesian diagram indicating the proportion of the signal in the first half of a quarter cycle of an AC cycle from the 90^0 limit. It enabled the spread of the PD activity across the quarter cycle at relatively lower levels of the AC voltage to be obtained.
- L : (1-S) Cartesian diagram relating the signal strength to its spread.
- L/(1-S) : z Cartesian diagram indicating how the effective amplitude per unit signal width varies as the signal progressively spreads across the quarter cycle. As such, it is a normalised indication of how the severity of the PD activity changes.

Raw PD data, acquired from various sources [4] [7] [8] [22] have been chromatically processed.

The data sets have been divided into two main categories:

1. Those concerned with identifying PD activities produced by different sources.
2. Those obtained as:
   - The applied voltages were increased for a fixed source condition.
   - The time variation progressing towards full breakdown.

The results presented show the complex nature of the data. Various features of the signals have been indicated. These are based upon the level of PD charge produced, the phase angle (during positive and negative half cycles) at which PD activity commenced and the phase angle duration of the PD activity. This preprocessed data was charaterised using phase angle domain chromatic processing.

Various characteristics based upon the chromatic parameters have been derived and presented for all the data investigated. These characteristics are based upon the chromatic parameters z, y (dominant location of signal in phase angle space), (L), the effective signal strength and (1-S), the effective signal spread with phase angle.

Using such quantified features, various types of Partial Discharges have been distinguished and progression towards full breakdown as a function of time or applied voltage identified. The same conclusion were also drawn by the PD data initiators (Chapter 2). However with chromaticity, they were drawn in a simpler and more informative and traceable method, which supported the motivating driver behind the development of the technique.

It is suggested that a decision regarding insulation breakdown could be based upon two criteria:

- The extent to which the signal dominant phase is displaced across the quarter cycle towards lower phase angles (and hence instantaneous voltages).
- The effective amplitude of the signal.

The chromatic parameters were also used for quantifying the symmetry of PD signals, polarity effects between positive and negative voltage half cycles, effective

amplitude and dominant phase angle. The clusters of data points from symmetry and polarity effect chromatic diagrams have been used as an extra indication of the PD activity progression and PD source discrimination.

The robustness of the chromatic methodology has been shown to enhance the processing of complex data signals by easing the problem of interpreting PD signatures via the chromatic signal representing parameters. The process is facilitated through the use of H-L and H-S polar maps, 2D cartesian diagrams; $x : y$, $z : y$, $x : z$ or 3D space (θ, z, r) diagrams. These diagrams, along with other derived ones e.g. L/(1-S), can provide clearer indications of which cross-correlation means would give meaningful and accurate results regarding any hidden information within the complex data signals.

The Chromatic methodology enables numerical scales of judgment to be established. Unlike Neural Networks, Fuzzy logic, SVM...etc, the chromatic approach has a high degree of traceability, lends itself to a hierarchical approach to provide different levels of detailed information and significantly enables the quantified information to be easily assimilated via patterns so that in-depth mathematical knowledge is not mandatory.

Future work could address the following aspects:

- The Chromatic methodology has been validated with raw PD data from various PD sources and samples leading to breakdown. The extent to which the approach can be used to locate PD events within HV equipment, e.g. (PD events in transformers at weak locations; close to extremities, windings joint-points...etc) and discriminate between voids sizes, requires further investigation.

- It is also worth exploring the first stage of the method (Chromatic filtering) to extract PD signal features and constitute a features vector for any ANN, Fuzzy Logic, SVM...etc engine. Subsequent classification could be based on the Chromatic parameters, R_o, G_o, B_o, or H, L, S rather than being based on statistical or time analysis of pulse shape, PCA or wavelet transform.

- For practical monitoring applications, the algorithm processing the PD raw data, could be uploaded to a microchip and embedded with a data acquisition device and display unit into a hand held clamp-type split core monitoring device or sent via a mobile phone connection to a database for further processing.

Bibliography

[1] CENELEC. High-voltage test techniques, partial discharge measurements, 2001.

[2] E. Lemke. Guide for partial discharge measurements in compliance to iec 60270. *CIGRE D1.33 High Voltage Test and Measuring Techniques*, pages 1–55, 2008.

[3] S. Das and P. Purkait. phi-q-n pattern analysis for understanding partial discharge phenomena in narrow voids. *IEEE Power and Energy Society General Meeting*, pages 1–7, 2008.

[4] W.G. Ariastina and T.R. Blackburn. Characteristics of partial discharge in oil impregnated insulation using different test voltage frequencies. *IEEE International Conference on Properties and Applications of Dielectric Materials*, 1:487–492, 2000.

[5] G.R. Jones, P.C. Russell, A. Vourdas, J. Cosgrave, L. Stregioulas, and R. Haber. The gabor transform basis of chromatic monitoring. *IEEE Measurement Science and Technology*, 11(5):489–498, 2000.

[6] G.R. Jones, A.G. Deakin, and J.W. Spencer. *Chromatic Monitoring of Complex Conditions.* Number ISBN 13.978-1-58488-988-5. Taylor and Francis, Florida, USA, 2008.

[7] L. Hao and P.L. Lewin. Phase resolved partial discharge identification using a support vector machine. In *23rd IAR Workshop on Advanced Control and Diagnosis*, pages 386–391, 2008.

[8] K.X. Lai, A. Lohrasby, B.T. Phung, and T.R. Blackburn. Partial discharge characteristics of electrical trees prior to breakdown. In *International Symposium on Electrical Insulating Materials*, pages 649–652, 07-11 September 2008.

[9] A. Cavallini, M. Conti, A. Contin, G.C. Montanari, and G. Pasini. An integrated diagnostic tool based on pd measurements. *IEEE Electrical Insulation Conference & Electrical Manufacturing and Coil Winding Conference*, pages 219 – 224, 16 - 18 Oct 2001.

[10] M.M.A. Salama and R. Bartnikas. Determination of neural network topology for partial discharge pulse pattern recognition. *Transactions on Neural Networks*, 13(2):446–456, March 2002.

[11] G. Lupo, C. Petrarca, L. Egiziano, V. Tucci, and M. Vitelli. Partial discharge testing on resin insulated voltage transformers. *Electrical Engineering (Archiv fur Elektrotechnik)*, 81(2):89–97, 1996.

[12] W. Chang and H. Yang. Partial discharge pattern recognition of molded type transformers using self organizing map. In *International Conference on Properties and Applications of Dielectric Materials*, pages 246–249. Institute of Electrical and Electronics Engineers Inc, Bali, Indonesia, June 2006.

[13] M. Fidan and H. Ismailoglu. A novel partial discharge calibrator design via dual microcontroller and high speed dac. In *International Conference on Electrical and Electronics Engineering*, Bursa (Turkey), Dec 2009.

[14] M.H. Wang. Partial discharge pattern recognition of current transformers using an enn. *IEEE Transactions on Power Delivery*, 20(3):1984–1990, July 2005.

[15] C.D. Russell, C.D. Sudworth, N. Krasner, M. Haqqani, G.R. Jones, and A. Deakin. Signal processing techniques for oct images of human tissue. In *European Conference on Biomedical Optics (ECBO)*, June 2005.

[16] O.A. Oraby, J.W. Spencer, and G.R. Jones. Monitoring changes in the speckle field from an optical fibre exposed to low frequency acoustical vibrations. *Journal of Modern Optics*, 56(1):73–84, 2009.

[17] J. Zhang, G.R. Jones, J.W. Spencer, P. Jarman, I.J. Kemp, Z. Wang, P.L. Lewin, and R.K. Aggarwal. Chromatic classification of rf signals produced by electrical discharges in hv transformers. *IEE Proceedings Generation, Transmission and Distribution*, 152(5):629–634, 2005.

[18] M. Ragaa, J.W. Spencer, G.R. Jones, and A.G. Deakin. Characterisation of partial discharge signals using a chromatic approach. In *Proceedings of the XVIII Gas Discharge Conference*, pages 556–559, 2010.

[19] M. Ragaa, G.R. Jones, A.G. Deakin, and J.W. Spencer. Partial discharge monitoring using chromatic maps. In *19th International Conference on Gas Discharges and Their Applications*, Beijing, China, September 2012.

[20] H.M. Ryan. *High Voltage Engineering and Testing.* The Institution of Electrical Engineers, 4 edition, 2012.

[21] S.A. Boggs. Partial discharge: Overview and signal generation. *IEEE Electrical Insulation Magazine*, 6:33–39, July/August 1990.

[22] A. Cavallini, M. Conti, G.C. Montanari, C. Arlotti, and A.Contin. Pd inference for the early detection of electrical treeing in insulation systems. *IEEE Transactions on Dielectrics and Electrical Insulation*, 4:724 – 735, August 2004.

[23] S. Bahadoorsingh and S.M. Rowland. A framework linking knowledge of insulation ageing to asset management. *IEEE Electrical Insulation Magazine*, 24:38–46, 2008.

[24] T.K. Abdel-Galil, Y.G. Hegazy, M.M.A. Salama, and R. Bartnikas. Partial discharge pulse pattern recognition using hidden markov models. *IEEE Transactions on Dielectrics and Electrical Insulation*, 11:715 – 723, August 2004.

[25] T.K. Abdel-Galil and I.O. Habiballah. Challenges of using partial discharge measurements for predictive maintenance. In *Transmission and Distribution Conference & Exhibition.* IEEE/PES, 2005.

[26] H. Suzuki and T. Endoh. Pattern recognition of partial discharge in xlpe cables using neural network. *IEEE Transactions on Electrical Insulation*, 27(3):543–549, June 1992.

[27] L. Weidong, L. Shanghe, and H. Xiaofeng. Feature extraction and pattern recognition of signals radiated from partial discharge. In *5th Asia-Pacific Conference on Environmental Electromagnetics CEEM*, pages 114–117, 2009.

[28] E. Gulski and A. Krivda. Neural networks as a tool for recognition of partial discharges. *IEEE Transactions on Electrical Insulation*, 28(6):984–1001, November 1993.

[29] G. Mirelli and R. Schifani. A novel method for the recognition of pd patterns by neural network. In *Conference on Electrical Insulation and Dielectric Phenomena*, pages 206–209, 1999.

[30] W.Y. Chang and H.T. Yang. Application of self organizing map approach to partial discharge pattern recognition of cast-resin current transformers. *WSEAS Transactions on Computer Research*, 3(3):142–151, March 2008.

[31] T. Hong, M.T.C Fang, and D. Hilder. Pd classification by a modular neural network based on task decomposition. *IEEE Transactions on Dielectrics and Electrical Insulation*, 3(2):207 – 212, 1996.

[32] D. Evagorou, A. Kyprianou, P.L.. Lewin, A.. Stavrou, V. Efthymiou, and G.E. Georghiou. Classification of partial discharge signals using probabilistic neural network. In *IEEE International conference on Solid Dielectrics ICSD*, pages 609–615, 2007.

[33] W. Li, J. Luo, R. Xia, J. Zhao, S. Meng, Y. Jiang, and H. Min. Partial discharge pattern analysis based on 2-d wavelet transform. In *Asia-Pacific Power and Energy Engineering Conference (APPEEC)*, pages 1–3, March 2010.

[34] Y. Tian, P.L. Lewin, S.J. Sutton, and S.G. Swingler. Pd characterization using wavelet decomposition of acoustic emission signals. In *International Conference on Solid Dielectrics*, Toulouse, France, July 2004.

[35] Y. Tu, Z.D. Wang, and P.A. Crossley. Partial discharge pattern recognition based on 2-d wavelet transform and neural network techniques. In *IEEE Power Engineering Society Summer Meeting*, volume 1, pages 411 – 416, Chicago, IL, USA, July 2002.

[36] E.M. Lalitha and L. Satish. Wavelet analysis for classification of multisource pd patterns. *IEEE Transaction on Dielectrics and Electrical Insulations*, 7:40–47, February 2000.

[37] T.K. Abdel-Galil, M.M.A. Salama R.M. Sharkawy, and R. Bartnikas. Partial discharge pulse pattern recognition using an inductive inference algorithm. *IEEE Transaction on Dielectric and Electrical Insulation*, 12(2):320–327, 2005.

[38] A.A. Mazroua, R. Bartnikas, and M.M.A. Salama. Neural network system using multi-layer perceptron technique for the recognition of pd pulse shapes due to cavities and electrical trees. *IEEE Transactions on Power Delivery*, 10(1):92–96, January 1995.

[39] M.M.A. Salama and R. Bartnikas. Fuzzy logic applied to pd pattern classification. *IEEE Transactions on Dielectrics and Electrical Insulation*, 7(1):118–123, February 2000.

[40] H.C. Chang, Ying-Piao Kuo, Chun-Yao Lee, and Han-Wei Lin. A partial discharge based defect-diagnosis system for cast-resin current transformers. In *39th International Universities Power Engineering Conference UPEC*, volume Vol. 1, pages 233 – 237, 2004.

[41] A.A. Mazroua, R. Bartnikas, and M.M.A. Salama. Pd pattern recognition with neural networks using the multi-layer perceptron technique. *IEEE Transactions on Electrical Insulation*, 28:1082–1089, 1993.

[42] A.A. Mazroua, R. Bartnikas, and M.M.A. Salama. Discrimination between pd pulse shapes using different neural net work paradigms. *IEEE Transactions on Electrical Insulation*, 21:1119–1131, 1994.

[43] T.K. Abdel-Galil, R.M. Sharkawy, M.M.A. Salama, and R. Bartnikas. Partial discharge pattern classification using the fuzzy decision tree approach. *IEEE Transactions on Instrumentation and Measurement.*, 54(6):2258–2263, December 2005.

[44] H.G. Kranz. Diagnosis of partial discharge signals using neural networks and minimum distance classification. *IEEE Transactions on Electrical Insulation*, 28(6):1016–1024, December 1993.

[45] E.F. El-Saadany, M.M.A. Salama, K.W. Hipel, and A.Y. Chikhani. Stochastic time series modeling for load forecasting. *Power Energy Systems*, 18:199–205, 1998.

[46] J.M. Mendel. Fuzzy logic systems for engineering: a tutorial. *Proceedings of the IEEE*, Vol 83(issue 3):345 – 377, March 1995.

[47] S. Gopal, B. Karthikeyan, and D. Kavitha. Partial discharge pattern classification using fuzzy expert system. In *International Conference on Solid Dielectrics*, volume 2, pages 653 – 656, Toulouse France, July 2004.

[48] S.C. Wang and P.H. Huang. Fuzzy c-means clustering for power system coherency. In *IEEE International Conference on Systems Man and Cybernetics*, volume 3, pages 2850–2855, October 2005.

[49] W.Y. Chang and H.T. Yang. Application of fuzzy c-means clustering approach to partial discharge pattern recognition of cast-resin current transformers. In *8th International Conference on Properties and applications of Dielectric Materials*, pages 372 – 375, June 2006.

[50] W.Y. Chang. Partial discharge pattern recognition for cast-resin current transformer. In *IEEE 9th International Conference on the Properties and Applications of Dielectric Materials ICPADM*, pages 461 – 464, July 2009.

[51] K. Zalis. Applications of expert systems in evaluation of data from partial discharge diagnostic measurement. In *Proceedings of the 7th International Conference on Properties and Applications of Dielectric Materials*, volume 1, pages 331 – 334, June 2003.

[52] U. Fayyad, G. Piatetsky-Shapiro, and P. Smyth. From data mining to knowledge discovery in databases. *American Association for Artificial Intelligence*, 17(3):37–54, 1996.

[53] A. Abdelhalim and I. Traore. A new method for learning decision trees from rules. In *International Conference on Machine Learning and Applications*, pages 693–698, 2009.

[54] K.X. Lai, B.T. Phung, and T.R. Blackburn. Descriptive data mining of partial discharge using decision tree with genetic algorithm. In *Australasian Universities Power Engineering Conference, AUPEC*, pages 1–6, December 2008.

[55] K.X. Lai, B.T. Phung, and T.R. Blackburn. Investigation of partial discharge in single void and multi-voids using data mining technique. In *Australasian*

Universities Power Engineering Conference AUPEC, pages 1–6, Septembre 2009.

[56] X. Ma, C. Zhou, and J. Kemp. Interpretation of wavelet analysis and its application in partial discharge detection. *IEEE Transactions on DielecIrics and Electrical Insulation*, 9(3):446457, June 2009.

[57] A.O. Akumu, H. Masai, F. Adachi, R. Ozaki, H. Ihori, M. Fujii, and K. Arii. Wavelet analysis of partial discharge acoustic signals in a model transformer. *Japan Journal of Applied Physics*, 42:5347–5352, 2003.

[58] A. Sarikhani, E. Reihani, N. Nabizadeh, A. Hooshmand, and M. Davodi. Analysis of partial discharge by wavelet hilbert transform. *European Transactions on Electrical Power*, 19:11401152, 2009.

[59] Y. Xie, J. Tang, and Q. Zhou. Feature extraction and recognition of uhf partial discharge signals in gis based on dual-tree complex wavelet transform. *European Transactions on Electrical Power*, 2009.

[60] E. Gulski. *Computer-aided Recognition of Partial Discharges Using Statistical Tools.* Delft University Press, 1991.

[61] A. Krivda. Automated recognition of partial discharge. *IEEE Transaction on Dielectrics and Electrical Insulations*, 2:796–821, October 1995.

[62] T. Okamoto and T. Tanaka. Partial discharge pattern recognition for three kinds of model electrode with a neural network. In *IEE Proceedings Science, Measurement and Technology.*, volume 142, pages 75–84, January 1995.

[63] M. Li, X. Liu, and X. Zhang. Pd pattern recognition based on linear discriminant analysis for gis. In *International Conference on High Voltage Engineering and Application (ICHVE)*, pages 297 – 300, Octobre 2010.

[64] M.K. Abdul Rahman, R. Arora, and S.C. Srivastava. Partial discharge classification using principal component transformation. In *IEE Proceedings Science, Measurement and Technology*, volume 147, pages 7 – 13, January 2000.

[65] M.A. Eldery, T.K. Abdel-Galil, E F. El-Saadany, and M.M.A. Salama. Identification of partial discharge locations in transformer winding using psd estimation. *IEEE Transaction on Power Delivery*, 21(2):1022–1023, April 2006.

[66] X. Zhang, Y. Yao, and J. Tang. Partial discharge pattern recognition based on optimal uncorrelated discriminant vectors in gis. *European Transactions on Electrical Power*, 19:1098–1108, September 2009.

[67] X. Zhu, Y. Yu, and X. Guo. Extension theory and the application in optimization of immune neural network. In *First International Workshop on Education Technology and Computer Science ETCS*, volume 1, pages 842 – 847, March 2009.

[68] K.X. Lai, B.T. Phung, T.R. Blackburn, and N.A. Muhamad. Classification of partial discharge using pca and som. In *International Power Engineering Conference IPEC*, pages 1311 – 1316, December 2007.

[69] A.M. Martinez and A.C. Kak. Pca versus lda. *IEEE Transactions on Pattern Analysis and Machine Intelligence*, 23(2):228–233, February 2001.

[70] V. Chatpattananan, N. Pattanadech, and K. Vicetjindavat. Pca-lda for partial discharge classification on high voltage equipment. In *8th International Conference on Properties and applications of Dielectric Materials*, pages 479–481, 2006.

[71] B. Scholkopf and A. Smola. *Learning with Kernels Support Vector Machines, Regularization Optimization and Beyond.* MIT Press, 2002.

[72] J. Shawe-Taylor and N. Christianini. *Kernel Methods for Pattern Analysis.* Cambridge University Press, 2004.

[73] L. Hao, P.L. Lewin, Y. Tian, and S.J. Dodd. Partial discharge identification using a support vector machine. In *Conference on Electrical Insulation and Dielectric Phenomena*, pages 414 – 417, October 2005.

[74] L. Hao, P.L. Lewin, and S. Dodd. Comparison of support vector machine based partial discharge identification parameters. *IEEE International Symposium on Electrical Insulation*, pages 110–113, June 2006.

[75] L. Hao, P.L. Lewin, and S.G. Swingler. Identification of multiple partial discharge sources. In *International Conference on Condition Monitoring and Diagnosis*, pages 118–121, The Tony Davies High Voltage Laboratory, University of Southampton, Highfield, Southampton, SO17 1BJ, UK, 2008.

[76] L. Hao, P.L. Lewin, and S.G. Swingler. Use of machine learning for partial discharge discrimination. In *The 11th International Electrical Insulation Conference*, pages 115–120, 2009.

[77] L. Hao and P.L. Lewin. Partial discharge source discrimination using a support vector machine. *IEEE Transactions on Dielectrics and Electrical Insulation*, 17:189–197, 2010.

[78] J.A. Hunter, L. Hao, P.L. Lewin, D. Evagorou, A. Kyprianou, and G.E. Georghiou. Comparison of two partial discharge classification methods. In *Conference Record of the IEEE International Symposium on Electrical Insulation (ISEI)*, pages 1 – 5, June 2010.

[79] A.G. Deakin, I. Rallis, J. Zhang, J.W. Spencer, and G.R. Jones. Towards holistic chromatic intelligent monitoring of complex systems. In *Complexity, Science and Society.* The University of Liverpool, September 2005.

[80] P.H. Moon and D.E. Spencer. *The Photic Field.* MIT Press, Cambridge, Massachusetts, 1981.

[81] J. Zhang and G.R. Jones. Chromatic processing for event probability description. In *Proceedings of the Complex Systems Monitoring Session of the International Complexity, Science and Society Conference UK.Liverpool*, pages 61–67. CIMS, September 2005.

[82] G.R. Jones, P.C. Russell, A. Vourdas, J. Cosgrave, L. Stergioulas, and R. Haber. The gabor transform basis of chromatic monitoring. *IEEE Measurement Science and Technology*, 11(5):489–498, 2000.

[83] A. Koh, E.M. Dean, J. Zhang, G.R. Jones, and J.W. Spencer. Effect of chromatic filter characteristics in quantifying complex data. In *Proceedings of the Complex Systems Monitoring Session of the International Complexity, Science and Society Conference UK.Liverpool.* CIMS, September 2005.

[84] J. Zhang, G.R. Jones, A. Deakin, and J.W. Spencer. Chromatic processing of dga data produced by partial discharges for the prognosis of hv transformer behaviour. *Measurement Science & Technology*, 16:556–561, 2005.

[85] G.R. Jones, A.G. Deakin, and J.W. Spencer. Multistimulus chromatic processing of complex signals. In *Proceedings of the Complex Systems Monitoring Session of the International Complexity, Science and Society Conference, UK.Liverpool*, pages 5–15. Centre for Intelligent Monitoring Systems (CIMS), September 2005.

[86] L.K. Stergioulas. *Time-frequency methods in optical signal processing.* PhD thesis, University of Liverpool, 1997.

[87] F.W. Billmeyer and M. Saltzman. *Principles of Color Technology.* John Wiley, New York, 1981.

[88] G.R. Jones and P.C. Russell. Chromatic modulation based metrology. *Pure and Applied Optics Journal*, 2:87–110, 1993.

[89] B. Han. *Partial Discharge Monitoring of Power Transformers.* PhD thesis, University of Southampton, 2004.

[90] W.G. Ariastina and T.R. Blackburn. Comparison of measured pds in oil-impregnated insulation using different sensor bandwidths. In *Proceedings of the International Symposium on Electrical Insulation Materials (ISEIM)*, number 4-21 in 1, pages 864–867, November 2001.

[91] W.G. Ariastina and T.R. Blackburn. Distribution of partial discharges in oil-impregnated insulation. In *Australasian Universities Power Engineering Conference*, pages 331–336, September 2000.

[92] A. Cavallini, M. Conti, G.C. Montanari, and A. Contin. Transition from pd to electrical tree in solid insulation inferred through enhanced detection tools. *IEEE International Conference on Solid Dielectrics ICSD*, 2:632 – 635, 2004.

[93] D.D. Chang, T.S. Sudarshan, and J.E. Thompson. Analysis of electric stress distribution in cavities embedded within dielectric structures. *IEEE Transaction on Electrical Insulation*, 21(2):213–219, April 1986.

[94] R.A. Orchard. *FuzzyClips V6.02 A User's Guide.* National Research Council of Canada, Ottawa, nrc/frb 1015 edition, 1995.

Appendix A

PD Measurement circuits

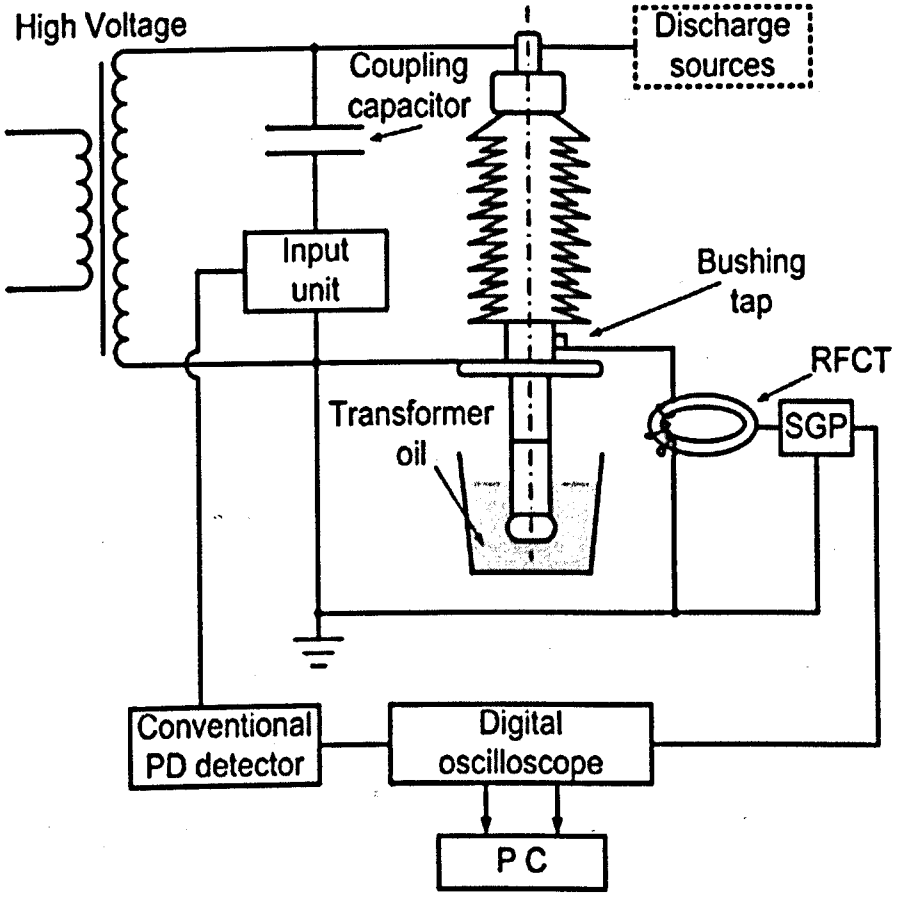

FIGURE A.1: Schematic diagram of the PD measurement circuit used by Hao *et al* [7].

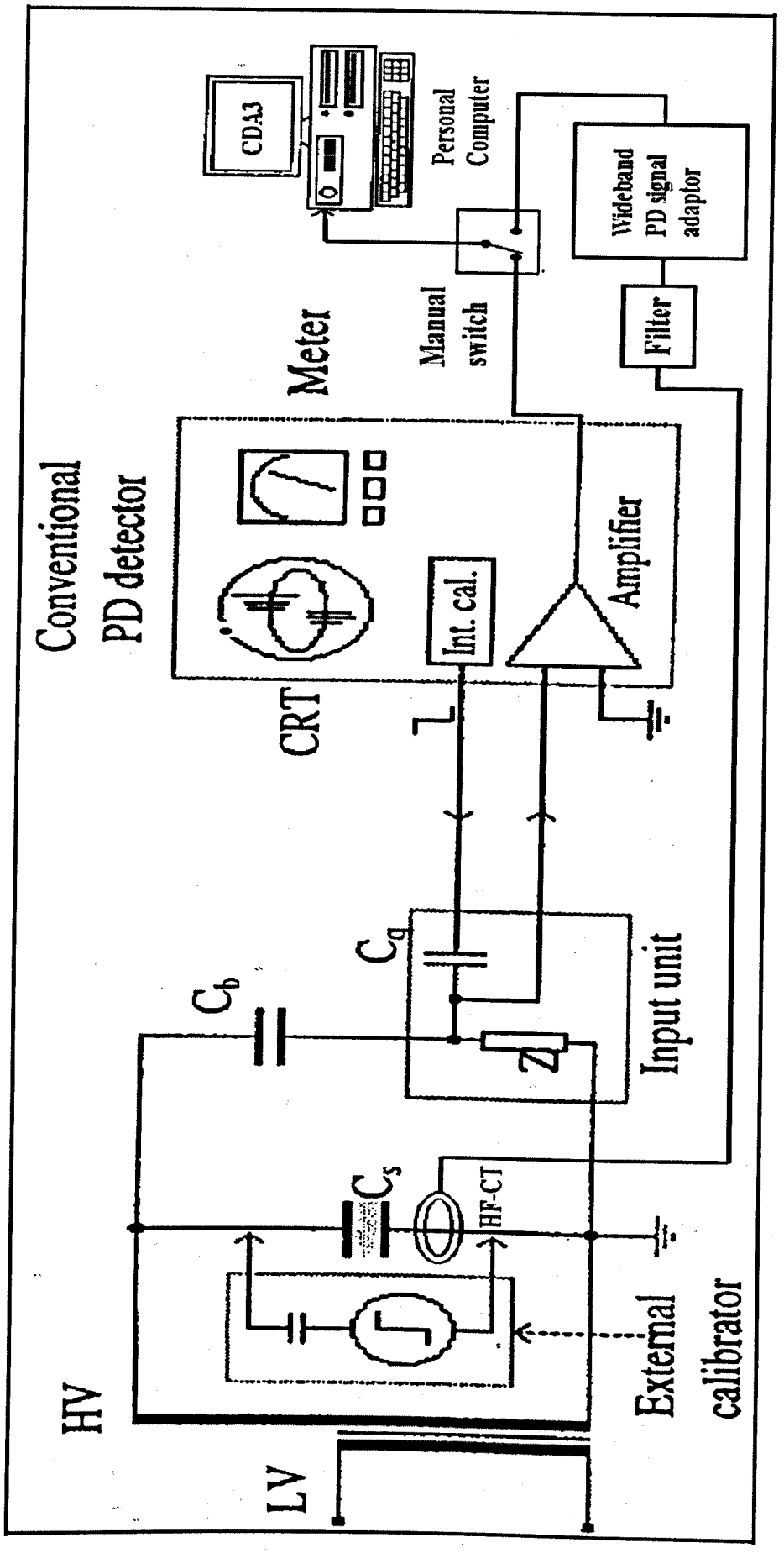

FIGURE A.2: Basic diagram of the PD measuring system used by Ariastina *et al* [4].

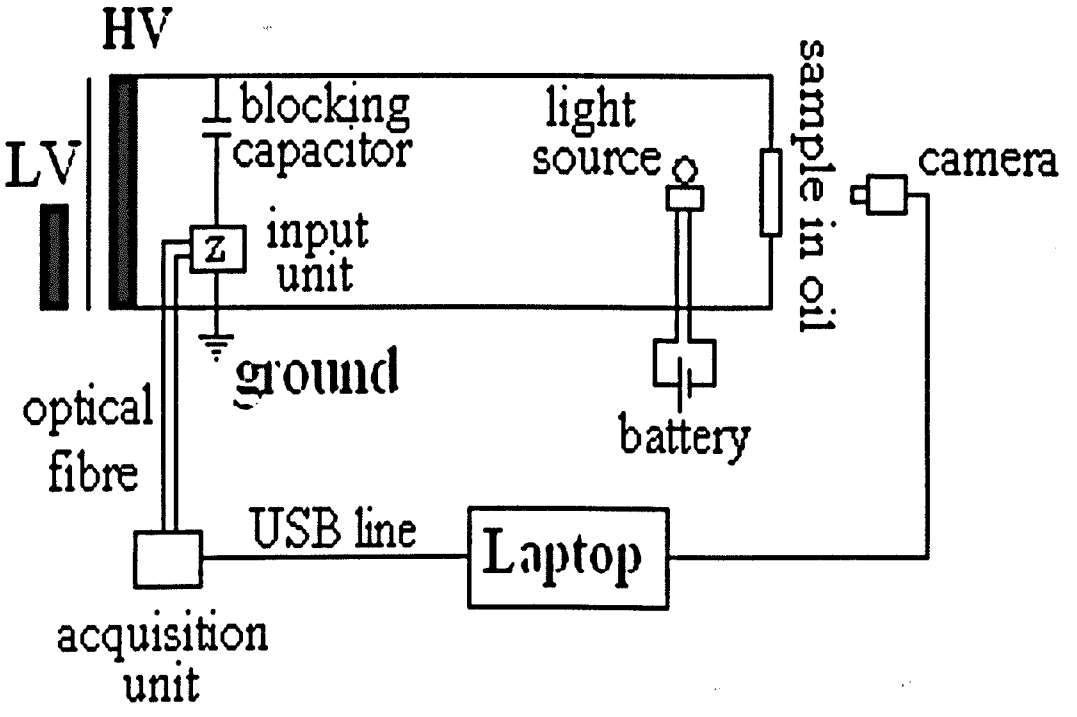

FIGURE A.3: PD measuring circuit used by Lai *et al* [8].

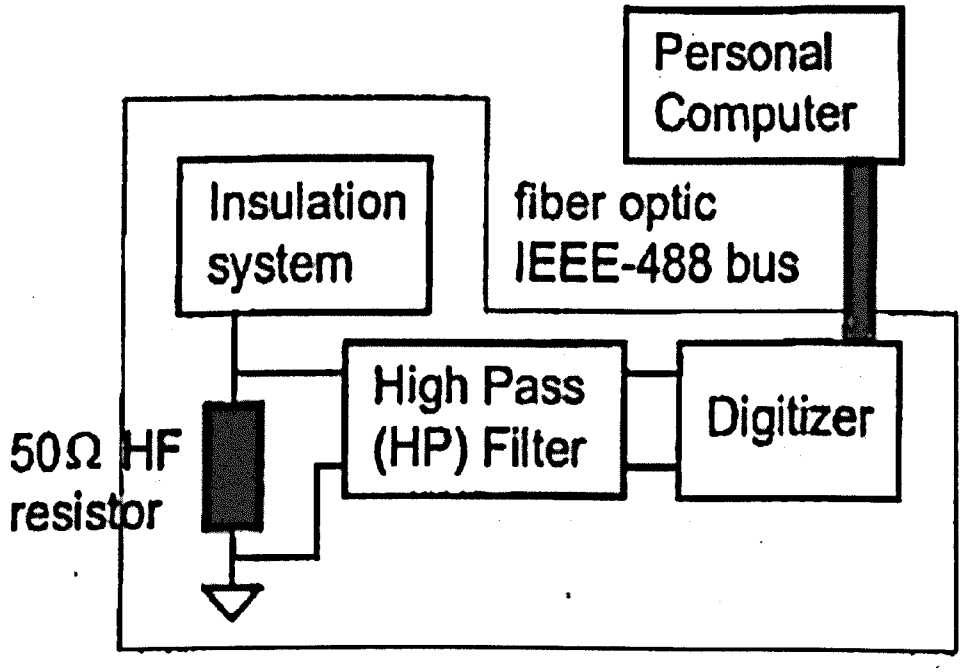

FIGURE A.4: PD measuring circuit used by Cavallini *et al* [9].

Appendix B

Matlab code

The loaded data files are in the $(n - \phi - q)$ format, which is the common format delivered by most PD detectors. This Matlab code was used to process the Australian PD data set and could be adapted to any PD data of the same format.

```
clear;
clc;

XYZ=[];
X=[];

% Data preconditioning

for jj = 1:3
   stdunsw2=[ ];
   SMunsw2=[ ]; % create new matrix for data
   AVunsw2=[ ];
   SMdiff=[ ];
   MAXunsw2=[ ];
   NumberOfPulses =[ ];
   NumberOfPD =[];

   filename = strcat(int2str(jj),'.txt');
   RGBunsw2 = dlmread(filename);   % dlemread (.txt) data
```

```
   RGBunsw2 = sortrows(RGBunsw2,1);
   RGBunsw2(:,2) = abs(RGBunsw2(:,2));

% Normalisation with regard the maximum range of the PD detector.

   RGBunsw2(:,2) =(RGBunsw2(:,2)./60);

% Standard deviation

  for i = 0:359
  NumberOfP = find(RGBunsw2(:,1)==i);
  stdunsw2 = [stdunsw2;i,std(RGBunsw2(NumberOfP,2))];
  stdunsw2(find (isnan(stdunsw2)))=0;
  end

  stdunsw2(:,2) =(stdunsw2(:,2).*1.7);% 95% of the signal

% Sorting the data

  for i = 0:359
  NumberOfP = find(RGBunsw2(:,1)==i);
  LenNoPulses =length( NumberOfP);
  SMunsw2 = [SMunsw2;i,sum(RGBunsw2(NumberOfP,2))];

  NumberOfPulses = [NumberOfPulses;i,LenNoPulses];

  AVunsw2 = [AVunsw2;i,mean(RGBunsw2(NumberOfP,2))];
  AVunsw2(find (isnan(AVunsw2)))=0;

  end

  Newboundary = [stdunsw2(:,1),(stdunsw2(:,2)+ AVunsw2(:,2))];

  for kk=1:length(Newboundary)
  RGBunsw2(find(RGBunsw2(:,1)==Newboundary(kk,1)),3) = Newboundary(kk,2);
  end
```

```
  for i=1:360

        if Newboundary(i,1)>= 315
           Newboundary(i,1)= Newboundary(i,1)- 360;
        end
  end

  Newboundary= [Newboundary(316:360,:);Newboundary(1:315,:)];

% Chromatic Filters:

  RF=linspace(1,0,90);                                  % Red triangular filter
  GF=[linspace(0,1,45) linspace(0.9773,0,45)];          % Green triangular filter
  BF=linspace(0,1,90);                                  % Blue triangular filter

% Processing data Processing of quarter cycles of signal

  for i = 1:4                          % calculation of R,G and B

  R(i) = sum((RF) .* Newboundary((i-1)*90+1:i*90,2)')/sum(RF);
  G(i) = sum((GF) .* Newboundary((i-1)*90+1:i*90,2)')/sum(GF);
  B(i) = sum((BF) .* Newboundary((i-1)*90+1:i*90,2)')/sum(BF);

  [H(i), L(i), S(i)]=convert_hsl(R(i),G(i),B(i));    % H,L,S calculation

  XY(i) = R(i)/(R(i)+G(i)+B(i));        % Calculating x,y,z
  YY(i) = G(i)/(R(i)+G(i)+B(i));
  ZY(i) = B(i)/(R(i)+G(i)+B(i))

  end

    XYZ=[XYZ; XY',YY',ZY'];

    X=[X;R',G',B',H',L',S'];
```

```
end

% Gathering results

 time = (1:3);

 for k = 1:3
 Hue(k) = X((k-1)*4+1,4);
 Lit(k) = X((k-1)*4+1,5);
 Sat(k) = X((k-1)*4+1,6);
 end

% L(H) plotting

  LSfigure(Hue, Lit, Hue, Lit, Sat, Sat);     % creates L/(1-S) plots

% Plot x,y,z

  XYZ_1=[XYZ(1:2,1),XYZ(5:6,1),XYZ(9:10,1)];
  XYZ_2=[XYZ(1:2,2),XYZ(5:6,2),XYZ(9:10,2)];
  XYZ_3=[XYZ(1:2,3),XYZ(5:6,3),XYZ(9:10,3)];

  createfigureXY(XYZ-2,XYZ-3);        % creates various x, y, z plots

% H,L,S vs. time plotting

  HLStimefigure(time, Lit, Sat, Hue);
  HLStimefigure(time, Lit, Sat, Hue);

% Polar plots

  polar-plot3(Lit1,Hue1,Lit2,Hue2);
```

Appendix C

Further chromatic diagrams

Figures C.1 and C.2 show the variation of the rate of change of PD activity within the 1st half cycle with respect the of the 2nd half cycle for both PD data from different PD sources and progressing towards breakdown.

The data points in both figures seem to drift away from the diagonal line (which represent an equal rate of change between the positive and negative half cycles), apart from the *Corona* point, which do the opposite.

This means that, when approaching breakdown, the difference in the change of PD activity within each half cycle tend to increase and this change could be proportional to the time left before breakdown.

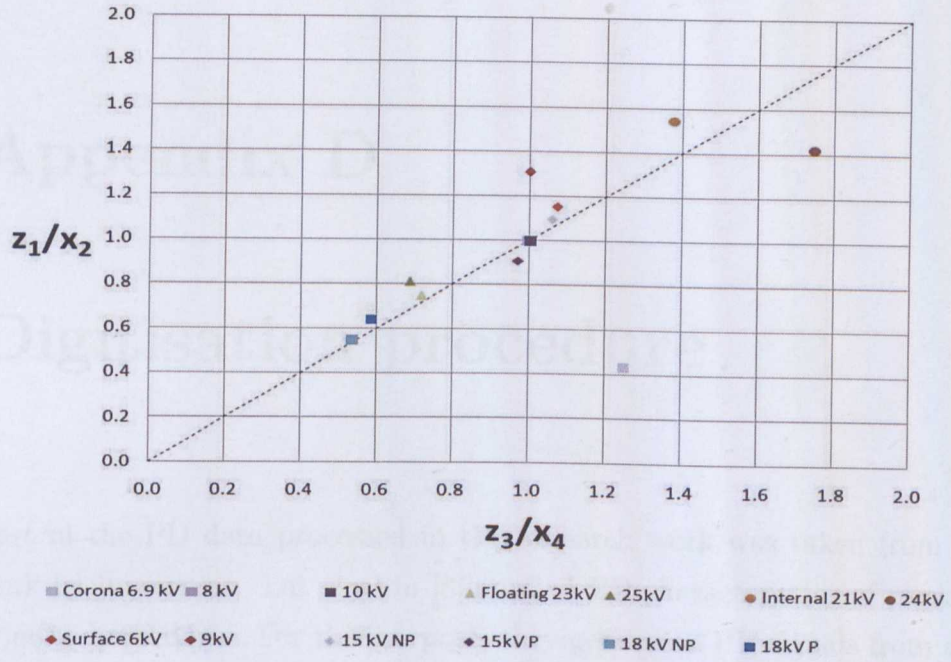

FIGURE C.1: 1st HC ratio vs 2nd HC multiple PD sources

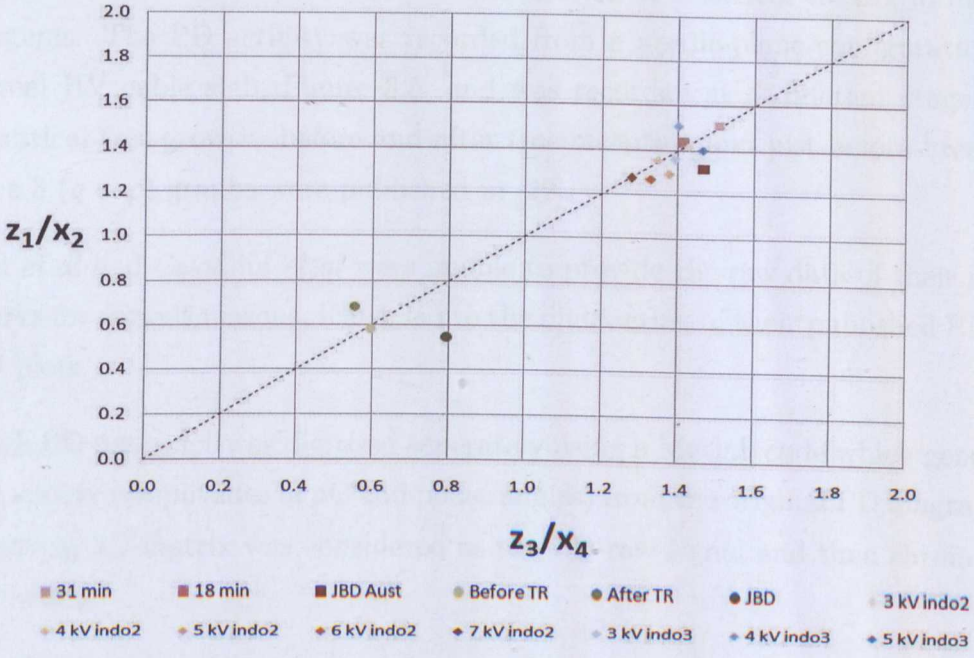

FIGURE C.2: 1st HC ratio vs 2nd HC progressing towards breakdown

Appendix D

Digitisation procedure

Part of the PD data processed in this research work was taken from published work by its owners. Lai *et al* in [8] studied PD characteristics of electrical trees prior to breakdown. For this purpose, they generated PD signals from a lab-built need-plane configuration, Figure 3.4. The $(q - \varphi)$ diagrams of the PD activity recorded at 3 different time stages (31, 18 minutes before breakdown, and just before breakdown) were published in [8].

Cavallini *et al* in [22], also generated PD data signals for the purpose of their research in PD inference for the early detection of electrical treeing in insulation systems. The PD activity was recorded from a needle-plane configuration using a real HV cable slab, Figure 3.5, and was recorded at 3 different stages of the electrical tree growth: before and after tree inception and just before breakdown. The 3 $(q - \varphi)$ graphs were published in [22].

Lai *et al* and Cavallini *et al* were unable to provide the raw data of their research works for various reasons, which led to the digitisation of their published PD signal 2D plots.

Each PD data plot was digitised seperately using a Matlab code which generates a 2D matrix (amplitudes in pC and phase angles) from the original PD diagram. The resulting 2D matrix was considered as the PD raw signal and then chromatically processed.

To visualy assess the acuracy of the digitisation procedure, a PD activity diagram, which was plotted from raw data Figure 3.13 (c) was digitised and the two plots (from raw and digitised data) were superimposed in the same diagram, Figure D.1.

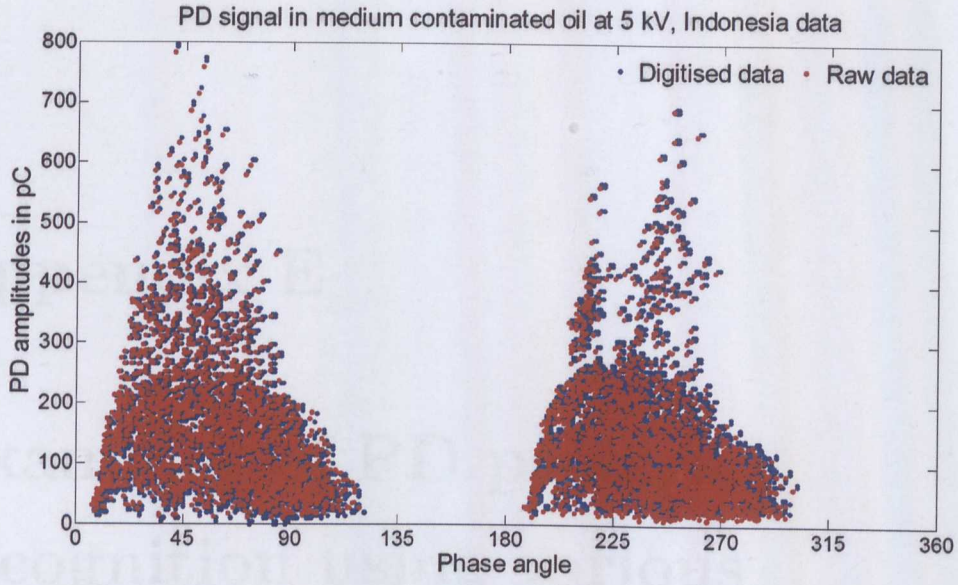

FIGURE D.1: Comparison between the same PD signal plotted from: Raw data and Digitised data

To quantify the digitisation procedure accuracy, the two signals in Figure D.1 were chromatically proceed seperately and their characterising chromatic parameters are summirised in Table D.1.

TABLE D.1: Accuracy of the digitisation procedure

Data	Chromatic parameters of the 1^{st} and 3^{rd} quarter cycles					
	H_1	H_3	L_1	L_3	S_1	S_3
Raw	225.87	225.76	0.144	0.110	1	1
Digitised	227.32	226.85	0.147	0.115	1	1
Accuracy (%)	99.36	99.51	97.96	95.65	100	100

Figure D.1 could also be used to assess the subtelty of the chromatic methodology in discriminating between two similar signals. The visual inspection of Figure D.1 indicates a minor difference in PD amplitudes between the raw and digitised signals, such a change is shown by the increase of L from 0.144 to 0.147 in the 1^{st} quarter cycle and from 0.110 to 0.115 in the 3^{rd} quarter cycle. The corresponding phase angles between the two signals can be barely noticed, yet H increased from 225.87 to 227.32 in 1^{st} quarter cycle and from 225.76 to 226.85 in 3^{rd} quarter cycle. No visible change in the spread of the two signals, hence S remained constant.

Appendix E

Examples of PD pattern recognition using various mathematical techniques

PD defect diagnosis using ANN [40]

This example uses PD data from empirical experimentation which employs tailor-made cast-resin current transformers with designated defects as testing bases. Four types of partial discharge defects were designed and include:

- Model A - perfect product.
- Model B - high voltage corona discharge.
- Model C - low voltage coil partial discharge.
- Model D - high voltage coil partial discharge.

Each of these four models was experimented on 30 times. In total, 120 sets of data were processed, 80 of which were for training, and 40 of which were for testing.

The PD data was in the 3D common format: PD amplitude - Phase of occurence - PD events count (q - φ - n).

A (M x N) matrix was built, where the φ axis (0° - 360°) with each division being 360° / M and the q axis (0 pC - 400 pC) with each division being 400 pC / N.

A triple-layer feed forward back propagation network (BPN) is used to process the PD data, as shown in Figure E.1. Experiments were carried out to elicit the proper numbers of input layer and hidden layer neurons. When the number of hidden layer neurons h is 40 and the input layer (M x N) set as M = 20 - 30 and N = 20 - 40, BPN has an optimal training effect within a short time.

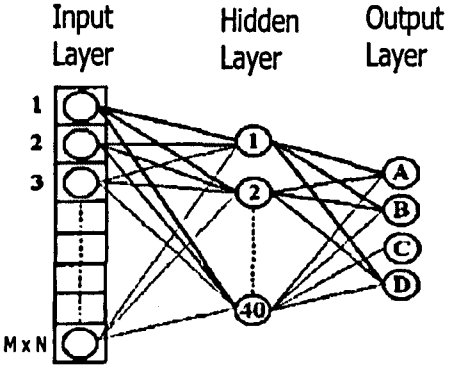

FIGURE E.1: Topological structure of BPN

120 sets of data without noise distortion undergone BPN recognition, 80 of which were for training purposes, 40 for testing. Results showed that BPN recognised 4 types of PD 100 % correctly. Distinct features make these four types of patterns an easy task, and guarantee a 100 % recognition rate.

Then 100 sets out of the 120 were distorted by random noise. With noise per discharge count at 10 %, 20 %, 30 % and 40 % respectively, the 20 sets of data then undergone BPN pattern recognition. Results are displayed in table on Figure E.2. In each PD model, there are four outcomes specifically for noise at 10 %, 20 %, 30 % and 40 %.

Recognition rate	A	B	C	D
10%	96%	94%	97%	98%
20%	81%	80%	92%	98%
30%	68%	64%	88%	95%
40%	59%	51%	82%	90%

FIGURE E.2: Recognition result under noise.

From the table above, the effect of noise at different levels is seen clearly. With noise within 10 %, the recognition rates hover over 90 %, with noise within 20 %, the recognition rates stay above 80 %. With noise higher than 20 %, the recognition rates for A and B worsen notably.

Hence, when using BPN for noise-free PD data, the recognition rate is 100 %. Noise per discharge count at 20 % lowers the recognition rate to 80 %. Hence noise interferes with PD patterns and influences the recognition rate. Real PD data is mostly corrupted with noise, which renders ANN (BPN) less effective in PD data discrimination.

Fuzzy Logic Applied to PD pattern Classification [39]

A fuzzy expert system was used to classify void size in terms of five significant features, which define the pulse shape of a PD signal [38]:

- Appparent charge transfer (proportional to the peak value of the PD pulse).
- Rise time.
- Fall time.
- Width and
- Area

A total of 25 rules were defined on the basis of 137 data samples extracted from in [93]. All work was carried out with computer, using the fuzzy expert system based on FuzzyClips V6.02 software [94].

Three cylindrical void size depths were utilised in the investigation, namely small ($\leq$ 2.0 mm), medium ($\approx$ 1.5 mm), and large $\geq$ 2.0 mm). All voids had a cylindrical diameter of 2.0 mm and were formed within an acrylic dielectric. In order to accclerate the time required to identify the membership function parameters and define the rules, the feature characteristics were plotted and their distributions approximated by trapezoidal membership functions, Figure E.3.

Figure E.4, which depicts a schematic diagram for the fuzzy PD diagnosis technique employed in conjunction with the fuzzy expert system (FuzzyClips [94] in

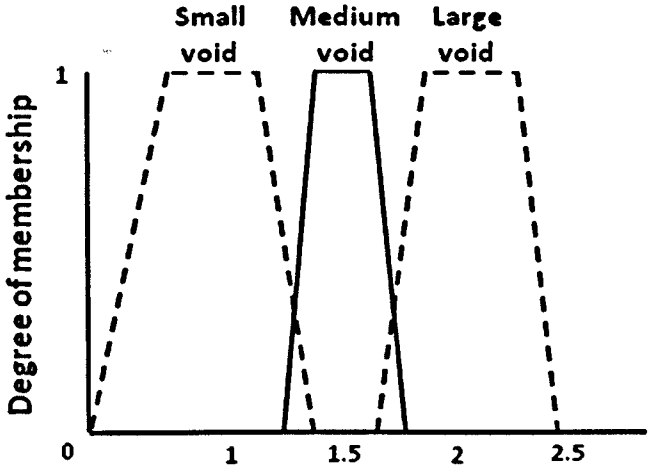

FIGURE E.3: Possible membership for void size

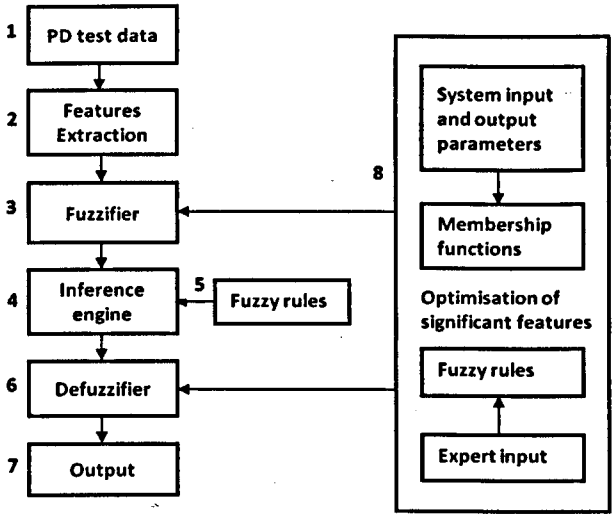

FIGURE E.4: Schematic diagram for fuzzy logic PD analysis

stages 2 to 6), makes use of the membership function in Figure E.3 to represent void sizes. Initially the membership functions representing the five significant features were defined in terms of the size of void of which they were characteristic, i.e if an charge was representative of a large void, its membership will be delineated by the membership function associated with the term "Large".

The defuzzification (stage 6 in Figure E.4) of the resultant membership function is performed, using either the centre of gravity (COG) or mean of maxima (MOM). In PD related work, the former is preferd than the latter.

With 137 processed samples, the fuzzy expert system is found to be able to idenfify the void sizes with the following success rates:

- Small voids (1,0 m) 83.8 %.
- Medium voids (1.5 m) 88.4 %.
- Large voids (2.0 m] 74 % .

The results obtained are very comparable to those attainable with NN as previously described in [38]. Additional analysis of the data on the respective feature characteristics to define further rules, related to the distinction between medium and large voids, should improve the efficency of the fuzzy logic technique.

Data mining of PD data using decision tree with genetic algorithm [54]

Data mining emerged from the ability and the necessity for converting a huge amount of data into useful information and knowledge. Data mining can be categorised into predictive and descriptive models. Predictive model uses known results from different data such as historical data to perform a prediction, whereas descriptive model identifies similar/different patterns or relationships from the data.

The predictive data mining techniques commonly used to analyse PD data are supervised. The following example will show the application of descriptive data mining technique on PD data. The technique chosen is decision tree with genetic algorithm (GA), which is a search technique used in computing to find approximate solutions to optimisation. The method aims to mine the rules/relationships which can be used to differentiate the PD types.

The PD data used had been collected from three test setups that create the basic PDs: corona, internal and surface discharges.

The integrated parameters that could be derived from the basic PD quantities (PD magnitude and phase angle) over a period of time are: the number of PD detected (n), the discharge current (I), the peak discharge magnitude (q_m) and the average discharge magnitude (q_a).

Commonly, a univariate phase-resolved distribution is used to show the variation of one integrated parameter with respect to the phase position (φ). There are four commonly used distributions: $(n-\varphi)$, $(q_m-\varphi)$, $(q_a-\varphi)$ and $(I-\varphi)$.

The statistical moments (Mean μ, Standard Deviation σ, Skewness Sk and Kurtosis Ku) are applied to positive half-cycle and negative half-cycle of the distributions. A total of 32 statistical attributes is obtained.

An open source software named Weka has a collection of machine learning algorithms for data mining tasks. Weka contains tools for data pre-processing, classification, regression, clustering, association rules and visualisation.

The program of decision tree with GA was written using MATLAB. Weka J48 which build decision tree was also used through MATLAB. The written program was used to find the best decision tree based on 2 up to 6 attributes.

Table E.1 shows the results of best decision trees and had the highest classification correctness.

Number of Attributes used	2	3	4	5	6
Rate of classification (%)	97.96	98.64	98.64	97.28	95.24

Besides mining the characteristics from the decision trees, all the best decision trees found can be used for classification purpose, i.e. samples can be fed into all the decision trees with a set of chosen attributes and can be classified by selecting which PD type appeared the most.

PD source discrimination using a SVM [77]

The flowchart shown in Figure E.5 summarises the procedure of applying the SVM to PD discrimination. The training process is based on the data from the experiment under controlled laboratory conditions (Robinson PD Detector). The testing data is representative of field data captured by a wide bandwidth sensor (RFCT) in a practical application.

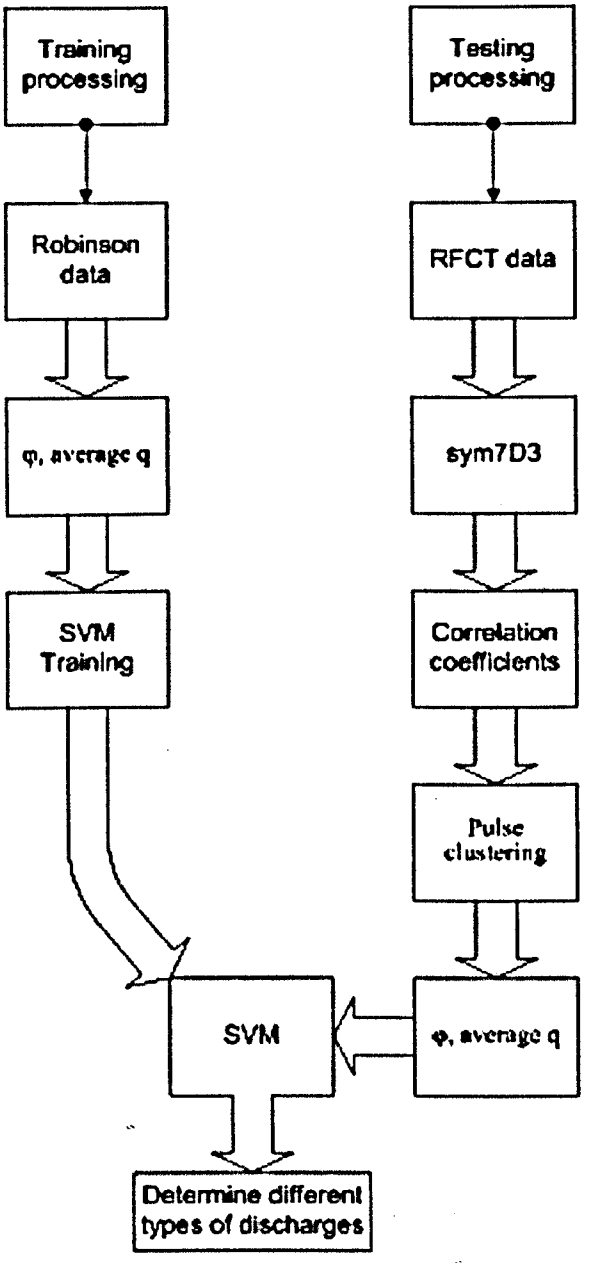

FIGURE E.5: Flowchart of SVM application

The obtained (φ - average q) information recorded by Robinson PD detector was used as the feature vector for SVM identification. The SVM was then trained using the data set obtained from the Robinson detector. The SVM identification results using correlation coefficient grouped data for single PD source are shown in the table in Figure E.6.

The numbers in the lower left corners represent the cycle numbers of each single PD source for testing. The numbers in the upper right corners are the identified cycle numbers. Each PD source consists of 20 cycles data. For corona discharge, 20

Identification type / Testing type	Corona	Surface	Internal
Corona in air	20 20	0 0	1 0
Surface discharge in air	0 0	22 20	1 0
Internal discharge in oil	0 0	0 0	20 20

FIGURE E.6: Correlation analysis based SVM identification results (single source)

cycles were correctly classified and 1 cycle was misclassified as internal discharge. For surface discharge in air, 22 cycles have been identified as surface discharge in air and 1 cycle misclassified as internal discharge. For internal discharge in oil, all 20 cycles of testing data were classified successfully. This result indicates that it is possible to identify PD events occurring within the object under test when sources are considered separately.

The SVM based method developed can discriminate between the three different sources (corona, surface and internal) but appears to overidentify the presence of internal discharge activity. The classification used is over a whole cycle and future work will be needed to develop the proposed technique so that each event is classified separately.